Vibration Analysis of Cracked Composite Bending-torsion Beams for Damage Diagnosis

Kaihong Wang

Dissertation submitted to the Faculty of the
Virginia Polytechnic Institute and State University
in partial fulfillment of the requirements for the degree of

Doctor of Philosophy
in
Mechanical Engineering

Daniel J. Inman, Chairman
Donald J. Leo
Gyuhae Park
Harry H. Robertshaw
Mahendra P. Singh

November 29, 2004
Blacksburg, Virginia

Keywords: vibration analysis, cracked composite, bending-torsion coupling, crack detection, cracked composite wing, flutter and divergence, Info-gap modeling

Vibration Analysis of Cracked Composite Bending-torsion Beams for Damage Diagnosis

Kaihong Wang

(ABSTRACT)

An analytical model of cracked composite beams vibrating in coupled bending-torsion is developed. The beam is made of fiber-reinforced composite with fiber angles in each ply aligned in the same direction. The crack is assumed open. The local flexibility concept is implemented to model the open crack and the associated compliance matrix is derived. The crack introduces additional boundary conditions at the crack location and these effects in conjunction with those of material properties are investigated. Free vibration analysis of the cracked composite beam is presented. The results indicate that variation of natural frequencies in the presence of a crack is affected by the crack ratio and location, as well as the fiber orientation. In particular, the variation pattern is different as the magnitude of bending-torsion coupling changes due to different fiber angles. When bending and torsional modes are essentially decoupled at a certain fiber angle if there is no crack, the crack introduces coupling to the initially uncoupled bending and torsion. Based on the crack model, aeroelastic characteristics of an unswept composite wing with an edge crack are investigated. The cracked composite wing is modeled by a cracked composite cantilever and the inertia coupling terms are included in the model. An approximate solution on critical flutter and divergence speeds is obtained by Galerkin's method in which the fundamental mode shapes of the cracked wing model in free vibration are used. It is shown that the critical divergence/flutter speed is affected by the elastic axis location, the inertia axis location, fiber angles, and the crack ratio and location. Moreover, model-based crack detection (size and location) by changes in natural frequencies is addressed. The Cawley-Adams criterion is implemented and a new strategy in grouping frequencies is proposed to reduce the probability of measurement errors. Finally, sensitivity of natural frequencies to model parameter uncertainties is investigated. Uncertainties are modeled by information-gap theory and represented with a collection of nested sets. Five model parameters that may have larger uncertainties are selected in the analysis, and the frequency sensitivities to uncertainties in the five model parameters are compared in terms of two immunity functions.

Acknowledgements

I would like to take this opportunity to express my sincere gratitude to Professor Daniel J. Inman for his constant encouragement, unwavering support and valuable advice. He truly exemplifies the merit of technical excellence and academic wisdom. Without his great guidance, this work would never been finished. I am also very grateful to my committee, Professors Harry H. Robertshaw, Donald J. Leo, Mahendra P. Singh, and Dr. Gyuhae Park, for devoting time from their busy schedule to providing valuable comments and suggestions on this work. A special thank you goes to Dr. Park for his helpful guidance at the beginning of this research.

I am indebted to Drs. Charles R. Farrar and Francois M. Hemez at Los Alamos National Lab. Their inspiring discussions contribute a lot to this research. Support from Los Alamos National Lab on this research is also gratefully acknowledged.

Numerous staff members in the Department of Mechanical Engineering and colleagues at the Center for Intelligent Material Systems and Structures provided valuable assistance of various kinds in the past years. Special thanks are due to Ben Poe and Jamie Archual at the Computer Lab, the program manager Beth Howell at CIMSS, and those previously or currently working at CIMSS: Rodrigo Marques, Dan Peairs, Luciano Silva, Eric Ruggiero, Honghui Tan, Henry Sodano, Mandy Cundy, Christopher Johnston, Pablo Tarazaga, and many others not named here. Thank you all for your kindness and friendship.

Last, but not the least, I would like to thank my parents for their constant support and great patience during my graduate studies, and my wife and son for their love and every enjoyable moment we shared at Blacksburg.

Contents

List of Figures

List of Tables

Chapter 1

Introduction

1.1 Motivation for Vibration Analysis of Cracked Composite

Composite materials have been used for a long time. They can be traced all the way back to early human history. For instance, archaeologists discovered that ancient Israelites used straw to strengthen mud bricks, and many medieval swords and armors were even constructed with layers of different materials. In general, composite materials can be defined as the combination of two or more materials on a microscopic scale to form a useful material. The advantage of composites is that the overall properties are superior to those of the individual constituents. The properties that can be improved during the formation of a composite material usually include, but not limited to: strength; stiffness; corrosion resistance; surface finish; weight; fatigue life. In recent decades, due to the high strength-to-weight and stiffness-to-weight ratios, fiber-reinforced composites have been extensively used for many applications, such as aerospace structures and high-speed turbine machinery. Accordingly, mechanics of fiber-reinforced composites have been intensively studied and handbooks guiding the design and testing have also published. The present research is concerned with investigation on the vibration characteristics of a cracked composite beam, with motivations explained in the following two subsections. Specifically, the topic on a composite laminated beam that has a surface crack and vibrates in coupled bending and torsion will be studied. Unless stated otherwise, the composites mentioned thereafter refer to the fiber-reinforced composite materials.

1.1.1 Failure of Composite Wings

Unlike conventional metals and metal alloys, composites possess properties that can be controlled to large extent by selecting constitutive components, the volume fraction ratio of fiber to matrix, and the geometry and orientation of fibers. The design flexibility, high strength-to-weight ratio, improved corrosion and temperature resistance, and reduced manufacturing costs are especially desirable for space and aeronautical applications, and consequently composites are widely used in aerospace engineering. For instance, NASA and Boeing jointly launched the NASA ACT (Advanced Composite Technology) program in 1989 to improve the efficiency of composite structures, which aimed to reduce air travel costs through the use of composite materials on commercial aircrafts. Technologies such as stitching, braiding and knitting were applied to 3-D composites, resulting in significant reduction in cost (20% to 25%) and weight (30% to 35%) (Dow and Dexter, 1997; http://www.larc.nasa.gov).

The direct motivation of this research stems from the wing failure of some Unmanned Aerial Vehicles (UAVs). As one of the UAVs designed for surveillance and reconnaissance missions, the Predator is a long endurance, medium altitude and low speed unmanned airplane with the fuselage and wings all made of composites. It has been given strike capability with the addition of laser-guided missiles. It is 27 ft. long and has a 49 ft. wingspan. The system operates at an altitude of 25,000 ft. and at a range of 400 nautical miles. Some of these aircrafts deployed in service crashed without suffering from any external attacks, resulting initially from a sudden wing failure. Inherent flaws from the manufacturing processes as well as design deficiencies may account for the original sources of the wing failure; internal damage such as delamination, fiber/matrix cracking and debonding between matrix and fibers could be the direct outcome of impact and/or fatigue loading during the flight. While failure resistance at the design and manufacturing stages needs to be improved or qualitatively controlled, understanding the dynamics of the composite wing once some form of damage develops and propagates is of very importance. Not only is structural analysis for the system important, but the analysis is needed to develop a systematic tool for in-service damage detection and lifetime prediction of aerial vehicles.

The actual wing failure may result from the combination of different damage some of which are mentioned above. Depending on the actual design, stacking sequences, fiber orientation and volume fraction, manufacturing processes, loading spectrum, and environmental factors, to name a few, are all important. Since different damage has fairly different mechanisms in terms of its static and dynamic characteristics, it is common in the composite community to differentiate an individual damage format from others for both theoretical and experimental analysis in order to construct cornerstones for more complicated situations. With delamination the prevailing format among others, fatigue cracks inside the structure and on the surface are also widely observed, either in composite wings or in other composite structures. In this research, a surface fatigue crack on a composite wing is investigated.

Cracks in a composite structure and the associated stress analysis are real engineering problems in fracture mechanics. With relatively high strength and low ductility, composite materials usually possess fatigue properties similar to some brittle metals. Cracks in fibers, matrix, and the interfaces of fibers and matrix are very common as the fatigue failure mode in composites. A large number of publications can be found dealing specifically with cracks in composite materials. Fracture mechanics of composite materials were well developed in recent decades supported with intensive theoretical and experimental analyses (Sih and Chen, 1981). Fracture testing of composite structures in aerospace engineering plays an important role in determining the failure resistance of composites. For instance, the fracture behavior of a stitched carbon fabric composite was investigated at NASA (Clarence *et al.*, 2001). Specimens with various thicknesses representing a wing skin from tip to root were tested. Normal and shear strains were calculated on fracture planes for plane anisotropic crack problems. The crack propagation mechanisms of composite wing skin panels were assessed with mathematical models using fracture mechanics in anisotropic cracked structures (Yuan, 2001). Critical fracture parameters governing the severity of stress and deformation field ahead of the cracks were evaluated.

While a vast amount of research has focused on the stress and deformation analyses of cracked composites using various fracture mechanics, relatively less investigation has been

devoted to studying the vibration characteristics of cracked composite structures, especially aiming at those of composite aircraft wings under some damage conditions. A detailed literature review will be given in the next chapter. This research concentrates on the vibration analysis of a cracked composite beam, which could contribute to research on real cracked composite wings with large wing span and high aspect ratio for damage diagnosis and prognosis on the remaining life.

1.1.2 Vibration-based Structural Health Monitoring

With a tremendous growth in the last years, structural health monitoring (SHM) has emerged as a well-recognized field of technology. The essential concerns of structural health monitoring involve the integration of smart materials, sensors, data processing, telemetry, modern computational power and decision-making algorithms into structures to detect damage, access the integrity and even predict the remaining life time based on projected loading and environmental conditions. Traditional non-destructive evaluation (NDE) techniques such as liquid penetrant, magnetic particles, radiography, ultrasonics and eddy current methods usually require off-line inspection and the knowledge of possible damaged areas. The inaccessibility to the inspection location could result in great challenges and even become prohibitive for most NDE techniques. Structural health monitoring, on the other hand, may have an array of sensors attached on or imbedded in the host structure in service, and be able to continuously monitor in real time those physical parameters that can be further processed for damage detection and health status assessment. The inaccessibility issues could be eliminated to the lowest possible level. The downtime for pre-scheduled maintenance as well as associated costs is greatly reduced.

Techniques in structural health monitoring especially benefit aerial and ground vehicles, aerospace structures, civil infrastructures such as bridges and buildings, offshore systems, and many more. SHM has attracted significant attentions in both industry and academe worldwide. Since 1997 a biannual international workshop on SHM is held in Stanford, California. Alternatively another biannual international workshop takes place in Europe (from 2002 on). Papers involving SHM are also frequently presented in many other

conferences, for instance, the joint annual international symposiums on Smart Structures and Materials and Nondestructive Evaluation for Health Monitoring and Diagnostics organized by the Society for Optical Engineering (SPIE), the annual International Modal Analysis Conference (IMAC), and the biannual International Conference on Damage Assessment of Structures (DAMAS). An increasing number of articles about research and applications with SHM have also appeared in a few journals in the field of structural design and dynamics. Particularly, An International Journal of Structural Health Monitoring was launched in 2002 to publish peer-viewed papers involving theoretical, analytical and experimental investigations on SHM.

There are several cornerstones for a SHM technique to build upon in order to be successfully used in a real application satisfying reliability, cost-effectiveness and other pre-defined requirements. Understanding damage mechanisms of the materials as well as dynamics and failure mechanisms of target structures under working conditions could be the first step for a feasible SHM scheme. This will provide guidelines for further implementation of sensor arrays, data processing and decision making. While a large amount of work on material properties including fatigue mechanisms has to be performed before a material can be actually used, most of them are performed at the coupon level with which external loadings and working environments are well controlled. Investigation on failure dynamics at the system level may require experiments and testing on prototypes; current CAE software may not be able to predict the exact failure behavior with the accuracy heavily depending on the complexity and previous knowledge of the failure mode. The primary objective of SHM is to detect a variety of damages at the earliest possible stage to prevent catastrophic failure. The more one understands the dynamics of a structure with various damages, the more possible a reliable SHM strategy can be developed. Since damage (e.g., crack, corrosion, creep) on a structure usually changes the mass, stiffness and/or damping distribution of the structure either locally or globally, vibration characteristics of the structure may be changed so that evaluation of vibration responses may be used to detect the damage. The importance and summary on previous research can be found in several survey papers, for instance the one by Doebling *et al*. (1998). Other fundamentals in SHM include development of more advanced sensors and implementation of smart materials aiming at measuring accurately

small changes of a variety of physical parameters in real time. Unlike many NDE techniques requiring no historical data, SHM techniques usually take measurement and store historical data for comparison and analysis. Data processing, feature extraction, statistical analysis and final decision making are very important for a SHM technique to be implemented.

The research proposed here contributes to the SHM communities through an investigation on vibration characteristics of cracked structures. Attention is focused on the cracked beam made of fiber reinforced composite vibrating in coupled bending and torsion. A brief review on SHM, vibration-based damage detection and vibration characteristics of damaged composites will be given in the next chapter.

1.2 Objectives

As mentioned above, this research is focused on the composite beam of a relatively large aspect ratio. Due to the anisotropic nature of fiber-reinforced composites, a torsional movement coupled in most cases with the bending mode is more significant compared with the shear deformation and rotary inertia of the beam, especially during the aeroelastic analysis of an aircraft wing. The composite beam under investigation is basically a one-dimensional problem but with two independent variables (bending and torsion), with the shear deformation and rotary inertia neglected. As a damage mode, cracks on the composite could take various formats, such as surface or internal cracks, fiber or matrix cracks, regular or irregular cracks, or a combination of any of these. To reduce the complexity and as an initial step toward more sophisticated situations, this research assumes the crack is on the edge surface and remains open to avoid non-linearity problems. Moreover, damping of any kind is also neglected. The objectives are then to model the edge crack, analyze the vibration characteristics of the cracked beam considering also the composite anisotropic properties, and implement the model for predicting flutter/divergence instability of a cracked composite wing. Detailed tasks are described as follows:

- **Modeling the edge surface crack based on linear fracture mechanics**. The local flexibility method is used and a local flexibility matrix is derived specifically for the composite beam considering only bending and torsion. Then additional boundary conditions at the crack location can be established such that the beam can be replaced with two intact beams connected at the crack location.
- **Analysis of free vibration characteristics of the cracked composite beam**. To facilitate the analysis on flutter/divergence of a cracked composite wing, clamped-free (a cantilever beam) boundary conditions are assumed. Changes in natural frequencies and mode shapes with respect to the crack location, crack ratio, fiber angles and fiber volume fraction are obtained and plotted.
- **Prediction on flutter and divergence speed for a cracked composite wing**. A beam model is taken to simulate a composite wing with a large aspect ratio. The fundamental bending and torsional modes of the cracked cantilever beam are used with Galerkin's method for an approximate solution to flutter and divergence speed. Again, variation of the flutter/divergence speed for different crack location, crack ratio and material properties are compared.
- **Crack detection based on changes in natural frequencies**. While natural frequencies are relatively easier and more accurately measured than other modal parameters, solving an inverse problem for crack detection based only on changes in natural frequencies is not so easy, considering that fact that natural frequency has a global nature while damage in most cases is a local phenomenon. However, if the crack is the most possible failure mode and no other form of damage exists, detecting the crack by natural frequencies is possible, even with the presence of measurement errors.
- **Uncertainty analysis of model parameters**. Since no experimental data is available so far for the beam model with or without a crack, an analysis on the uncertainty of model parameters complements this research. It will also help future efforts in model updating. Information-gap theory is selected to investigate the uncertainties in model parameters, because no statistical data is available. Two stiffness parameters, EI and GJ, and the coupling term, K, are chosen as the

statistically varying quantities. The output performance will be the correlation of natural frequencies.

1.3 Review

The following chapter reviews the literature on structural health monitoring, vibration analyses of damaged composites with a special attention on that of cracked composite beams, and uncertainty analysis of model parameters using Info-Gap theory. The background of this research and other related work will also be reviewed. Chapter 3 starts with modeling a surface crack and establishing the local flexibility matrix at the crack location. The prototype is based on a cracked prismatic bar made of isotropic and homogenous materials. Then correction of related coefficients for an isotropic composite is made so that the local flexibility matrix for a cracked composite beam is obtained. The composite beam model is directly taken from a paper by Weisshaar (1985) since it has the quality close to a box model for an aircraft wing made of fiber-reinforced composites. This model, considering coupling between bending and torsion, is also widely used for aeroelastic analysis of composite wings. Combined with the crack model, a cracked beam model is then developed and the natural frequencies and corresponding mode shapes of a cantilever beam (clamped-free boundary conditions) are plotted. A simple comparison with a cracked composite beam considering only bending is given. Chapter 4 uses the cracked composite beam model to simulate a cracked composite wing and applies quasi-steady aerodynamic forces for an aeroelastic stability analysis. The fundamental coupled bending and torsional modes are used in Galerkin's method to obtain an approximation solution of flutter and divergence speeds. Plots of the crack induced changes in flutter/divergence speed, in conjunction with material properties, are obtained. In Chapter 5, a crack detection method based on changes in natural frequencies, the Cawlay-Adams Criterion, is taken to detect both the crack location and crack ratio. It is shown with the presence of measurement error that each frequency change is not equally valuable for the detection. Chapter 6 comes back to the initial cracked beam model and investigates the sensitivity of natural frequency to the model parameters. The Info-Gap theory is taken since no statistical data is available for the model so far. Finally, Chapter 7 summarizes contributions of this research and proposes some work for future endeavor.

Chapter 2

Literature Review

2.1 Structural Health Monitoring (SHM)

It is quite common that before and after a mechanical system is finally put into service, evaluation and testing on its integrity, including that of its components, should be performed. Non-destructive evaluation (NDE) or non-destructive testing (NDT) is then widely implemented for safety/reliability purpose, which usually refers a noninvasive assessment of structural quality during or after manufacturing, or of its condition during or after use. Many NDE techniques are well developed and successfully instrumented for a variety of applications, such as ultrasonic inspection, eddy current testing, X-radiography and acoustic emission testing. However, traditional NDE methods can not satisfy the increasing needs of on-line inspection and continuous assessment of structures' health condition while the structures are in service. Nor are they capable of predicting the remaining life once some damage is diagnosed. With technological advances in smart materials, sensors, data and signal processing, computational power as well as increasing needs on real time assessment of structural health status, it is not surprising that structural health monitoring has emerged as a natural evolution from traditional NDE technologies to meet those requirements. Although SHM may be literally categorized under the framework of NDE in terms of terminology, it does deviate from traditional concepts of NDE in the sense that the ultimate goal of SHM is the real time, automatic and continuous assessment of structures in service with minimum human labor involved.

A brief comparison of differences between traditional NDE methods and current SHM techniques is given in the table that follows. It is noted that apparent distinction between the two is difficult, since many ideas and techniques are certainly applicable to both NDE and SHM.

Table 2.1 A brief comparison of traditional NDE and SHM

	Traditional NDE	SHM
Objectives	Detection of local structural damage.	Continuous assessment of structural health conditions, including damage detection and lifetime prediction.
Data history	No historical data required.	Data history needed for continuous monitoring.
Maintenance approach	Schedule-based; fixed-time overhauls.	Condition-based.
Typical techniques	Visual inspection; liquid penetrant; eddy current; ultrasonic wave; magnetic particles; acoustic emission; radiography; etc.	Variety such as vibration-based (global or local), wave propagation, strain; etc.
Physics	Capillary action; electrical/magnetic properties; wave propagation; X-ray.	Static or dynamic changes in physical properties due to presence of damage.
Damage format	Cracks (internal and surface); voids; pores; surface corrosion; etc.	Any kind of structural damage.
Instrumentation	Well instrumented.	To be instrumented.
Sensor	Single type of sensor; isolation from host structures.	Sensor array; fusion of different kinds of sensors; integration of sensors to host structures.
On-line or off-line	Off-line inspection.	Both, with on-line targeted.
Accessibility	Direct access to damage locations.	Direct access not necessary.
Cost	High maintenance cost.	Low labor and maintenance costs.
Operational guidance	No guidance with damage removed during downtime.	On-line guidance while damage is developing.

The fundamental of SHM technology is the development of damage detection techniques. Structural damage may be defined as changes introduced to a system that

adversely affects its current or future performance (Doebling *et al*., 1998). A classification system for damage detection defined by Rytter (1993) includes four levels: 1) determination of damage existence in a structure; 2) level 1 plus determination of damage type and location; 3) level 2 plus quantification of damage severity; 4) level 3 plus prediction of remaining service life based on damage assessment and operational conditions.

The development of damage diagnosis in SHM is typically the collaboration between multi-disciplinary fields, such as sensing technology, smart materials, signal processing, system integration, data interpretation, etc. Vibration-based technologies are among topics that received intensive research interests during the relatively earlier stage of SHM history, and still play significant role in concurrent SHM strategies. Papers presented in a series of conferences on SHM indicate that a variety of sensing techniques and diagnosis algorithms have been investigated to monitor the health status of various structures, and many of them have been targeted directly for real applications in civil infrastructure, aeronautical and astronautic systems, ground vehicles, offshore platforms and underground pipelines.

The development of SHM techniques has been closely embraced by applications in a variety of industries. Monitoring the health status of aging and new structures in civil and aerospace engineering in order to reduce the maintenance cost and provide real time assessment on structural integrity supplied the original motivation during earlier stages. Implementation of SHM technologies have now expanded from these two traditional areas to ground transportation, underground pipelines, offshore and undersea structures and vehicles, and even biomedical devices, which will also affect the traditional philosophy of structural design and maintenance practice. Many experiments were conducted in labs at the coupon level or in the field. For infrastructures, Huston *et al*. (1997) studied the inspection of bridge decks by ground penetrating radar, and reported the feasibility of detecting internal cracks. Liu and Sun (1997) proposed a neural network system to data processing for a bridge health monitoring where the longitudinal elongations of the bridge subjected to moving trucks are used for damage detection. A research group at Los Alamos National Laboratory (Farrar *et al*., 1997) conducted intensive investigation on SHM with a focus on civil structures (e.g., the I-40 and Alamosa Canyon bridges). Vibration-based methods and statistical pattern

recognition are exploited for damage detection in real structures. Van der Auweraer and Peeters (2003) reviewed many projects launched worldwide in recent years to promote SHM development in versatile applications. In aerospace engineering, with more and more commercial (and military) aircraft now serving near or beyond the design life, the real-time assessment on structural integrity is specially desired for increasing reliability and reducing maintenance cost. For instance, NASA and Lockheed Martin jointly initiated a fiber optic-based integrated vehicle health management (IVHM) system for NASA space shuttles and Lockheed Martin X-33 reusable launch vehicle (RLV) (Melvin *et al*., 1997; Sirkis *et al*., 1999). The concept of IVHM has become a terminology widely accepted in the aerospace community (Derriso *et al*., 2003). With advances in sensor technology, smart materials, data processing and computer simulation and visualization, integrated SHM systems for a variety of applications along with codes and standards could come into use in the near future.

The following two sub-sections briefly review SHM techniques from two different perspectives in order to provide background for the present research. Firstly, techniques in damage detection are roughly grouped to the vibration-based methods and the methods based on wave propagation. Next, based on whether or not mathematical models are used, SHM techniques can be divided into two groups. A brief discussion on advantages and disadvantages of each group will be addressed.

2.1.1 Vibration-based SHM and SHM based wave propagation

A) Vibration-based SHM

Vibration usually refers to a periodic motion in an elastic structure about an equilibrium position. The premise of vibration-based techniques in SHM is that damage will alter the stiffness, mass, or damping properties of a structure which in turn affect the dynamic response of the structure such as natural frequencies, mode shapes and damping ratio of the structure. Intuitively then, changes in dynamic responses (modal parameters, forced responses, etc.) could be used to locate and even quantify the damage in the structure. An excellent review paper by Doebling *et al*. (1998) summarized the vibration-based damage

detection methods published up to 1996. Recently Sohn *et al*. (2004) reviewed SHM literature in a wider range for papers published between 1996 and 2001, in which SHM problems are considered as statistical pattern recognition and damage detection techniques including the vibration-based methods are categorized into the statistical pattern recognition paradigm. More comprehensive review and analysis can be found in these two papers. The following is devoted to briefly sketching a background for this research, with topics grouped by the dynamic characteristics considered during the vibration-based damage diagnostics.

Natural Frequencies

Among all modal parameters, natural frequencies of a structure are relatively easier and more accurate to measure. Inspecting changes in natural frequencies for damage detection was the major approach in vibration-based evaluation decades ago when modern experimental modal analysis had not been fully established, and so far still receives much research attention in SHM. Early systematic investigation on damage detection by changes in natural frequencies may be attributed to Adams *et al*. (1978) and Cawley and Adams (1979). Under the premise that the change in stiffness is independent of frequency, the ratio of frequency changes in two modes is only a function of the damage location. Experiments were carried out on an aluminum plate with damage in the form of a rectangular hole and a CFRP (carbon-fiber-reinforced plastic) plate with saw cuts and crushing damage. With a finite element model, good agreement was obtained on the damage location and magnitude for the aluminum plate, although less accurate results were found with the CRRP plate. Stubbs and Osegueda (1990a, 1990b) developed a sensitivity approach for damage detection from changes in natural frequencies that is based on the so-called Cawley-Adams criterion. Friswell *et al*. (1994) also extended the criterion by introducing statistical analysis on the likely damage scenarios. Palacz and Krawczuk (2002) compared several vibration-based methods including the Cawley-Adams for damage detection in a cracked beam, and indicate that first two frequency changes without measurement errors or four frequency changes with measurement errors could successfully detect both the location and depth of the surface crack. In Chapter 5 the Cawley-Adams criterion is again applied for the composite beam with an edge crack. With the presence of measurement errors, the feasibility of crack detection based on the analytical model is presented. However, as mentioned by Doebling *et al*. (1998) and

Firswell and Penny (1997), damage identification by frequency shifts alone has practical limitations in some applications. For instance, frequency changes are far more affected by temperature and humidity than by damage in the inspection of a bridge (Farrar *et al*., 1994). Moreover, natural frequency exhibits the global nature of a structure, and is usually insensitive to incipient damages, especially when the damage is located at a low stress region.

Salawu (1997) provided a good review on damage detection by changes in natural frequencies. Although it might not be so reliable using natural frequency changes alone for damage identification in some infrastructures such as prestressed concrete structures as indicated in the paper, many strategies and algorithms were developed to further explore the advantages of natural frequencies. Messina *et al*. (1996) developed an algorithm called damage location assurance criterion (DLAC). A DLAC value is calculated from the vector of experimental frequency changes and the vector based on theoretical analysis on a presumed damage location. The damage location is obtained by comparing the patterns of frequency changes. Messina *et al*. (1997) later extended the approach to the multiple damage location assurance (MDLAC) by incorporating mode shapes for the frequency sensitivity. Armon *et al*. (1994) proposed a rank-ordering of modes by the frequency shifts to detect slots and cracks in a beam, and showed that this method is robust with respect to both measurement errors and model uncertainties. Nicholson and Alnefaie (2000) introduced another damage-sensitive parameter called the modal moment index (MMI) extracted from measured modal parameters. The index has an abrupt change at the damage location and can be related to damage magnitude. Solving an inverse problem from the first three natural frequency changes, Chaudhari and Maiti (2000) used the Frobenius technique for the governing differential equation and then obtained the crack location by a semi-numerical approach, while Chinchalkar (2001) resorted to finite element modeling by a rank-one modification of an eigenvalue problem. Neural networks are also implemented for damage detection using natural frequencies, such as Luo and Hanagud (1997), Zhao *et al*. (1998), Yun and Bahng (2000), and Zapico *et al*. (2003). Jones and Turcotte (2001) took antiresonant frequencies in finite element model updating to detect structural damages. While the beating phenomenon was first investigated by Cattarius and Inman (1997) for damage detection in time domain, Abdel Wahab and Mottershead (2001) used the beating frequencies rather than the natural

frequencies to detect the onset of damage, which was demonstrated by the authors to be more sensitive as a damage indicator. Friswell *et al*. (1998) combined genetic and eigensensitivity algorithms for locating structural damages. Pawar and Ganguli (2003) used a genetic fuzzy system to find both the location and extent of damage in a cantilever beam.

Mode Shapes/Curvatures

Mode shapes are known as the spatial description of the amplitude at each resonance frequency. The modal assurance criterion (MAC) and related variations were developed in last two decades as a quality assurance indicator to explore the spatial modal information in the area of experimental and analytical structural dynamics (Allemang, 2002). West (1984) proposed possibly the first systematic investigation on damage detection by using MAC as the statistical indicator correlating mode shapes of the damaged and undamaged structure without the use of a prior finite element model. Another widely used criterion in damage detection is coordinate modal assurance criterion (COMAC) that identifies the coordinates where two sets of mode shapes do not agree (Lieven and Ewins, 1988). Examples with a focus primarily on MAC and COMAC include Yuen (1985), Rizos *et al.* (1990), Lin (1994), Saitoh and Takei (1996), Natke and Cempel (1997) and Marwala and Hunt (2000). Furthermore, Ratcliffe (1997) proposed a method for damage detection based solely on mode shapes. The location of damage can be identified from the finite difference approximation of a Laplacian operator to the mode shapes. Khan *et al.* (1999) used a continuously scanning laser Doppler vibrometer to monitor the discontinuities in mode shapes for detecting cracks and slots. Shi *et al*. (2000) formulated the MDLAC with incomplete mode shapes instead of natural frequencies for damage detection.

As an alternative in using mode shapes, curvature mode shapes were proposed and considered more sensitive to damage than the displacement mode shapes (Pandey *et al*., 1991). Lew *et al*. (1997) compared the method by curvature mode shapes with two other modal based methods and found it is reliable for beam-type structures but not suitable for truss-type structures. Amaravadi *et al*. (2001) obtained the curvature mode shapes by differentiating mode shapes twice, and then combined a wavelet map with them to improve the sensitivity and accuracy for locating damage in a lattice structure and a cantilever beam.

Stubbs *et al*. (1995) presented a damage index from the integration of the mode shapes for a pattern recognition technique in damage detection. Carrasco *et al*. (1997) used changes in modal strain energy to locate as well as quantify damage in a space truss model containing 12 bays. It is claimed that magnitude of the changes can be used as the indicator of overall magnitude of damage. Kim and Kwak (2001) studied strain mode shapes to detect cracks in plates. Abdo and Hori (2002) found that the rotation of mode shapes is a sensitive and robust indicator of damage. Cho *et al*. (2004) proposed a probabilistic neural network trained by mode shapes and natural frequencies and applied the technique for damage detection in a cable stayed bridge.

Unlike frequency extraction, estimating mode shapes usually requires the measurement at each of the points where estimates are needed, posing practical difficulties due to limitations in the number of sensors and the capability of accurate measurement. Moreover, mode shape estimation from the frequency response functions, even in the absence of any damage, could become problematic when the structure has complicated configurations. It is typically an application dependent technique, the feasibility and accuracy being affected by the type of structure, the damage format, the way to extract mode shapes and the algorithms in post-processing.

Damping

Although the estimation of damping matrix (mass and stiffness matrices as well) by frequency response functions (Chen *et al*., 1996), input/output data (Fritzen, 1986) and many other approaches has been the topic in the field of system identification for many years, damage detection based on changes in damping parameters alone has not been studied intensively compared to methods based on natural frequencies and mode shapes. This could be due to the existence of various types of damping and the relatively high uncertainties in damping estimates. While an abnormal increase in damping coefficients, suggesting more energy dissipation, could indicate damage in the structure as observed experimentally in most cases (Morgan and Osterle, 1985; Napolitano and Kosmarka, 1996), damage in a structure may also result in a decrease in damping or an increase followed by a decrease (Salane and Baldwin, 1990; Hearn and Testa, 1991). Williams and Salawu (1997) reviewed studies

mainly in civil engineering on the correlation of damage and damping changes, and concluded that damping values alone can not provide a reliable means for damage detection (location and size).

Changes in damping, however, may have the ability to detect damage to which conventional methods based on changes in natural frequencies and mode shapes are not sensitive. Modena *et al*. (1999) showed that visually undetectable cracks cause negligible changes in natural frequencies, but a considerable increase in damping that can be used to locate the cracking. Testing to identify manufacturing defects and structural damage in precast reinforced concrete elements justified the use of damping changes and non-linear response as damage indicators. Kawiecki (2000) measured damping coefficient of a metal beam and a metal blank used to fabricate 3.5" computer disks. An array of piezotransducers is used to provide both excitation and sensing. Changes in damping due to damage are observed; only the existence of damage, rather than the location and severity, can be answered. Recently, Kyriazoglou *et al*. (2004) defined a damping parameter as the ratio of energy dissipated in one cycle over the total energy stored in that cycle. With fatigue cracking in all specimens, the damping values are obtained from testing on cross-ply GFRP (glass fiber reinforced plastic) laminates, woven GFRP laminates and woven CFRP laminates. The results indicate that while there are no detectable changes in resonance frequencies, the damping parameter is fairly sensitive to small cracks in composites and hence promising for detection of initial damage. Techniques of damage detection based on measuring damping in a structure seem only able to answer the Level 1 (existence of damage) questions, and may monitor the growth of damage severity by comparing historical data. Locating and quantifying damage by changes in damping alone still remains a challenging problem.

Frequency Response Functions (FRFs)

Frequency response functions depict in frequency domain the input/output relationship for a system, and are extensively used in structural dynamics and system identification to extract resonance frequencies, estimate mode shapes and damping coefficients, and verify matrices of mass, stiffness and damping. Many damage detection methods based on evaluation of modal parameters aforementioned rely on some FRF data, directly or indirectly.

This also implies that information in FRF data may contain features that can be directly analyzed for damage detection. Chaudhry and Ganino (1994) trained an artificial neural network with frequency response data of a composite/aluminum beam in both damaged and undamaged situations. The training data contain the magnitude and phase of FRFs obtained experimentally over a specified frequency range. The trained neural network is able to identify the debonding on the beam. Wang *et al*. (1997) demonstrated an algorithm to locate and quantify the damage on a plane 3-bay frame structure by using the directly-measured FRF data. A damage vector indicating the location and magnitude is calculated from the perturbation equations of the FRF data. The selection of sensor/actuator locations and excitation frequencies is addressed in order to reduce the influence of measurement errors. Swamidas and Cheng (1997) measured the acceleration and strain FRFs in tubular T-joints, and found the antiresonant regions and quasi-static regions of the FRF curves showed considerable changes during the crack initiation and growth that may be undetectable by changes in natural frequencies. With a simply supported truss bridge, Thyagarajan *et al*. (1998) studied damage detection by using minimum number of sensors in optimization of FRFs. Lopes *et al*. (2000) used the FRFs obtained from a finite element model to train a neural network, and measured FRF data extracted from electric impedance through piezoceramic transducers are used to solve an inverse problem of damage detection. Mottershead *et al*. (2003) explored the possibility of detecting damage by using rotational FRFs. Recently, based on the observation that damage may increase the non-linear behavior in a structure in which the dynamic response is predominantly linear in the absence of damage, techniques focused on extraction of non-linear distortions in FRF data were developed to locate and quantify damage (Vanhoenacker, *et al*., 2004). Hwang and Kim (2004) presented a method in damage detection by using only a subset of vectors from the full set of FRF data for a few frequencies to calculate changes in the stiffness matrix. Damage detection by direct use of FRFs is still a research topic under exploration.

Time Domain Features

Modal parameters and FRF data usually involve data reduction and feature extraction during the transform of recorded data in time domain to features in frequency domain. The process may cause loss of important information related to damage dynamics; this

disadvantage could be avoided by directly using time response data for damage detection. Another advantage of using time domain features is that non-linearity responses raised by damage in a structure could be preserved further facilitating diagnostics. Numerous researchers used the family of ARMA (autoregressive moving average) models for damage detection by either extracting modal parameters from the model (Qian *et al.*, 1990; Li *et al*., 1993), or via comparison of parameters of the ARMA model to a baseline as the damage indicator (Garcia and Osegueda, 1999; Sohn and Farrar, 2000).

Methods by estimating damage-sensitive parameters from time responses without resorting to the extraction of modal parameters are investigated by many researchers. Agbabian *et al*. (1991) demonstrated the potential of using time responses for identification of structural changes in the presence of noise interference. An equivalent discrete mathematical model with the degrees of freedom compatible with the number of sensors is constructed from time-domain data. The identification involves the determination of the mean, variance and probability density function corresponding to each element of the system matrices. With piezoceramic patches as sensors and actuators, Banks *et al*. (1996) developed a model-based technique to estimate changes in damping, mass and stiffness properties from the time histories of input/output data. An inverse optimization problem is solved via the enhanced least square error minimization. Damage simulated by holes on a cantilever beam is identified in a satisfactory accuracy. Without relying on modal parameters and analytical models, Cattarius and Inman (1997) proposed a time-domain approach by taking the advantage of beating phenomenon to detect small damage that many be unnoticeable in natural frequency changes. Carneiro and Inman (2000) investigated the detection of a surface crack on a Timoshenko beam in time domain with the aid of an analytical model developed by the authors. A bilinear model of a closing crack is also considered. While the minimum rank perturbation theory (MRPT) has been extensively investigated in frequency domain by Zimmerman and his co-workers for damage detection, Lopez III and Zimmerman (2002) introduced a time-domain MRPT for detection of structural damage over a specified analysis time interval. The stiffness perturbation between successive time steps is evaluated via a recursive updating. With finite element models, Cacciola *et al*. (2003) applied the Monte Carlo method to evaluate the higher order statistics of a non-linear beam with an edge crack.

Measurement of the skewness coefficient of rotational degrees of freedom that is sensitive to the non-linear behavior can be used to locate and quantify the crack. Majumder and Manohar (2004) investigated damage identification on a non-linear beam subjected to moving load, a simulation of bridge with moving traffic load. Finite element models including a reduced-order model accommodating the limited number of sensors are constructed with time varying coefficients. A damage indicator vector is determined from time response to locate the damage in the form of stiffness loss.

It is noted, however, model-based time domain methods usually involve intensive computational effort and a considerable larger amount of data to process than the modal-based approaches in damage detection.

Others

In addition to methods mentioned above, there is a group of damage detection techniques that estimate changes in stiffness through the dynamically measured flexibility matrix (the inverse of static stiffness matrix) formulated usually from the lowest a few natural frequencies and mass normalized mode shapes. The flexibility matrix is more sensitive than the stiffness matrix to changes in lower modes and frequencies (Doebling *et al*., 1998). Proposed methods include the comparison of flexibility changes (Pandey and Biswas, 1994; Zhang and Aktan, 1995), the unity check method (Lim, 1990; Lin, 1998), and the residual flexibility method (Doebling *et al*., 1996), etc.

Techniques in model updating can also be closely related to, and used for, damage detection in that the updated structural matrices (mass, stiffness and damping) from the testing data may reflect changes due to the presence of damage. Proposed methods include, but not limited to, optimal matrix update methods (Baruch and Bar Itzhack, 1978; Kammer, 1988; Smith and Beattie, 1991; Liu, 1995), the minimum rank perturbation theory (Zimmerman and Kaouk, 1994; Kaouk and Zimmerman, 1995; and their co-workers), sensitivity-based methods (Norris and Meirovitch, 1989; Sanayei and Onipede, 1991), eigenstructure assignment methods (Zimmerman and Kaouk, 1992; Lim, 1995).

Another class of techniques based on electro-mechanical impedance method has been widely investigated in damage diagnostics. The electro-mechanical impedance can relate changes of local vibration characteristics to the existence or growth of structural damages. Typically, small piezoelectric patches bonded to the area close to a possible damage site are used to excite the local area at high frequencies, and both electrical and mechanical impedance can be obtained through the electro-mechanical coupling of the piezoelectric sensors. The electro-mechanical impedance is shown very sensitive to incipient damages. Another advantage is that no analytical or numerical models are needed so that errors introduced during the modeling can be avoided. The impedance-based methods, on the other hand, so far could hardly locate accurately nor quantify the damage in a structure. The possible damage area is usually known a prior in order to place the sensor/actuator patches for the testing on the local properties. A large number of publications can be found in literature from the earlier investigation on the basic concept (Liang *et al*., 1994; Sun *et al*., 1995), to various implementations and applications (Chaudhry *et al*., 1995; Raju *et al*.,1998; Park *et al*., 2000). A comprehensive survey on impedance-based SHM can be found in Park *et al*. (2003).

B) SHM based on wave propagation

As one class of the widely used approaches, wave propagation methods adopt a transmitter and a receiver to send a diagnostic stress wave along the structure and measure the changes in the received signal due to the presence of damage in the structure. This approach is a natural extension of traditional NDE techniques and is very effective in detecting damage in the form of geometrical discontinuities. To detect damage in a one-dimensional bar, Pines (1997) addressed the advantages of wave propagation models over finite element techniques in that the former has higher fidelity of detecting small changes in mass or stiffness. With the acousto-ultrasonic technique, Russell-Floyd and Phillips (1988) investigated statistically the parameter called “stress-wave factor” for detecting damages in carbon-fiber-reinforced composite. At the 0.1% significant level, holes within 4 mm in a 20-ply laminate was detected. Attenuation and dispersion of elastic waves in randomly cracked solids were investigated by Zhang and Gross (1993). Effects of the micro-crack density, the micro-crack orientation or the direction of wave incidence, and the wave frequency on the

attenuation coefficient and the effective wave velocity are exploited to identify the statistical distribution and orientation of micro-cracks. Mouritz *et al*. (2000) studied the low-frequency pulse-echo ultrasonics for fatigue detection in thick polymer composites. Damages consist of debonding of surface glass fibers and a combination of cracks and delaminations within the composite. The ability to detect damage improves with increasing thickness of the composite. In a paper by Van Den Abeele *et al*. (2001) micro-scale damage in a micro-inhomogeneous material were detected by means of nonlinear elastic wave spectroscopy. It is shown that distortion in acoustic and ultrasonic waves with nonlinear features can be used to detect cracks and flaws more reliably than linear acoustical methods (measures of wave speed and dissipation). Krawczuk (2002) combined the wave propagation approach with a genetic algorithm and the gradient technique to detect a transverse open crack on a beam-like structure modeled with spectral finite elements. Damage detection is performed in frequency domain. Similarly by the wave propagation and the spectral element method, Palacz and Krawczuk (2002) also investigated damage detection of a cracked rod. Moreover, wave propagation is used to detect delaminations in beam structures by the group of researchers (Ostachowicz *et al*., 2004). Trifunac *et al*. (2003) recorded low frequency wave numbers in a seven-story reinforced concrete building to eleven earthquakes. A significant and permanent increase of wave numbers is related to damage that increases with the number of earthquakes, and the wave numbers can indicate the location of damage. In another civil infrastructure application, Ma and Pines (2003) used dereverberated transfer functions by eliminating wave reflections to extract local dynamic characteristics for damage detection in a three-story building. With seismic wave excitation, this method is shown to be able to locate damage, determine its type and quantify its severity.

It is worth mentioning that, within guided ultrasonic wave propagation, Lamb waves are extensively used as an effective tool for damage detection by inspecting changes in the received waveforms. Lamb waves are basically two-dimensional propagating vibrations in plates (Viktrov, 1967) with mathematical equations originally formulated by Horace Lamb (Lamb, 1917). The velocities of Lamb waves depend on the frequency and the thickness of the plate, or the dispersion relation. While the fundamental symmetric mode is often used to detect surface cracks in metallic structures, the fundamental anti-symmetric mode is widely

used for damage detection in composites due to its sensitivity to delaminations. For instance, Chimenti and Martin (1991) applied Lamb waves in graphite-epoxy laminates to detect various defects such as delamination, porosity, ply gap, foreign matter and changes in fiber volume fraction. Tan *et al*. (1995) compared Lamb waves with the normal incidence pulse-echo approach for detecting delaminations near the surface of a composite plate. Changes in the Lamb wave amplitude are used to determine both the size and depth of the delamination. Another comparison between Lamb wave tomography conventional C-scan techniques was carried by Jansen *et al*. (1994) in detecting fiber failure, matrix cracking and delamination of polymer composite plates. More recently, piezoelectric materials are widely used as transducers in Lamb wave techniques. Kessler *et al*. (2002) used piezoceramic actuators to provide Lamb wave scans in damage detection on various composite structures (laminated plates, sandwich beams, cylinders, and plates with stiffeners). It is shown that Lamb wave techniques provide more information about damage type, severity and location than frequency response techniques. In another paper, a linear array of piezoceramic patches are attached on the surface of a composite structure to generate and monitor the interaction of Lamb waves in order to detect defects or damages (Diamanti *et al*., 2002). Furthermore, wavelet techniques are used to process the data of Lamb wave response generated by embedded piezoceramic transducers (Paget *et al*., 2002). Neural networks are widely implemented for data processing and decision making in damage detection (e.g., Liu and Sun, 1997; Liu *et al*., 1999; Lloyd and Wang, 1999; Lopes *et al*., 1999; Chang *et al*., 2002). A large number of publications about using Lamb waves for damage detection can be found in recent conferences and journals.

2.1.2 Non Model-based versus Model-based

Depending on whether or not mathematical models (analytical or finite element models) are explicitly used as the reference or baseline, SHM techniques can be grouped into two categories. Due to the well-established experimental modal analysis, evaluation of modal parameters for damage detection could rely only on experimental measurements without using a mathematical model. Examination on input/output data for damage sensitive features usually requires no models for the damaged structure. Examples include the methods by

modal sensitivities, the flexibility methods and the impedance-based methods as mentioned above. Non model-based techniques can avoid errors and uncertainties inherent during most modeling processes; computational errors and sometimes time-consuming burdens could also be eliminated. The disadvantage is that it is very difficult to locate and even quantify damage with most non model-based techniques as indicated by the impedance-based methods.

Damage may be detected by inspecting the local strain changes using fiber optic sensors, especially the fiber Bragg gating (FBG) sensors. Mathematical models of the target structure are not necessarily constructed before or after the inspection for the purpose of damage detection. FBG sensors have a great potential in SHM with many advantages such as high sensitivity and accuracy, immunity to electromagnetic and radiation interferences, easily embedded or coated to structures, ease to be multiplexed, low transmission loss and low cost. A FBG is a longitudinal periodic variation of refractive index that is formed in the core of an optical fiber due to exposure to interfering UV laser beams. The grating pattern acts as a fine narrow-band filter in the way that the back reflected is only a tiny part of the spectrum around the wavelength called the Bragg wavelength. The shift in Bragg wavelength is approximately linear to the strain and temperature change. A local strain can be determined by the grating bound to the structure at the point of interest, and multiple gratings with well-separated Bragg wavelengths in a single fiber provide straightforward multiplexing, a favorable feature for monitoring strains at a local point or area in SHM. Johnson *et al*. (1999) used a multi-channel FBG sensor system for monitoring bending motions, local strain concentrations and dynamic strain response of a composite hull, to facilitate further on-line SHM of a navel vessel in service. Moerman *et al*. (1999) set up a remote monitoring system with FBG sensors for a civil structure, and obtained good results of measuring strains during a tensile test as well as a bending test. It is shown that FBG sensors are also capable of monitoring shrinkage and creep deformations. A series of papers presented in 2002 at the first European SHM workshop addressed the application of FBG sensors, such as the crack detection in composites (Okabe *et al*., 2002) and detection of static and dynamic strains (Calabro *et al*., 2002; James *et al*., 2002; Cheng *et al*., 2002; Kang *et al*., 2002). More recently at the second European SHM workshop 26 papers were presented on various applications of fiber optic sensors for SHM, especially the FBG sensors. For instance,

Cusano *et al*. (2004) performed modal analysis of an aircraft wing with embedded FBG sensors and compared results obtained by accelerometers. A similar experiment on a beam sample was done by Zonta *et al*. (2004) in order to identify damage by the measurement of curvature mode shapes. Betz *et al*. (2004) discussed a damage identification system involving Lamb wave excitations and the detection of linear strain components with FBG sensors. Experiment on an aluminum structure was conducted with damage simulated by drilling holes on it. Fiber optic sensors other than the FBG sensors for SHM were also reported, from the earlier techniques of directly monitoring light power loss due to damages (Crane and Gagorik, 1984; Hofer, 1987; Glossop *et al*., 1990), to recent advances in using fiber optic interferometry (Elvin *et al*., 1999; Xu *et al*., 2003) for delamination detection. Fiber optic sensors are very promising in the development of future on-line SHM systems.

On the other hand, most vibration-based techniques tend to use mathematical models for either numerical verification or comparison to experimental results, whenever these models can be formulated to a certain confidence level. While having disadvantages mentioned earlier, model-based approaches do have advantages in many aspects (Carneiro, 2000): 1) once updated with experimental data, the model permits implementation of many parameter identification methods and may reduce the amount of experimental data required; 2) off-line simulations of system responses with slight variations in parameters and boundary conditions can be inexpensive as well as informative for pre-testing considerations; 3) models can be utilized to optimize the number and location of sensors and actuators; 4) a large amount of data can be generated inexpensively for further analysis, such as training a neural network in SHM. Moreover, with a feasible model available, it becomes possible to predict the remaining life of a damaged structure with the knowledge of damage growth mechanism and operational conditions.

For damage identification on fundamental structure elements (e.g., rods, shafts, pipes, beams, plates and trusses), finite element or spectral element methods are widely used for most model-based techniques. While these structural elements can be modeled relatively accurately in terms of their static and dynamic properties, incorporating damage mechanisms into the model to reveal the dynamics of a damaged structure could be a great challenge.

Damages of different formats (crack, corrosions, debonding, delamination, etc.) and geometry (single crack or distributed cracks; straight crack or curved crack, etc.), and at different locations (welded joints, around holes, near boundaries, etc.) may possess distinct dynamics in different structures.

In terms of modeling cracks in a beam-type structure made of homogenous and isotropic materials, most techniques to date can be grouped to three categories: finite element methods, continuous (analytical) models and discrete-continuous models. Ostachowicz and Krawczuk (2001) provided a comprehensive survey on modeling of a single crack. A crack in finite element methods is usually modeled by a stiffness reduction in the element (Yuen, 1985), by refining meshes around the crack tip (Markstrom and Storakers, 1980), by moving nodes toward the crack tip at the quarter point to account for stress singularity (Shen and Pierre, 1990), or by constructing a special crack element (Gounaris and Dimarogonas, 1988; Krawczuk and Ostachowicz, 1993). Friswell and Penny (2002) compared methods in these three categories for crack effects on a beam structure, and concluded that simple models considering crack flexibility are adequate to detect cracks in SHM. Finite element methods allow more complicated structures that have internal or surface cracks. However, the results as well as interpretation on the results may vary largely with different elements, schemes, and even users involved. In the continuous model class, Barr (1966) extended the Hu-Washizu variational principle for dynamic problems. The so-called Hu-Washizu-Barr variational principle is further investigated by Christides and Barr (1986) for torsional vibration of cracked beams, by Shen and Pierre for a pair of symmetric cracks (1990) and a single edge crack (1994) on a Bernoulli-Euler beam, and by Carneiro (2000) for a single crack on a Timoshenko beam. A set of exponential stress disturbance functions are constructed to account for the stress singularity ahead of the crack tip, and the stress/strain concentration is integrated into the partial differential equations. The main limitation of this approach, as indicated by Ostachowicz and Krawczuk (2001), is that the coefficients in the stress disturbance functions still need to be determined by experiments or finite element methods.

The discrete-continuous models are by far the most commonly used models in dynamic analysis of cracked beams. The basic concept is the introduction of additional boundary

conditions at the crack location where two intact beams are connected with a flexibility matrix whose components are determined by linear fracture mechanics. Hence, the most important work by this approach is to determine the local flexibility matrix. Dimarogonas and Massouros (1981) determined the compliance of torsional mode in a shaft that has a circumferential crack. Anifantis and Dimarogonas (1983) calculated a flexibility matrix for a beam of rectangular cross section and with a single edge crack. It is used to study the stability of a cracked column to follower and vertical loads. A complete 6×6 flexibility matrix for a crack in a beam of rectangular or circular cross section can be found in a series of papers published by Dimarogonas and his co-workers in last two decades. The main limitation of the flexibility approach is that it can only be applied to one-dimensional problems and works well mostly for fundamental structural elements. However, the discrete-continuous crack models are advantageous in many aspects. For instance, the intact part of a structure containing no cracks can still be modeled with corresponding partial differential equations; cracks only increase the boundary conditions that require less computational effort than most finite element methods involving fine meshes around the crack region. The local compliances based on linear fracture mechanics can be verified as well as calibrated with a wealth of experimental data available in literature. The flexibility method can be easily extended to construct special crack elements for finite element analysis. The present research takes advantage of the local flexibility method to investigate an edge crack on a composite beam that vibrates in coupled bending and torsion.

2.2 Vibration of Damaged Composite Laminates

As with other engineering materials, understanding failure mechanisms of composite laminates is very important for real applications involving the design, manufacturing, testing, and damage inspection of composite structures. Of particular interest in the community of structural health monitoring is the dynamic characteristics of composite laminates subjected to some forms of damage. Common damage in composite laminates includes matrix cracking, fiber breakage, fiber-matrix debonding, delamination between plies, and a mixture of any of these incidents (Voyiadjis, 1993). Some defects such as matrix cracking and fiber-matrix debonding are inherent during the fabrication (e.g., air trapped in the resin); they may also

form as initial transient damage under service loading. These defects are usually in micro scale and can rarely distribute to a large area without developing into delamination or transpiercing cracking.

2.2.1 Delamination

Delamination is probably the most important macro-scale failure in composite laminates. Vibration analysis of delaminated composites has been extensively investigated in last a few decades. Zou *et al*. (2000) provided a brief review on delamination detection that is based on various beams models. Ramkumar *et al*. (1979) is usually referred as the first systematic study on the free vibration of delaminated beams. The delaminated beam is modeled by four Timoshenko beams connected at the delamination front cross-sections as shown in Figure 2.1. This is known as the free model since the two sub-laminates (2 and 3 in the figure) separated by the delamination plane are allowed to vibration independently. This model was observed to overestimate the frequency reduction and later improved by Wang *et al*. (1982) by including the coupling between flexural and axial motions of the sub-laminates.

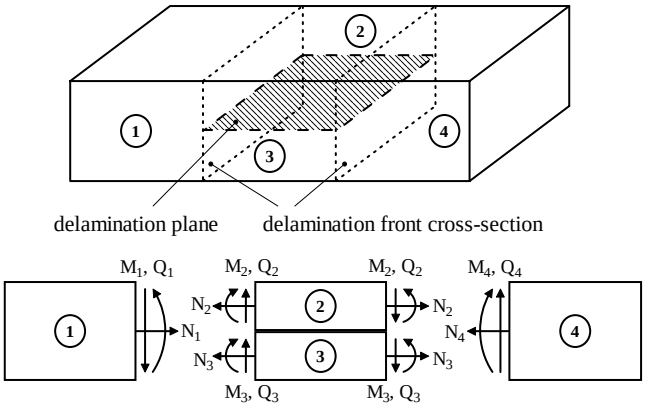

Figure 2.1 The four-beam model of a delaminated beam.

To avoid the physical incompatibility of some overlapping open modes predicted by free models, Mujumdar and Suryanarayan (1988) proposed a so-called constrained mode model in which the continuity of axial displacements and forces at the delamination fronts is ensured. The constrained mode model was further applied to simply-supported beams (Tracy

and Pardoen, 1989) with two different assumptions that, the axial and bending stiffnesses are uncoupled and two sub-laminates are constrained to vibrate together. Each of the four segments is modeled by Euler beam theory. Shen and Grady (1992) investigated with experiments on both models but based on Timoshenko beam theory. There is significant discrepancy between results predicted by the two models. The constrained model predicts frequency change more accurately for some opening modes shown in the experiment even though these modes can not open by the prediction of the model. Luo and Hanagud (2000) considered the nonlinear interaction between the two sub-laminates by adding a piecewise linear spring model that has a uniformly distributed stiffness. Each segment is modeled by Timoshenko beam theory and the bending-extension coupling is also taken into account. The stiffness can then be adjusted for the model to predict more accurate results for the situations where either the free model or the constrained mode model could not work well. A similar concept was later extended by Brandinelli and Massabo (2003) to investigate how a stitching reinforcement to a delamination could improve the dynamic behavior of the delaminated composite plates. An analytical model on the delaminated composite beam involving strain-displacement non-linearity was investigated recently by Luo *et al*. (2004).

Finite element methods are widely used for modeling delaminations in composite laminates. A finite element model using a layer-wise plate theory was proposed by Barbero and Reddy (1991) to study multiple delaminations. The basic assumption is that the same displacement distribution in individual layers is capable of representing the displacement discontinuity at interfaces between layers. Delamination is modeled by the jump discontinuity at the interface. The model indicates an accurate analysis of local effects in delaminated composite plates. However, the computational cost makes it relatively unattractive to predict the global behavior. Sankar (1991) developed a finite element beam model by laminated shear deformable theory. Friction between sub-laminates is considered and spring elements are constructed. Ju *et al*. (1995) presented a finite element model based on the Midlin plate theory. Effects of transverse shear deformation and the coupling between bending and extension are also considered. Composite plates with multiple delaminations, including elliptical delaminations, are investigated. Krawczuk *et al*. (1997a) developed finite element beam and plate models in which the delaminated part is divided into three segments

connected that the tip of the delamination by additional boundary conditions. Their models can be modified to handle delamination in various geometries. Later they investigated composite plates with closing delamination by adding a node-to-node contact model (Zak, *et al*., 2001). Parhi *et al*. (2001) constructed a shell element containing eight nodes with five degrees of freedom per node to investigate vibrations of composite shells with multiple delaminations. Finite element methods for vibration analysis of delaminated composites are also utilized to study dynamics and controls with embedded piezoelectric sensors and actuators, damping effects of the delamination, and delamination detection in SHM.

Other studies include the vibration characteristics of delaminated composite in the state of buckling or post-buckling deformation, such as Yin and Jane (1992), Chen (1994) and Chang and Liang (1998).

2.2.2 Cracking

The stress/strain distribution around the crack region in composite materials has been an important issue in fracture mechanics (Sih and Chen, 1981). While delamination (or "delamination crack" in some earlier papers) in composite laminates contains discontinuity planes parallel to the lamination plane, cracks that received the most investigation in fracture mechanics and structural dynamics usually have planes perpendicular to the laminates, especially for thin structures such as beams, plates and shells. A review paper by Dimarogonas (1996) summarized vibration analysis of cracked structures including some crack identification methods based on vibration signatures. Cracks on composite beams or plates are mostly investigated by the discrete-continuous models and finite element methods mentioned in the last sub-section.

Nikpur and Dimarogonas (1988) derived the energy release rate for a through-thickness crack in beams made of fiber-reinforced composite. Figure 2.2 illustrates the laminated composite beam with a thickness *B*, remotely loaded with six generalized forces. With the formulation of the energy release rate and by Castigliano's theorem, the final compliance matrix has the components expressed by

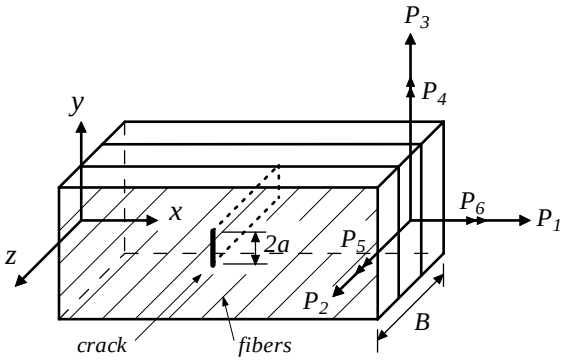

Figure 2.2 A laminated beam segment with a through-thickness crack.

$$c_{ij} = \frac{\partial^2}{\partial P_i \partial P_j} \int_{-a}^{a} \int_{0}^{B} \left\{ D_1 \left(\sum_{n=1}^{6} K_{In} \right)^2 + D_2 \left(\sum_{n=1}^{6} K_{IIn} \right)^2 + D_{12} \left(\sum_{n=1}^{6} K_{In} \right) \left(\sum_{n=1}^{6} K_{IIn} \right) + D_3 \left(\sum_{n=1}^{6} K_{IIIn} \right)^2 \right\} dz d\alpha \tag{2.1}$$

where coefficients D's are determined from the material properties, stacking sequence of laminates and characteristic equation of the beam, and K_{In}, K_{IIn} and K_{IIIn} are stress intensity factors (SIF) of mode I, II and III, respectively, corresponding to the generalized loading P_n. Equation (2.1) is the basis for the flexibility method to be applied for various cracked composite beams and plates.

With equation (2.1) Nikpour (1990a) later studied the vibration of a laminated anisotropic cylindrical shell with a circumferential crack. The shell is modeled with the Donnell-Mushtari-Vlasov theory and the crack introduces four additional boundary conditions at the crack location. Variation of natural frequencies is found to be magnified by the anisotropy of the material in conjunction to the crack effects. The same local flexibility method was also used by the author (Nikpour, 1990b) to investigate the buckling of cracked composite columns. Ghoneam (1995) studied a laminated composite beam with an open crack based on the flexibility concept. However, the formulation of corresponding stress intensity factors does not consider variations due to the material's anisotropy; the same forms for isotropic materials are taken instead. The interaction between mode I and II as shown in equation (2.1) is neglected. Krawczuk and Ostachowicz (1995) analyzed a composite cantilever beam with an open crack in which those neglected by Ghoneam (1995) are

considered. Frequency reduction patterns in terms of the crack location and depth are plotted. A finite element containing the crack is constructed and the results are compared with that obtained by the discrete-continuous model. However, equation (2.1) is misused by taking the summation of the SIF squares for the first two terms in the integral, instead of squares of the SIF summation. Kim and Kim (2003) studied a rotating composite beam with a closing surface crack. The beam rotates around one end in the plane perpendicular to the crack plane. A similar finite element is used for the cracked beam, and the crack may fully open or close as an intact beam at each time step. Again, equation (2.1) is misused in the same way. The equation is correctly used by Song *et al*. (2003) in the study on a cantilever composite beam with multiple surface cracks. The beam is separated by cracks to individual intact Timoshenko beams. The final characteristic matrix has the dimension $(4n+2)\times(4n+2)$ where n is the number of cracks. Numerical results are compared to those by Krawczuk and Ostachowicz (1995). Kisa (2004) addressed on vibration of a cantilever composite Bernoulli-Euler beam with multiple cracks. The finite element method proposed by Krawczuk and Ostachowicz (1995) is taken and solution is sought in modal domain. Results are compared with Krawczuk *et al*. (1997b) for a single crack and Song *et al*. (2003) for multiple cracks. To study a composite plate with an edge crack, Wang and Hwang (1998) applied the concept proposed by Leissa *et al.* (1993) in studying vibrations of circular plates with radial cracks. The two-dimensional displacement field is decomposed to two components, one representing the displacement without the crack and the other representing the singular displacement due to the crack. The problem is finally solved by integrating the vibration of the cracked plate with an assumed displacement across the crack and the non-uniform shear stress distribution along the crack surface. Limited by the measurement method (electronic speckle pattern interferometry), only the tearing mode (III) is taken into account to determine the stress intensity factors.

It is noted from the aforementioned papers addressing cracked composite beams that the laminates are stacking horizontally the same way as shown in Figure 2.2 with the surface through-width crack parallel to the *y*-*z* plane, while the bending vibration is considered as a vertical movement such that each ply experiences the in-plane bending. This is not typically an engineering application, especially for thin beams or plates. In the present research, the

beam laminates have a vertical ply stacking with a through-thickness edge crack. The sequence is symmetric with respect to the mid-plane, balanced or unbalanced. This is modeled to simulate a cracked composite wing so that two vibration modes – bending and torsion – are considered. To date publications on the vibration analysis of cracked composite beams involving coupled bending and torsion modes can not be found in literature, and hence this research could be the first effort on the specific as well as important topic.

2.3 Composite Wing Beam Models

Composite materials have been increasingly used in airplane design with many advantages such as the high strength-to-weigh and stiffness-to-weight ratios, and the isotropic nature in favor of aeroelastic tailoring. Aeroelastic tailoring usually involves the design optimization of a lifting surface to achieve desired aeroelastic responses such as the maximization of flutter and divergence speeds and the improvement of lift and control effectiveness. An accurate and computationally effective model of the composite wing is fundamental in aeroelastic analysis. Although finite element methods seem powerful in many aspects, most often they are too expensive to be coupled with other constrains to provide similar level of details for the preliminary design phase so that a reduced analytical model is still desired to provide insights on aeroelastic phenomena with the total number of states kept as low as possible (Cesnik *et al*., 1996).

It is quite common that one-dimensional beam models with two independent variables (bending and torsion) are used as the analytical method to study the basic aeroelastic phenomena (Bisplinghoff *et al.*, 1996; Fung, 1969). Similarly it is the most popular approach in literature to model a composite wing with a one-dimensional beam or box-beam model. Based on variational principles, Lottati (1985) developed a beam model for a cantilevered wing from an idealized box-beam model in which stiffnesses of bending and torsion as well as stiffness coupling between bending and torsion are derived from laminated composite skins. With the assumption on chordwise rigidity the governing partial differential equation on the bending deflection, $h(y)$, and twisting angle, $\alpha(y)$, is given by

$$EI\frac{\partial^4 h}{\partial y^4}+d_{22}\frac{\partial^4 \alpha}{\partial y^4}+K\frac{\partial^3 \alpha}{\partial y^3}+m\frac{\partial^2 h}{\partial t^2}+mX_\alpha\frac{\partial^2 \alpha}{\partial t^2}=-L$$
$$d_{22}\frac{\partial^4 h}{\partial y^4}-K\frac{\partial^3 h}{\partial y^3}+S\frac{\partial^4 \alpha}{\partial y^4}-GJ\frac{\partial^2 \alpha}{\partial y^2}+mX_\alpha\frac{\partial^2 h}{\partial t^2}+I_\alpha\frac{\partial^2 \alpha}{\partial t^2}=M \quad (2.2)$$

where *EI* and *GJ* are bending and torsional stiffness, respectively; *K* is the coupling stiffness between bending and torsion; *S* is the torsional stiffness due to warping effect; *m* is the mass per unit span; I_α is the cross-sectional mass moment of inertia about the rotation axis; X_α is the offset of mass center from the rotation axis; d_{22} is the coupling term due to the offset between the rotation axis and the reference axis; *L* and *M* are the aerodynamic lifting force and pitching moment, respectively. The two-dimensional displacement field is then obtained from the one-dimensional beam model by the relation $w(x,y)=h(y)+x\alpha(y)$ that was originally suggested by Stein and Housner (1974) to study orthotropic laminates and later extended by Weisshaar (1978, 1981) for symmetrical but unbalanced laminated plates. Weisshaar and Foist (1985) calculated the stiffness parameters *EI*, *GJ* and the coupling term *K* for two different assumptions – zero chordwise moment and zero chordwise curvature (chordwise rigidity). The effective bending stiffness and torsion stiffness as well as a non-dimensional cross-coupling parameter defined by $\Psi = K/\sqrt{EI\cdot GJ}$ are compared with those obtained by box-beam models for different fiber angles. It is shown that the beam model characterized by *EI*, *GJ* and *K* is fairly equivalent to the box-beam model that is usually believed more accurate in modeling composite wings; the model with the assumption of zero chordwise moment predicts these parameters closer to the results by the box-beam model. The beam model is applied by Guo *et al*. (2003) to investigate the effect of laminate lay-up on the flutter speed of composite wing. With the rotation axis offset and warping effects neglected, terms involving d_{22} and *S* in equation (2.2) vanish and the elastic coupling left is the bending-torsion coupling represented by the *K* term. It should be noted, however, two-dimensional thin-walled models or even one-dimensional box-beam models developed in the last decades can be very complicated depending on whether one or more considerations are given on the coupling effects between the extension, in-plane and out-plane bending, twisting, warping of cross section, shear deformation and rotary inertia. For instance, analytical thin-walled closed-section models of various complicities were investigated by Rehfield *et al*. (1990), Chandra *et al*. (1990), Smith and Chopra (1991) and Dancila and Armanios (1998).

On the other hand in the context of aeroelasticity, the aerodynamic loading can also be modeled increasingly sophisticated based on assumptions that may vary between two-dimensional incompressible flow and three-dimensional unsteady flow. Finally, combining the structural model with the aerodynamic model to solve the aeroelastic problem for an analytical solution could be very challenging, e.g., Librescu and Song (1992), Qin *et al*. (2003).

As a study in order to provide insight on the primary effect of cracks on a composite wing, simple structural and aerodynamic models are used in the present research with the further assumption that the inertia axis coincides with the reference axis, which eliminates the inertia coupling shown in equation (2.2). The effect of damage on flutter boundaries was investigated by a few researchers. Chen and Lin (1985) used finite element methods for the flutter characteristics of thin cracked panels. The existence of an edge crack decreases the flutter speed. Strganac and Kim (1996) integrated a damage growth scheme to study the aeroelastic behavior of damaged composite plates. Damage is distributed in the form of matrix cracking in each ply, and a damage parameter is formulated to represent the crack density. The governing equations are solved in time domain. With damage growth, the flutter boundary is first reduced and then leveled off at a certain damage level. The aeroelastic response depends also on the distribution of damage. Bauchau *et al*. (1997) also studied the effect of matrix cracking on flutter characteristics of a composite wing. They concluded that matrix damage does not have significant influence on the flutter speed, but increases the amplitude of aeroelastic oscillations significantly. Realizing that matrix cracking is limited to cross-ply laminates in previous studies, Kim *et al*. (1998) used finite difference and finite element methods to investigate bilinear flutter oscillations of damaged composite plates with angle-ply laminates. Aeroelastic stability is degraded due to the matrix cracking. The degradation is further enhanced by the decrease of the bending-torsion coupling level resulting from the matrix cracking. The effect of an edge crack on the aeroelastic behavior of a composite wing or panel has not been addressed to date, which will be part of the present research. Some results will be presented in Chapter 4.

2.4 Analysis of Model Parameter Uncertainties by Information-gap Theory

The accuracy of structural models, including finite element models now widely used for many engineering problems, are frequently inspected by the correlation between the model prediction and the testing data. In addition to the modeling methodologies themselves, uncertainties in model parameters could be the important source of errors that attract a large amount of research in the community of structural dynamics. Many techniques have been developed under the discipline of model updating to modify or refine structural parameters such as stiffness matrices, geometrical parameters and parameters characterizing boundary conditions in order to improve the prediction from mathematical models (Mottershead and Friswell, 1993). In some cases when the model parameters can be explicitly measured with accuracy at a high confidence level such as the static stiffness of a simple beam element, uncertainty may be analyzed probabilistically with more or less sample data. In other cases when a probabilistic structure can not be established, or stated alternatively that the model parameter is “severely” uncertain, the information-gap decision theory (Ben-Haim, 2001), or info-gap theory in short, could be a good choice to investigate the model robustness as an alternative in model updating. Hemez and Ben-Haim (2004) studied the effect of uncertainties in model parameters on the propagation of a transient impact passing a layer of hyper-elastic material. The info-gap theory is used to model a series of uncertain events with a family of nested sets. Model updating is then performed with the concepts of robustness to uncertainty and opportunity from uncertainty. The authors’ additional work illustrated the relationship between fidelity-to-data, robustness-to-uncertainty and confidence in prediction for model updating (Ben-Haim and Hemez, 2004). It is concluded that in order to assess the predictive accuracy of numerical models, one should not focus only on a single aspect during the model updating procedure. Ben-Haim (2001) provided examples on how model updating can be evaluated in terms of the performance of the system itself. In short, the info-gap theory could be used as a means to understand the model robustness to parameter uncertainties that can not be characterized with probability density functions, and to improve the model performance without loss of robustness.

The last task of the present research investigates the sensitivity of model prediction to the uncertainties in model parameters using the info-gap theory. Since no test data are available for the cracked composite beam model, and model parameters (e.g., *EI*, *GJ* and *K*) are estimated from laminated plate or box-beam model rather than experimentally measured directly, severe uncertainty may exist. Some results are presented in Chapter 6.

Chapter 3

Free Vibration of a Cracked Composite Beam with Coupled Bending-Torsion

3.1 Introduction

One-dimensional beam or box-beam models are widely used as the analytical approach to investigate the primary aeroelastic phenomena during the initial design of an aircraft wing. The most important variables that affect the aerodynamic forces as well as the wing's dynamics are the flexural deflection along the wingspan and the twisting of camber about a spanwise axis. The bending and torsion modes of a wing structure are usually coupled, elastically and/or inertially, due to non-uniform and asymmetric configurations. For a wing made of laminated composites, the most significant elastic parameters in one-dimensional beam models are the bending stiffness parameter, the torsional stiffness parameter and the bending-torsion coupling. These parameters can be determined experimentally or calculated by classical laminated plate theory. Although other elastic interactions such as extension-bending coupling, warping of cross section, rotary inertia and shear deformation exist in composite laminates, they are relatively less significant than the bending-torsion coupling in terms of their effects to the aeroelastic stability of a composite wing. Therefore these interactions are neglected in the present research. As a primary study on the crack effect for a composite wing, a composite beam model involving bending, torsion and their coupling is considered in this chapter.

Vibrations of cracked composite beams, either in Bernoulli-Euler type considering only bending movement or in Timoshenko type with shear deformation and rotary inertia included, have been investigated by a few researchers. Until the present research no published papers could be found addressing the analytical modeling on vibrations of cracked beams with coupled bending-torsion. Based on linear fracture mechanics and Castigliano's theorem, the local flexibility approach is implemented to model the crack. Correction on stress intensity factors due to the anisotropic nature of composite materials will be given. Stiffness and coupling parameters of the composite beam are calculated based on the coupled bending-torsion model presented by Weisshaar (1985). The additional boundary conditions are then determined following the governing differential equations. Unidirectional fiber-reinforced composite is assumed to investigate the effects of anisotropic properties. Analytical solutions with the first few natural frequencies and mode shapes are presented for a cantilever beam.

3.2 Local Flexibility Matrix

A crack on an elastic structure introduces a local flexibility that affects the dynamic response of the system and its stability. To establish the local flexibility matrix of the cracked member under general loading, a prismatic bar with a transverse surface crack is considered as shown in Figure 3.1 below. The crack has a uniform depth along z-axis and the bar is loaded with an axial force P_1, shear forces P_2 and P_3, bending moments P_4 and P_5, and a torsional moment P_6.

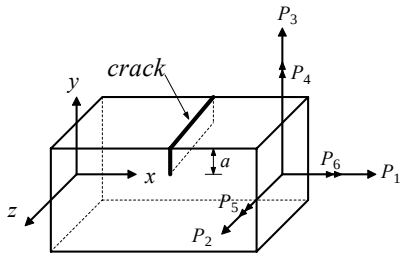

Figure 3.1 A prismatic bar with a uniform surface crack under generalized loading conditions.

Let the additional displacement be u_i along the direction of loading P_i and U the strain energy due to the crack. The additional displacement and strain energy are related by Castigliano's theorem as

$$u_i = \frac{\partial U}{\partial P_i} \tag{3.1}$$

where U has the form $U = \int_0^a J(\alpha)d\alpha$; $J(\alpha) = \partial U / \partial \alpha$ is the strain energy release rate; a is the crack depth. By the Paris' equation $u_i = \partial(\int_0^a J(\alpha)d\alpha)/\partial P_i$, the local flexibility matrix $[c_{ij}]$ per unit width has the components

$$c_{ij} = \frac{\partial u_i}{\partial P_j} = \frac{\partial^2}{\partial P_i \partial P_j}\int_0^a J(\alpha)d\alpha \tag{3.2}$$

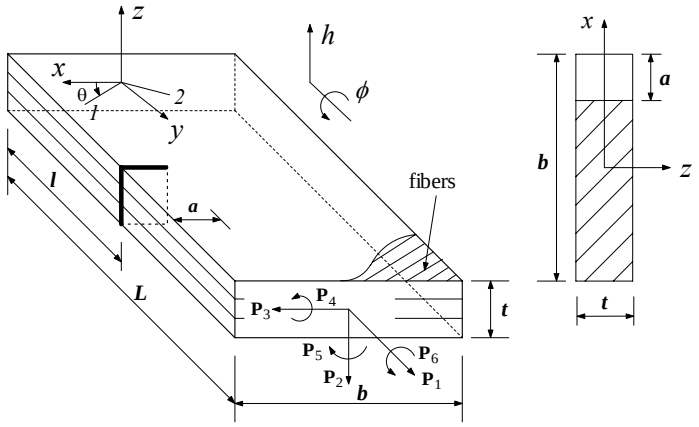

Figure 3.2 A unidirectional fiber-reinforced composite beam with an open edge crack.

Figure 3.2 illustrates a fiber-reinforced composite beam with an edge surface crack and unidirectional plies. For an isotropic composite material, Nikpour and Dimarogonas (1988) derived the final equation for the strain energy release rate $J(\alpha)$ as

$$J = D_1\left(\sum_{n=1}^{6} K_{In}\right)^2 + D_2\left(\sum_{n=1}^{6} K_{IIn}\right)^2 + D_{12}\left(\sum_{n=1}^{6} K_{In}\right)\left(\sum_{n=1}^{6} K_{IIn}\right) + D_3\left(\sum_{n=1}^{6} K_{IIIn}\right)^2 \tag{3.3}$$

where K_{In}, K_{IIn}, and K_{IIIn} are stress intensity factors (SIF) of mode I, II and III, respectively, corresponding to the generalized loading P_n. Here, mode I is the crack opening mode in

which the crack surfaces move apart in the direction perpendicular to the crack plane, while the other two are associated with displacements in which the crack surfaces slide over one another in the direction perpendicular (mode II, or sliding mode), or parallel (mode III, or tearing mode) to the crack front. D_1, D_2, D_{12} and D_3 are constants defined by

$$D_1 = -\frac{\overline{A}_{22}}{2}\mathrm{Im}\left(\frac{\mu_1+\mu_2}{\mu_1\mu_2}\right);\ D_2 = \frac{\overline{A}_{11}}{2}\mathrm{Im}(\mu_1+\mu_2);$$
$$D_{12} = \overline{A}_{11}\,\mathrm{Im}(\mu_1\mu_2);\ D_3 = \frac{1}{2}\sqrt{A_{44}A_{55}}, \tag{3.4}$$

with μ_1 and μ_2 the roots of the characteristic equation (A.1) in Appendix A. Coefficients $\overline{A}_{11}$, $\overline{A}_{22}$, A_{44} and A_{55} are also given in Appendix A. Note in equation (3.3) the first two modes are mixed while the third mode is uncoupled with the first two modes if the material has a plane of symmetry parallel to the *x*-*y* plane, which is the case under investigation.

In general the SIFs K_{jn} (j = I, II, III) can not be taken as the same formats as the counterparts of isotropic material with the same geometry and loading. Bao *et al*. (1992) suggested that K_{jn} (j = I, II, III) for a crack in a fiber-reinforced composite beam can be expressed as

$$K_{jn} = \sigma_n\sqrt{\pi a}F_{jn}(a/b, \tau^{1/4}L/b, \zeta) \tag{3.5}$$

where σ_n is the stress at the crack cross section due to the n^{th} independent force; a is the crack depth; F_{jn} denotes the correction function; L and b are the beam length and width, respectively; τ and ζ are dimensionless parameters taking into account the in-plane orthotropy, which are defined by

$$\tau = \frac{E_{22}}{E_{11}},\ \zeta = \frac{\sqrt{E_{22}E_{11}}}{2G_{12}} - \sqrt{\nu_{12}\nu_{21}} \tag{3.6}$$

where the elastic constants E_{22}, E_{11}, G_{12}, ν_{12} and ν_{21} are given in Appendix A.

Following the paper by Bao *et al*. (1992) the term related to $\tau^{1/4}L/b$ is negligible for $\tau^{1/4}L/b \geq 2$. This condition is fulfilled for the fiber-reinforced composite beam in which the aspect ratio *L/b* is greater than 4. The SIF in equation (3.5) is then reduced to the form

$$K_{jn} = \sigma_n \sqrt{\pi a} Y_n(\zeta) F_{jn}(a/b) \tag{3.7}$$

where $Y_n(\zeta)$ takes into account the anisotropy of the material, and $F_{jn}(a/b)$ takes the same form as in isotropic material and can be found in the handbook by Tada *et al*. (2000) for different geometry and loading modes.

For the unidirectional fiber-reinforced composite beam, the SIFs become:

$$K_{I1} = \sigma_1 \sqrt{\pi a} Y_I(\zeta) F_1(a/b),\ \sigma_1 = \frac{P_1}{bt};$$

$$K_{I4} = \sigma_4 \sqrt{\pi a} Y_I(\zeta) F_1(a/b),\ \sigma_4 = \frac{12P_4}{bt^3} z;$$

$$K_{I5} = \sigma_5 \sqrt{\pi a} Y_I(\zeta) F_2(a/b),\ \sigma_5 = \frac{6P_5}{bt^2};$$

$$K_{I2} = K_{I3} = K_{I6} = 0;$$

$$K_{II3} = \sigma_3 \sqrt{\pi a} Y_{II}(\zeta) F_{II}(a/b),\ \sigma_3 = \frac{P_3}{bt}; \tag{3.8}$$

$$K_{II1} = K_{II2} = K_{II4} = K_{II5} = K_{II6} = 0;$$

$$K_{III2} = \sigma_2 \sqrt{\pi a} Y_{III}(\zeta) F_{III}(a/b),\ \sigma_2 = \frac{P_2}{bt};$$

$$K_{III6} = \sigma_6 \sqrt{\pi a} Y_{III}(\zeta) F_{III}(a/b),\ \sigma_6 = \frac{24P_6\pi^3}{\pi^5 bt^2 - 192t^3} \cos\left(\frac{\pi}{t} z\right);$$

$$K_{III1} = K_{III3} = K_{III4} = K_{III5} = 0$$

where,

$$F_1(a/b) = \sqrt{\frac{\tan\lambda}{\lambda}} \left[0.752 + 2.02(a/b) + 0.37(1-\sin\lambda)^3\right] / \cos\lambda,\ \lambda = \frac{\pi a}{2b};$$

$$F_2(a/b) = \sqrt{\frac{\tan\lambda}{\lambda}} \left[0.923 + 0.199(1-\sin\lambda)^4\right] / \cos\lambda;$$

$$F_{II}(a/b) = \left[1.122 - 0.561(a/b) + 0.085(a/b)^2 + 0.18(a/b)^3\right] / \sqrt{1-a/b};$$

$$F_{III}(a/b) = \sqrt{\frac{\tan\lambda}{\lambda}};$$

and

$$Y_I(\zeta) = 1 + 0.1(\zeta - 1) - 0.016(\zeta - 1)^2 + 0.002(\zeta - 1)^3;$$

$$Y_{II}(\zeta) = Y_{III}(\zeta) = 1.$$

In equation (3.8), σ_6 is the stress along the short edge of the cross section, determined with the classical theory of elasticity as follows.

Consider the beam with rectangular cross section as shown in Figure 3.2 for stress analysis under the torsional moment T (= P_6 while $P_{1\sim5}$ = 0). With $b > t$, the stress distribution on the cross section can be found in the classical theory of elasticity. Denote σ_6 with engineering notation on shear stress τ_{yz}. Specifically the stress along the short edge can be found (Sokolnikoff, 1983) to be

$$\tau_{yz}\Big|_{x=\pm\frac{b}{2}} = \frac{8t}{\pi^2}\mu\alpha\sum_{n=0}^{\infty}\left[\frac{(-1)^n}{(2n+1)^2}\frac{\sinh(k_n \pm b/2)}{\cosh(k_n b/2)}\cos(k_n z)\right] \tag{3.9}$$

where $k_n = (2n+1)\pi/t$, and $\mu\alpha$ relates to the torsional moment by

$$T = \mu\alpha\left(\frac{bt^3}{3} - \frac{64t^4}{\pi^5}\sum_{n=0}^{\infty}\frac{\tanh(k_n b/2)}{(2n+1)^5}\right). \tag{3.10}$$

For $b/t > 2$ and $1 > \tanh(\pi b/2t) > 0.9963$, truncating the series in equations (3.9-10) with the first term will result 92% and 99.5% accuracy of the analytical solution for the stress and moment, respectively. With only the first term in both summations along with the approximation $\tanh(\pi b/2t) = 1$, eliminating $\mu\alpha$ in equations (3.9-10) and taking the magnitude of the stress along the short edge yields

$$\tau_{yz} = \frac{24T\pi^3}{\pi^5 bt^2 - 192t^3}\cos\left(\frac{\pi}{t}z\right). \tag{3.11}$$

For the composite beam with an edge crack shown in Figure 3.2 equation (3.2) becomes

$$c_{ij} = \frac{\partial^2}{\partial P_i \partial P_j}\int_{-t/2}^{t/2}\int_0^a J(\alpha)\,d\alpha\,dz. \tag{3.12}$$

Substitution of equation (3.3) into (3.12) yields

$$c_{ij} = \frac{\partial^2}{\partial P_i \partial P_j}\{\int_{-t/2}^{t/2}\int_0^a [D_1(K_{I1} + K_{I4} + K_{I5})^2 + D_2 K_{II3}^2 + D_{12}(K_{I1} + K_{I4} + K_{I5})K_{II3} + D_3(K_{III2} + K_{III6})^2]d\alpha dz. \tag{3.13}$$

For the composite beam under consideration, there are two independent variables – the transverse and torsional displacements, and one dependent variable – the rotational displacement of the cross section. Correspondingly the external forces the beam could take are the bending moment (P_4 in Figure 3.2), the shear force (P_2) and the torsional moment (P_6). Out of all components in the flexibility matrix only those related to i, j = 2, 4, 6 are needed. It is easily to show that the matrix [C] is symmetric and $c_{24} = c_{46} = 0$. Based on equations (3.8) and (3.13) the components of interest in the local flexibility matrix [C] become:

$$c_{22} = \frac{2\pi D_3}{b^2 t}\int_0^a \alpha[F_{III}(\alpha/b)]^2 d\alpha = \frac{2\pi D_3}{t}\Lambda_{III};$$

$$c_{44} = \frac{24\pi D_1}{b^2 t^3}\int_0^a \alpha[F_1(\alpha/b)]^2 d\alpha = \frac{24\pi D_1 Y_I^2}{t^3}\Lambda_1;$$

$$c_{66} = \frac{\pi D_3 (24\pi^3)^2 t}{(\pi^5 b t^2 - 192 t^3)^2}\int_0^a \alpha[F_{III}(\alpha/b)]^2 d\alpha = \frac{576 D_3 \pi^7 b^2 t}{(\pi^5 b t^2 - 192 t^3)^2}\Lambda_{III}; \tag{3.14}$$

$$c_{26} = c_{62} = \frac{96\pi^3 D_3}{b(\pi^5 b t^2 - 192 t^3)}\int_0^a \alpha[F_{III}(\alpha/b)]^2 d\alpha = \frac{96\pi^3 D_3 b}{\pi^5 b t^2 - 192 t^3}\Lambda_{III};$$

where the dimensionless coefficients

$$\Lambda_{III} = \int_0^{\bar{a}} \bar{\alpha} F_{III}^2(\bar{\alpha}) d\bar{\alpha},\ \Lambda_1 = \int_0^{\bar{a}} \bar{\alpha} F_1^2(\bar{\alpha}) d\bar{\alpha} \text{ and } \bar{a} = a/b.$$

The final flexibility matrix at the crack location for the coupled bending and torsional vibration is then

$$[C] = \begin{bmatrix} c_{22} & 0 & c_{26} \\ 0 & c_{44} & 0 \\ c_{26} & 0 & c_{66} \end{bmatrix} \tag{3.15}$$

with components given in equation (3.14). Note the off-diagonal term c_{22} (= c_{62}) indicates the coupling between bending and torsion due to the presence of the crack.

3.3 The Composite Beam Model with Coupled Bending-Torsion

In the preliminary design, it is quite common that an aircraft wing is modeled as a slender beam or box to study the bending-torsion characteristics. Weisshaar (1985) presented an idealized beam model for composite wings describing the coupled bending-torsion with three beam cross-sectional stiffness parameters along a spanwise midsurface reference axis (y-axis): the bending stiffness parameter EI; the torsional stiffness parameter GJ and the bending-torsion coupling parameter K. Note that EI and GJ are not the bending and torsion stiffnesses of the beam since the reference axis is not the elastic axis in general. Figure 3.3 illustrates a beam segment with internal bending and torsional moments.

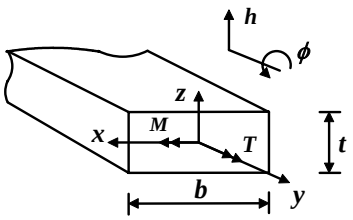

Figure 3.3 A beam segment with internal bending moment, torsional moment and deformations.

The two-dimensional displacement field $w(x, y, t)$ may be represented by a bending deflection $h(y, t)$ along the y-axis and a twisting $\phi(y, t)$ about this axis. At any cross section of the beam the relation between the internal bending moment M, the torsional moment T, and the beam curvature $\partial^2 h/\partial y^2$ and twisting rate $\partial\phi/\partial y$ may be expressed as

$$\begin{Bmatrix} M \\ T \end{Bmatrix} = \begin{bmatrix} EI & -K \\ -K & GJ \end{bmatrix} \begin{Bmatrix} \partial^2 h/\partial y^2 \\ \partial\phi/\partial y \end{Bmatrix}. \tag{3.16}$$

If a coupling measure is defined as $\Psi = K/\sqrt{EI \cdot GJ}$ as in Weisshaar (1985), it has been shown that $-1 < \Psi < 1$ with the magnitude closing to ±1 indicating the highly coupled while $\Psi = 0$ indicates no coupling between bending and torsion.

On the other hand, the relation between the plate bending moments, torsional moment and curvatures can be determined by classical laminated plate theory as

$$\begin{Bmatrix} M_x \\ M_y \\ M_{xy} \end{Bmatrix} = \begin{bmatrix} D_{11} & D_{12} & D_{16} \\ D_{12} & D_{22} & D_{26} \\ D_{16} & D_{26} & D_{66} \end{bmatrix} \begin{Bmatrix} \kappa_x \\ \kappa_y \\ \kappa_{xy} \end{Bmatrix}. \tag{3.17}$$

Following the paper by Weisshaar (1985) the three stiffness parameters in equation (3.16) may be determined for high aspect-ratio beams (assuming $M_x = 0$ but κ_x is not restrained) as

$$\begin{aligned} EI &= b(D_{22} - \frac{D_{12}^2}{D_{11}}); \\ K &= 2b(D_{26} - \frac{D_{12}D_{16}}{D_{11}}); \\ GJ &= 4b(D_{66} - \frac{D_{16}^2}{D_{11}}), \end{aligned} \tag{3.18}$$

where bending stiffnesses D_{11}, D_{22}, D_{66}, D_{12}, D_{16} and D_{26} are given in Appendix A. It may be of interest to know that, for the assumption of chordwise rigidity $w(x, y, t) = h(y, t) - x\phi(y, t)$ (here $\kappa_x = 0$, but $M_x \neq 0$), the second term in each equation of (3.18) disappears and only the first term is left for EI, K and GJ. This is equivalent to the situation that D_{11} tends to infinity, or infinite chordwise rigidity.

Once the parameters EI, K and GJ are obtained, the free vibration of the coupled bending and torsion for the composite beam, with damping, shear deformation and rotary inertia neglected, may be governed by the equation

$$\begin{aligned} EI\frac{\partial^4 h}{\partial y^4} - K\frac{\partial^3 \phi}{\partial y^3} + m\frac{\partial^2 h}{\partial t^2} &= 0 \\ GJ\frac{\partial^2 \phi}{\partial y^2} - K\frac{\partial^3 h}{\partial y^3} - I_\alpha\frac{\partial^2 \phi}{\partial t^2} &= 0 \end{aligned} \tag{3.19}$$

where m is the mass per unit length, I_α the polar mass moment of inertia per unit length about the y-axis.

Using separation of variables $h(y,t) = H(y)e^{i\omega t}$, $\phi(y,t) = \Phi(y)e^{i\omega t}$, equation (3.19) is transferred to

$$\begin{aligned} EIH^{iv} - K\Phi''' - m\omega^2 H = 0 \\ GJ\Phi'' - KH''' + I_\alpha \omega^2 \Phi = 0 \end{aligned} \tag{3.20}$$

where the Roman letter and primes in superscript denote the derivative with respect to the spatial variable. As shown by Banerjee (2001), eliminating either H or Φ in equation (3.20) will yield a general solution in the normalized form

$$\begin{aligned} H(\xi) &= A_1 \cosh\alpha\xi + A_2 \sinh\alpha\xi + A_3 \cos\beta\xi + A_4 \sin\beta\xi + A_5 \cos\gamma\xi + A_6 \sin\gamma\xi \\ \Phi(\xi) &= B_1 \cosh\alpha\xi + B_2 \sinh\alpha\xi + B_3 \cos\beta\xi + B_4 \sin\beta\xi + B_5 \cos\gamma\xi + B_6 \sin\gamma\xi \end{aligned} \tag{3.21}$$

where $A_{1\text{-}6}$ and $B_{1\text{-}6}$ are related by

$$\begin{aligned} B_1 = k_\alpha A_2 / L,\ B_2 = k_\alpha A_1 / L,\ B_3 = k_\beta A_4 / L, \\ B_4 = -k_\beta A_3 / L,\ B_5 = k_\gamma A_6 / L,\ B_6 = -k_\gamma A_5 / L; \end{aligned}$$

and other parameters are defined consequently as

$$k_\alpha = (\bar{b} - \alpha^4) / \bar{k}\alpha^3,\ k_\beta = (\bar{b} - \beta^4) / \bar{k}\beta^3,\ k_\gamma = (\bar{b} - \gamma^4) / \bar{k}\gamma^3,$$

with

$$\bar{k} = -K / EI\ ,$$

$$\alpha = [2(q/3)^{1/2} \cos(\varphi/3) - a/3]^{1/2},$$

$$\beta = [2(q/3)^{1/2} \cos((\pi - \varphi)/3) + a/3]^{1/2},$$

$$\gamma = [2(q/3)^{1/2} \cos((\pi + \varphi)/3) + a/3]^{1/2},$$

$$q = b + a^2/3,$$

$$\varphi = \cos^{-1}[(27abc - 9ab - 2a^3)/(2(a^2 + 3b)^{3/2}],$$

$$a = \bar{a} / c,$$

$$b = \bar{b} / c,$$

$$c = 1 - K^2 / (EI \cdot GJ),$$

$$\bar{a} = I_\alpha \omega^2 L^2 / GJ,$$

$$\bar{b} = m\omega^2 L^4 / EI,$$

$$\xi = y / L\ .$$

Details about solving the sixth-order auxiliary equation resulted from eliminating either H or Φ in equation (3.20) are provided in Appendix B.

Following Banerjee (2001), the expressions for the cross-sectional rotation $\Theta(\xi)$, the bending moment $M(\xi)$, the shear force $S(\xi)$ and the torsional moment $T(\xi)$ are obtained with the normalized coordinate ξ as

$$\begin{aligned}
\Theta(\xi) &= (1/L)[A_1\alpha\sinh\alpha\xi + A_2\alpha\cosh\alpha\xi - A_3\beta\sin\beta\xi \\
&\quad + A_4\beta\cos\beta\xi - A_5\gamma\sin\gamma\xi + A_6\gamma\cos\gamma\xi], \\
M(\xi) &= (EI/L^2)[A_1\bar{\alpha}\cosh\alpha\xi + A_2\bar{\alpha}\sinh\alpha\xi - A_3\bar{\beta}\cos\beta\xi \\
&\quad - A_4\bar{\beta}\sin\beta\xi - A_5\bar{\gamma}\cos\gamma\xi - A_6\bar{\gamma}\sin\gamma\xi], \\
S(\xi) &= -(EI/L^3)[A_1\alpha\bar{\alpha}\sinh\alpha\xi + A_2\alpha\bar{\alpha}\cosh\alpha\xi + A_3\beta\bar{\beta}\sin\beta\xi \\
&\quad - A_4\beta\bar{\beta}\cos\beta\xi + A_5\gamma\bar{\gamma}\sin\gamma\xi - A_6\gamma\bar{\gamma}\cos\gamma\xi], \\
T(\xi) &= (GJ/L^2)[A_1 g_\alpha\cosh\alpha\xi + A_2 g_\alpha\sinh\alpha\xi - A_3 g_\beta\cos\beta\xi \\
&\quad - A_4 g_\beta\sin\beta\xi - A_5 g_\gamma\cos\gamma\xi - A_6 g_\gamma\sin\gamma\xi],
\end{aligned} \tag{3.22}$$

where

$$\bar{\alpha} = \bar{b}/\alpha^2,\ \bar{\beta} = \bar{b}/\beta^2,\ \bar{\gamma} = \bar{b}/\gamma^2,$$

$$g_\alpha = (\bar{b} - c\alpha^4)/\bar{k}\alpha^2,\ g_\beta = (\bar{b} - c\beta^4)/\bar{k}\beta^2,\ g_\gamma = (\bar{b} - c\gamma^4)/\bar{k}\gamma^2.$$

One issue related to the coupled bending-torsion equation (3.19) is that, for the unidirectional composite beam in some specific fiber orientation (e.g. at 0°, 90°), bending and torsion will be decoupled such that equation (3.21) is no longer a valid solution to the eigenvalue problem. Under this situation the coupled equation simply reduces to two independent equations for bending and torsion. Then separation of variables yields

$$\begin{aligned}
EIH^{iv} - m\omega^2 H &= 0 \\
GJ\Phi'' + I_\alpha\omega^2\Phi &= 0
\end{aligned} \tag{3.23}$$

The general solution in the normalized form in this case is

$$\begin{aligned}
H(\xi) &= A_1\cosh\eta\xi + A_2\sinh\eta\xi + A_3\cos\eta\xi + A_4\sin\eta\xi \\
\Phi(\xi) &= B_1\cos\sigma\xi + B_2\sin\sigma\xi
\end{aligned} \tag{3.24}$$

where $\eta = (m\omega^2 L^4/EI)^{1/4}$, $\sigma = (I_\alpha\omega^2 L^2/GJ)^{1/2}$ and m and I_α are defined as in equation (3.19). Again, the expressions for cross-sectional rotation $\Theta(\xi)$, the bending moment $M(\xi)$, the shear force $S(\xi)$ and the torsional moment $T(\xi)$ become

$$\Theta(\xi) = (1/L)[A_1\eta\sinh\eta\xi + A_2\eta\cosh\eta\xi - A_3\eta\sin\eta\xi + A_4\eta\cos\eta\xi],$$

$$M(\xi) = (EI/L^2)[A_1\eta^2\cosh\eta\xi + A_2\eta^2\sinh\eta\xi - A_3\eta^2\cos\eta\xi - A_4\eta^2\sin\beta\xi],$$
$$S(\xi) = -(EI/L^3)[A_1\eta^3\sinh\eta\xi + A_2\eta^3\cosh\eta\xi + A_3\eta^3\sin\eta\xi - A_4\eta^3\cos\eta\xi], \qquad (3.25)$$
$$T(\xi) = (GJ/L^2)[-B_1\sigma\sin\sigma\xi + B_2\sigma\cos\sigma\xi].$$

3.4 Additional Boundary Conditions at the Crack Location

Let the edge crack be located at $\xi_c = l/L$, as shown in Figure 3.2. The beam can be replaced with two intact beams connected at the crack location by the local flexibility matrix. The solution of H and Φ for each intact beam is given next.

When bending and torsion are coupled due to the fiber orientation (not at 0° or 90°), let $\Gamma = [\cosh\alpha\xi \;\; \sinh\alpha\xi \;\; \cos\beta\xi \;\; \sin\beta\xi \;\; \cos\gamma\xi \;\; \sin\gamma\xi]^T$, then

$0 \le \xi \le \xi_c$,

$$H_1(\xi) = [A_1 \;\; A_2 \;\; A_3 \;\; A_4 \;\; A_5 \;\; A_6]\Gamma,$$
$$\Phi_1(\xi) = [B_1 \;\; B_2 \;\; B_3 \;\; B_4 \;\; B_5 \;\; B_6]\Gamma; \qquad (3.26.1)$$

$\xi_c \le \xi \le 1$,

$$H_2(\xi) = [A_7 \;\; A_8 \;\; A_9 \;\; A_{10} \;\; A_{11} \;\; A_{12}]\Gamma,$$
$$\Phi_2(\xi) = [B_7 \;\; B_8 \;\; B_9 \;\; B_{10} \;\; B_{11} \;\; B_{12}]\Gamma. \qquad (3.26.2)$$

There are 12 unknowns in equation (3.26) since $B_{1\text{-}12}$ are related to $A_{1\text{-}12}$ by the relationship in equation (3.21). When bending and torsion are decoupled due to the fiber orientation at 0° or 90°, similarly let $\Gamma_1 = [\cosh\eta\xi \;\; \sinh\eta\xi \;\; \cos\eta\xi \;\; \sin\eta\xi]^T$, $\Gamma_2 = [\cos\sigma\xi \;\; \sin\sigma\xi]^T$, then

$0 \le \xi \le \xi_c$,

$$H_1(\xi) = [A_1 \;\; A_2 \;\; A_3 \;\; A_4]\Gamma_1,$$
$$\Phi_1(\xi) = [B_1 \;\; B_2]\Gamma_2; \qquad (3.27.1)$$

$\xi_c \le \xi \le 1$,

$$H_2(\xi) = [A_5 \;\; A_6 \;\; A_7 \;\; A_8]\Gamma_1,$$
$$\Phi_2(\xi) = [B_3 \;\; B_4]\Gamma_2. \qquad (3.27.2)$$

There are still 12 unknowns in equation (3.27) since $B_{1\text{-}2}$ are not related to $A_{1\text{-}6}$.

At the crack location, $\xi = \xi_c$, the local flexibility concept demands

1) continuity of the bending moment:

$$M_1(\xi_c) = M_2(\xi_c) \tag{3.28.1}$$

2) continuity of the shear force:

$$S_1(\xi_c) = S_2(\xi_c) \tag{3.28.2}$$

3) continuity of the torsional moment:

$$T_1(\xi_c) = T_2(\xi_c) \tag{3.28.3}$$

4) discontinuity of the transverse displacement:

$$H_2(\xi_c) = H_1(\xi_c) + c_{22}S_1(\xi_c) + c_{26}T_1(\xi_c) \tag{3.28.4}$$

5) discontinuity of the cross-sectional rotation:

$$\Theta_2(\xi_c) = \Theta_1(\xi_c) + c_{44}M_1(\xi_c) \tag{3.28.5}$$

6) discontinuity of the torsional angle:

$$\Phi_2(\xi_c) = \Phi_1(\xi_c) + c_{62}S_1(\xi_c) + c_{66}T_1(\xi_c) \tag{3.28.6}$$

For the beam in coupled bending-torsion, each crack will result in 6 additional boundary conditions at the crack location. Note the coupling between the transverse displacement and the torsional angle in equations (3.28.4) and (3.28.6) due to the presence of crack.

3.5 Elastic Parameters of the Composite Beam

The unidirectional composite beam consists of several plies aligned in the same direction. In each ply (and for the whole laminate), the material is assumed orthotropic with respect to its axes of symmetry. Material properties of each ply are taken to be:

Modulus of elasticity: $E_m = 2.76$ GPa, $E_f = 275.6$ GPa;
Poisson's ratio: $\nu_m = 0.33$, $\nu_f = 0.2$;
Modulus of rigidity: $G_m = 1.036$ GPa, $G_f = 114.8$ GPa;
Mass density: $\rho_m = 1600$ kg/m^3, $\rho_f = 1900$ kg/m^3;

where the subscript *m* stands for matrix and *f* for fiber. The geometry of the beam is taken to be: length L = 0.5 m, width b = 0.1 m and thickness t = 0.005m. In the following sections, θ stands for the fiber angle, and V the fiber volume fraction, $\eta = a/b$ the crack ratio, and $\xi_c = l/L$ the dimensionless crack location.

Coefficients of the local flexibility matrix

Once incorporated with the boundary conditions (3.28), the components in the local flexibility matrix given by expression (3.14), may be expressed in dimensionless formats for further comparison. The dimensionless constants become:

$$\bar{c}_{22} = c_{22}\frac{EI}{L^3} = \varepsilon_{22}\Lambda_{III}\text{, with } \varepsilon_{22} = \frac{2\pi D_3 EI}{tL^3};$$

$$\bar{c}_{44} = c_{44}\frac{EI}{L} = \varepsilon_{44}\Lambda_1\text{, with } \varepsilon_{44} = \frac{24\pi D_1 Y_I^2 EI}{t^3 L};$$

$$\bar{c}_{66} = c_{66}\frac{GJ}{L} = \varepsilon_{66}\Lambda_{III}\text{, with } \varepsilon_{66} = \frac{576 D_3 \pi^7 h b^2 GJ}{(\pi^5 bt^2 - 192t^3)^2 L}; \tag{3.29}$$

$$\bar{c}_{26} = c_{26}\frac{GJ}{L^2} = \varepsilon_{26}\Lambda_{III}\text{, with } \varepsilon_{26} = \frac{96\pi^3 D_3 bGJ}{(\pi^5 bt^2 - 192t^3)L^2};$$

$$\bar{c}_{62} = c_{26}\frac{EI}{L^2} = \varepsilon_{62}\Lambda_{III}\text{, with } \varepsilon_{62} = \frac{96\pi^3 D_3 bEI}{(\pi^5 bt^2 - 192t^3)L^2};$$

where Λ_1 and Λ_{III} are dimensionless and defined the same as in equation (3.14). They are functions of crack ratio only ($a/b \in [0, 1]$) and both go to infinity with a/b approaching unity, as shown in Figure 3.4 and 3.5. For a crack ratio close to 1, which means the beam is nearly completely broken, the beam dynamics suffer severe instability and these coefficients may not be used in analyzing vibration characteristics. The following analysis is focused on crack ratios up to 0.9.

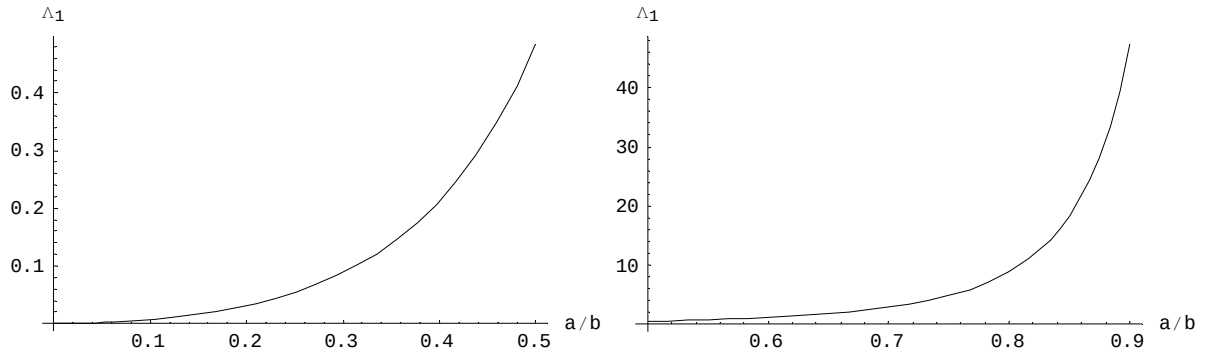

(a) (b)

Figure 3.4 Dimensionless coefficient Λ_1 as a function of the crack ratio a/b: (a) for $a/b \in [0, 0.5]$; (b) for $a/b \in [0.5, 1]$.

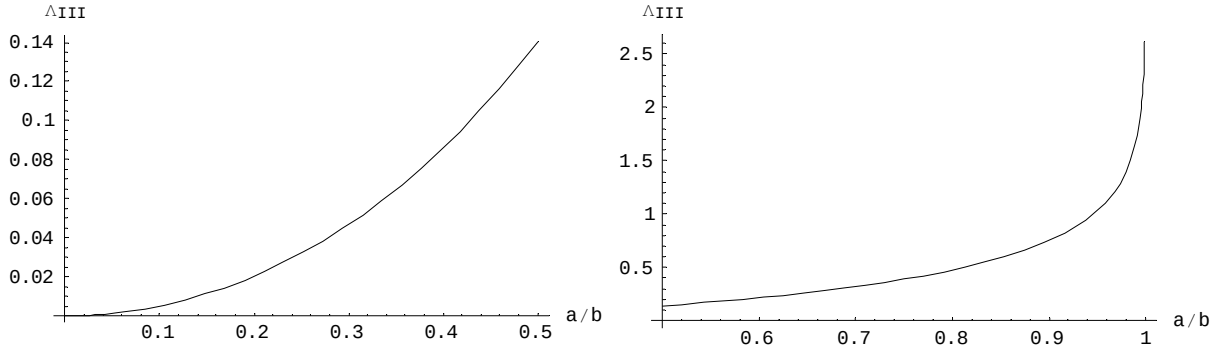

(a) (b)

Figure 3.5 Dimensionless coefficient Λ_{III} as a function of the crack ratio a/b: (a) for $a/b \in [0, 0.5]$; (b) for $a/b \in [0.5, 1]$.

The coefficients $\varepsilon_{22}, \varepsilon_{44}, \varepsilon_{66}, \varepsilon_{26}, \varepsilon_{62}$ are all dimensionless, and are functions of fiber orientation, θ, and volume fraction, V. Their variations are shown in Figure 3.6.

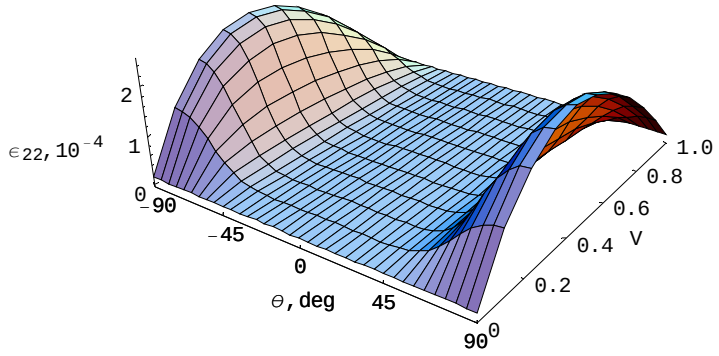

(a) variation of ε_{22}

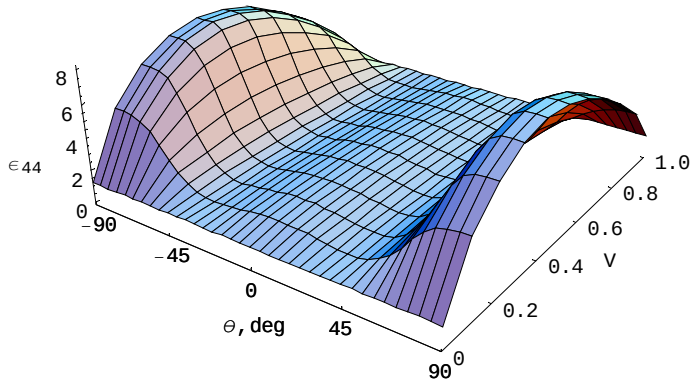

(b) variation of ε_{44}

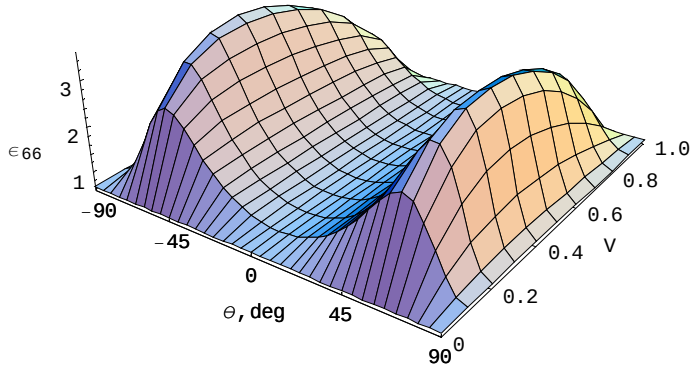

(c) variation of ε_{66}

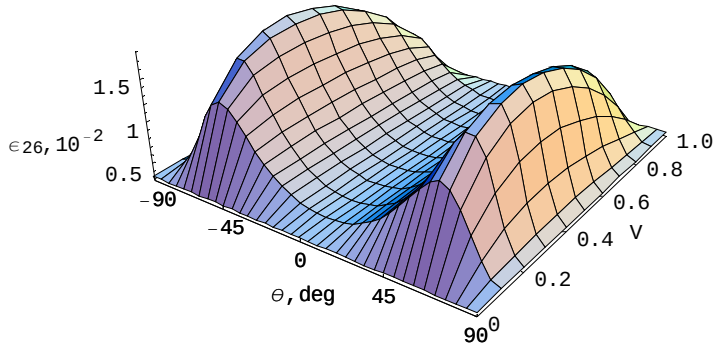

(d) variation of ε_{26}

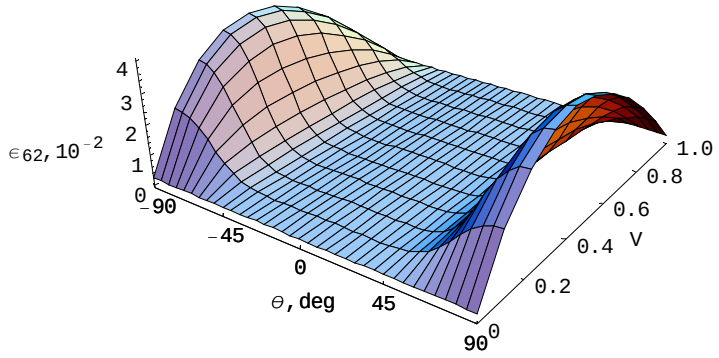

(e) variation of ε_{62}

Figure 3.6 Variation of $\varepsilon_{22}, \varepsilon_{44}, \varepsilon_{66}, \varepsilon_{26}, \varepsilon_{62}$ as a function of the fiber angle (θ) and the volume fraction (V).

It is obvious that coefficients $\varepsilon_{22}, \varepsilon_{44}, \varepsilon_{66}, \varepsilon_{26}, \varepsilon_{62}$ exhibit double symmetry for $\theta = 0°$ and $V = 0.5$. Among these dimensionless coefficients, ε_{44} has the largest magnitude, followed by ε_{66} and then ε_{26} and ε_{62} with the last two accounting for the coupling effects. In other words, the bending or torsional mode is affected most by the internal bending or torsional moment, respectively, whose distribution along the beam has been altered by the surface crack. The internal shear force plays the least important role by noting its relatively low magnitude. The dimensionless Λ_1 and Λ_{III} work as "weighing" factors for the final dimensionless components in the local flexibility matrix. For a crack ratio up to 0.9, Λ_1 is always larger than

Λ_{III} so that the role of the coefficient ε_{44} is further enhanced. Note that in equation (3.29) only $\bar{c}_{44}$ is affected by Λ_1.

As shown in equation (3.29) the coefficients $\varepsilon_{22}, \varepsilon_{44}, \varepsilon_{66}, \varepsilon_{26}, \varepsilon_{62}$ are normalized with either *EI* or *GJ*. The plot of each coefficient shown in Figure 3.6 bears a similar "shape" to that of the normalized stiffness parameter *EI* or *GJ* as shown in Figure 3.7.

Bending and torsional stiffness parameters, and the coupling term

The bending and torsional stiffness parameters, *EI* and *GJ*, are functions of θ and *V*, as shown in Figure 3.7(a) and (c). For θ = 0° or 90° (bending and torsion are decoupled), the torsional stiffness parameter *GJ* has the same variation with respect to the fiber volume fraction. However the bending stiffness parameter varies differently. When normalized by the stiffness of fiber angle at 0°, the dimensionless $EI(\theta, V)/EI(0, V)$ and $GJ(\theta, V)/GJ(0, V)$ are shown in Figure 3.7(b) and (d).

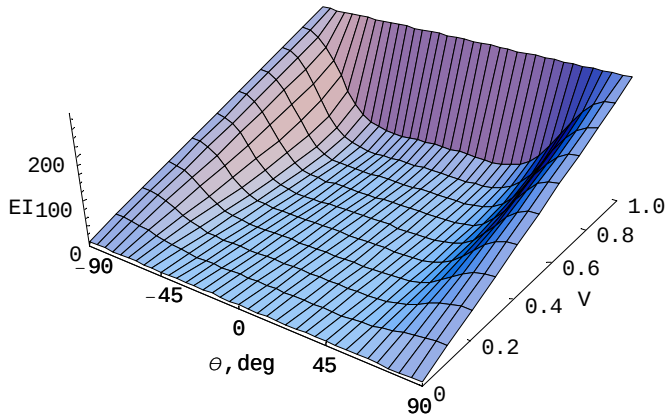

(a) $EI(\theta, V)$, N•m^2

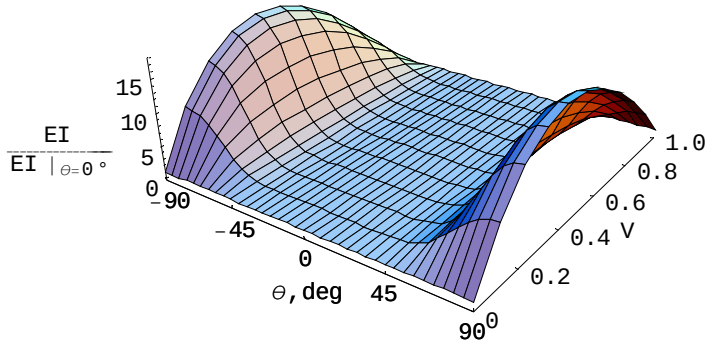

(b) $EI(\theta, V)/EI(0, V)$

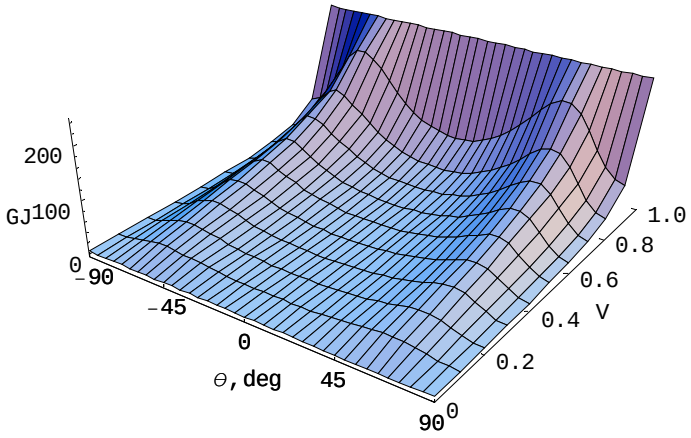

(c) $GJ(\theta, V)$, N•m^2

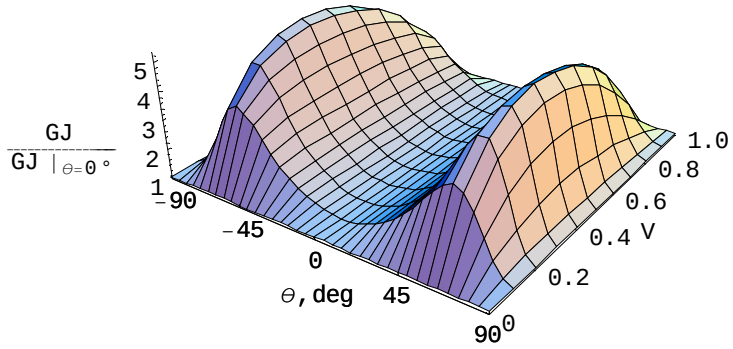

(d) $GJ(\theta, V)/GJ(0, V)$

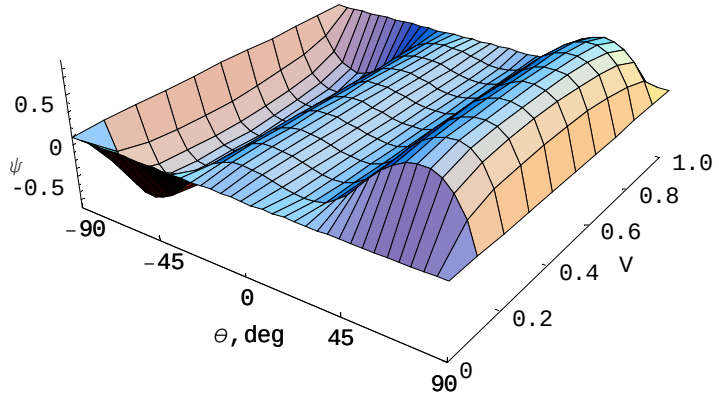

(e) $\Psi = K / \sqrt{EI \cdot GJ}$

Figure 3.7 Various bending and torsional stiffness parameters, and the coupling term as functions of the fiber angle (θ) and the volume fraction (V). Note the regions of strong coupling corresponding to $\theta = \pm 65°$.

The dimensionless coupling measure Ψ, defined by $\Psi = K / \sqrt{EI \cdot GJ}$, is an indication on how "strong" the bending and torsion are coupled, with ±1 indicating the "strongest" coupling while 0 indicating no coupling. Figure 3.7(e) shows the coupling measure with respect to the fiber angle and volume fraction. Bending and torsion are decoupled when θ = 0° or 90°, or V = 0 or 1. For the fiber volume fraction being 0 or 1, the material is isotropic and homogeneous so that bending and torsion is basically decoupled for the beam with rectangular cross section.

As shown in the figure, the "strong" coupling is expected for the fiber angle around ±65°, while the coupling is very "weak" for the angle between ±35°. The variation of the coupling term with respect to the fiber angle agrees with the results presented in Weisshaar (1985). Note that in Figure 3.7 the stiffness parameters (EI and GJ) and the coupling measure (Ψ) are determined by the fiber angle and the volume fraction, and no crack is involved.

Since the stiffness parameters as well as the coupling term are determined by the material properties (θ and V), natural frequencies of the beam will be affected not only by the crack location and its depth, but also by the material properties. The analysis of the natural frequency changes follows. Three situations are selected in terms of the degree of coupling.

3.6 Frequency Changes

In the next two sub-sections the composite beam with an edge crack is assumed to be a cantilever beam with a fixed end at the origin of the *y*-axis. In addition to the six boundary conditions at the crack location, other boundary conditions of the cantilever beam will be:
at the fixed end, $\xi = 0$,

$$H_1(0) = \Theta_1(0) = \Phi_1(0) = 0\,; \tag{3.30.1-3}$$

at the free end, $\xi = 1$,

$$M_2(1) = S_2(1) = T_2(1) = 0\,. \tag{3.30.4-6}$$

Substitution of equation (3.26) into (3.28) and (3.30) will yield the characteristic equation of the initially coupled beam:

$$[\Lambda]A = 0 \tag{3.31}$$

where $A = [A_1\ A_2\ A_3\ A_4\ A_5\ A_6\ A_7\ A_8\ A_9\ A_{10}\ A_{11}\ A_{12}\ ]^T$ and $[\Lambda]$ the 12×12 characteristic matrix being the function of frequency. Substitution of equation (3.27) into (3.28) and (3.30) yields the characteristic equation of the initially decoupled beam:

$$[\overline{\Lambda}]\overline{A} = 0 \tag{3.32}$$

where $\overline{A} = [A_1\ A_2\ A_3\ A_4\ A_5\ A_6\ A_7\ A_8\ B_1\ B_2\ B_3\ B_4\ ]^T$ and $[\overline{\Lambda}]$ still being a 12×12 characteristic matrix.

Solving for $\det[\Lambda] = 0$ or $\det[\overline{\Lambda}] = 0$ yields the natural frequencies. Substituting each natural frequency back into equation (3.31) or (3.32) will give the corresponding mode shape. Note that both the natural frequency and the mode shape now depend not only on the crack depth and location, but also on the material properties (fiber orientation and volume fraction). The bending-torsion coupling described by equation (3.31) arises from both the equation of motion and the crack boundary condition. However, in equation (3.32) only the crack contributes to the coupling between bending and torsion that is initially decoupled by equation (3.23).

A) Natural frequency change as a function of crack ratio and fiber angle

Assume that the crack is located at $\xi_c = 0.3$ and the fiber volume fraction is V = 0.5. The natural frequency will be affected by the crack ratio and fiber angle. The first four natural frequencies are plotted in Figure 3.8 to Figure 3.11.

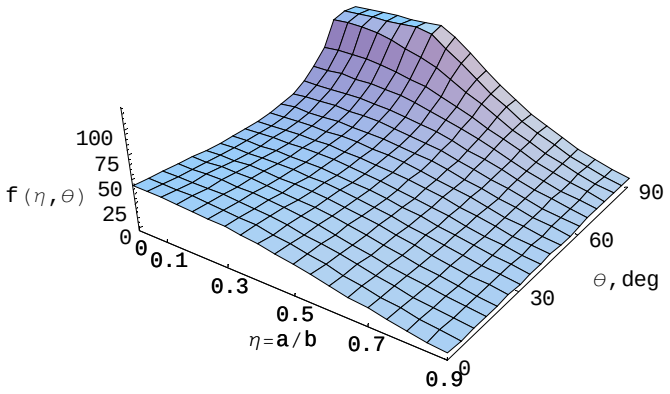

(a) The first natural frequency, rad/s

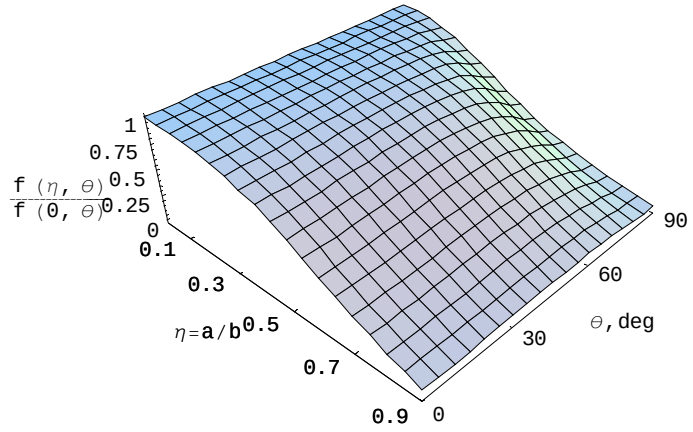

(b) Normalized at $\eta = 0$ for each fiber angle

Figure 3.8 Variation of the first natural frequency as a function of the crack ratio (a/b) and fiber angle (θ).

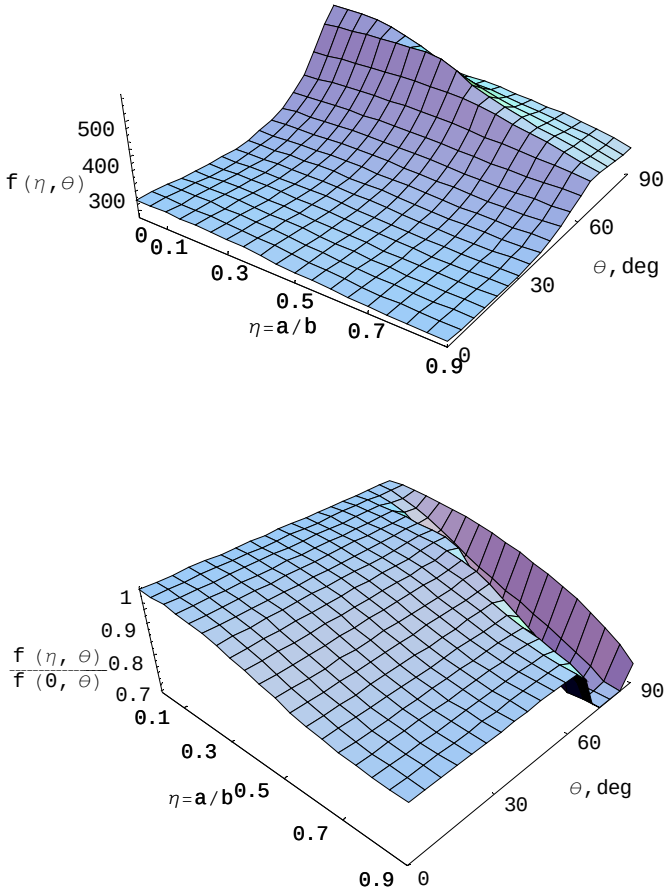

(a) The second natural frequency, rad/s

(b) Normalized at $\eta = 0$ for each fiber angle

Figure 3.9 Variation of the second natural frequency as a function of the crack ratio (a/b) and fiber angle (θ).

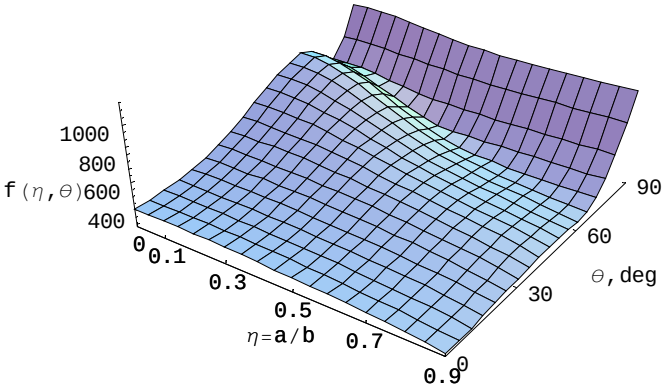

(a) The third natural frequency, rad/s

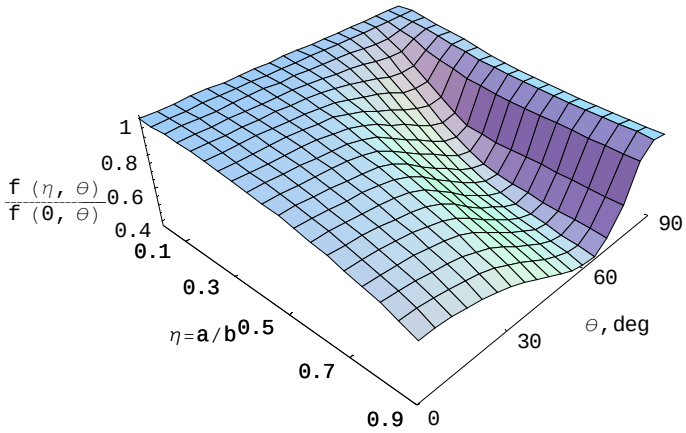

(b) Normalized at $\eta = 0$ for each fiber angle

Figure 3.10 Variation of the third natural frequency as a function of the crack ratio (a/b) and fiber angle (θ).

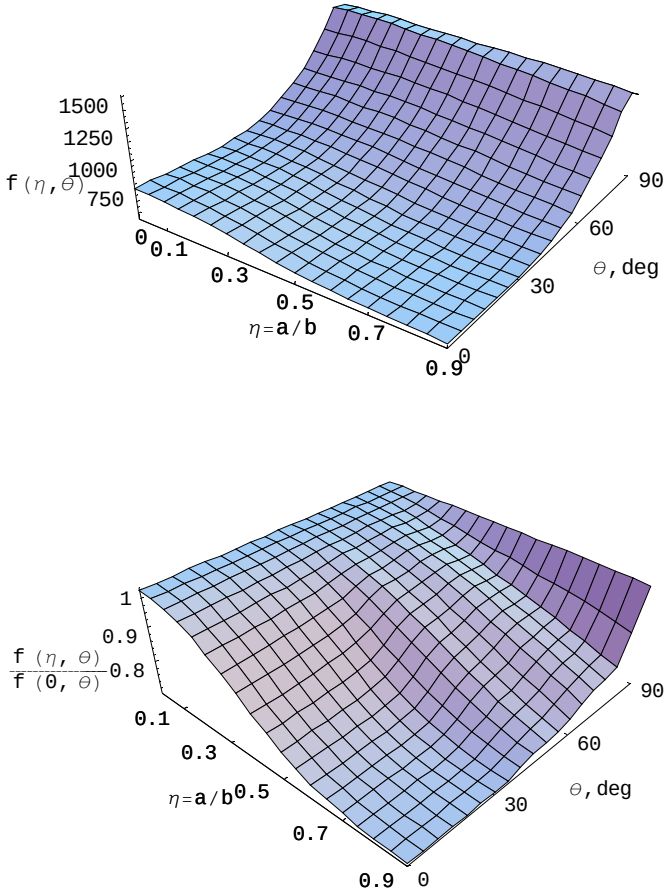

(a) The fourth natural frequency, rad/s

(b) Normalized at $\eta = 0$ for each fiber angle

Figure 3.11 Variation of the fourth natural frequency as a function of the crack ratio (a/b) and fiber angle (θ).

When the fiber angle is around 60°, where the bending and torsion are highly coupled, the frequency reduction with the crack ratio increased has a different pattern as that when the fiber angle is smaller. For instance, Figure 3.9 and Figure 3.10 indicate an accelerated reduction of the second and third frequencies with respect to the crack ratio in the region of θ = 60°. At a certain crack ratio, the natural frequency is controlled by either the bending or torsional mode when the fiber angle is small (the coupling is weak). However, when the fiber angle is increased such that the coupling becomes stronger, the same natural frequency which is previously controlled by the bending mode (or the torsional mode) becomes controlled by the torsional mode (or the bending mode). This could be the main reason for the transient region of the frequency reduction.

B) Natural frequency change as a function of crack location and fiber angle

Assume that the crack ratio is fixed at $\eta = 0.3$ and the fiber volume fraction is $V = 0.5$. The natural frequency will be affected by the crack location and fiber angle. The first four natural frequencies are plotted in Figure 3.12 to Figure 3.15 as follows.

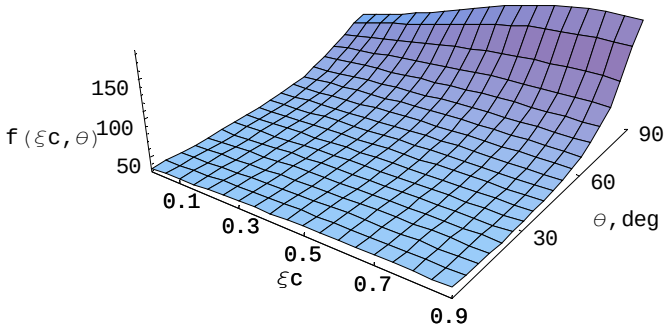

(a) The first natural frequency, rad/s

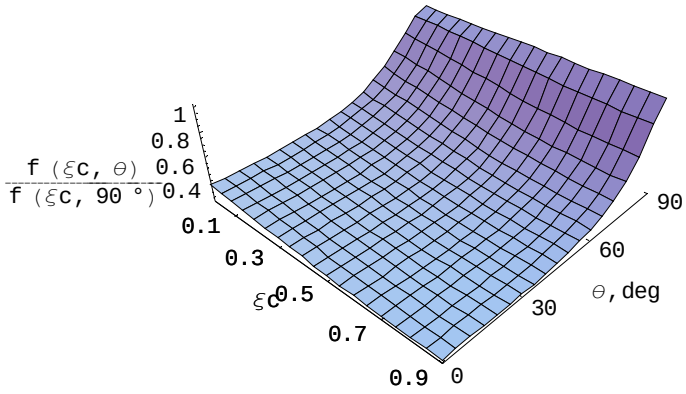

(b) Normalized at $\theta = 90°$ for each crack location

Figure 3.12 Variation of the first natural frequency as a function of the normalized crack location (ξ_c) and fiber angle (θ).

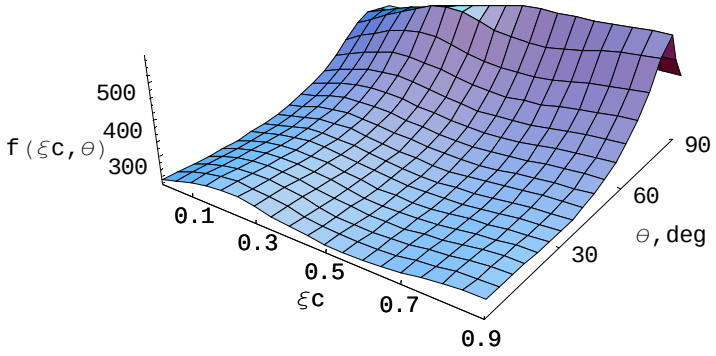

(a) The second natural frequency, rad/s

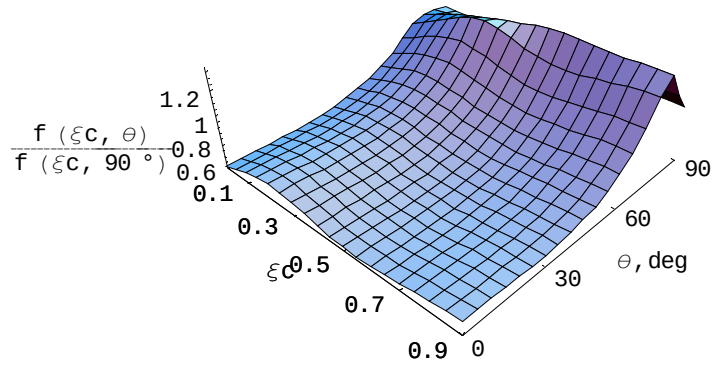

(b) Normalized at $\theta = 90°$ for each crack location

Figure 3.13 Variation of the second natural frequency as a function of the normalized crack location (ξ_c) and fiber angle (θ).

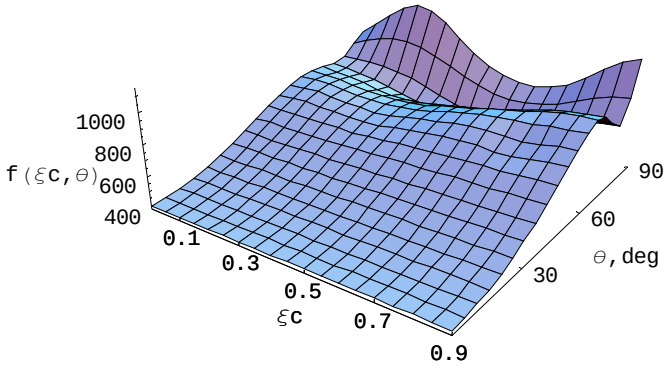

(a) The third natural frequency, rad/s

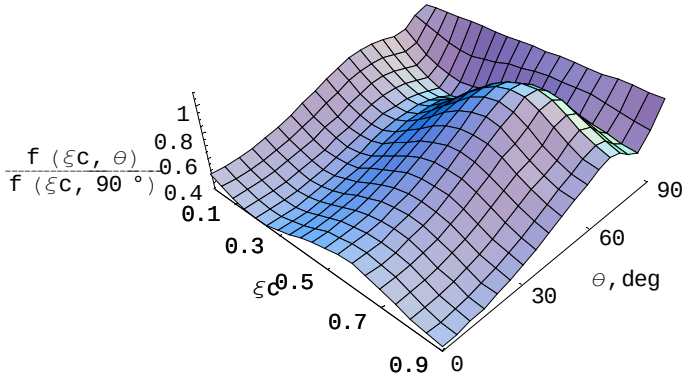

(b) Normalized at $\theta = 90°$ for each crack location

Figure 3.14 Variation of the third natural frequency as a function of the normalized crack location (ξ_c) and fiber angle (θ).

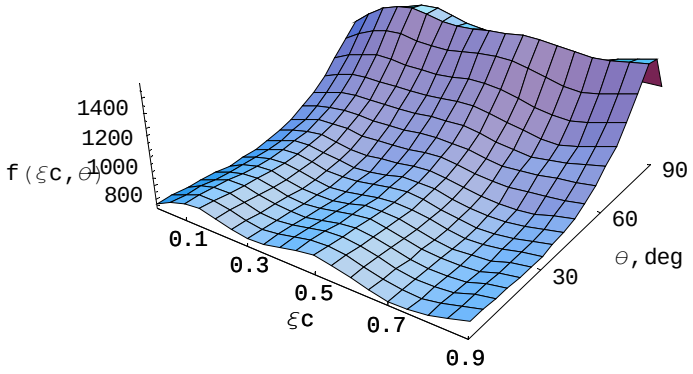

(a) The fourth natural frequency, rad/s

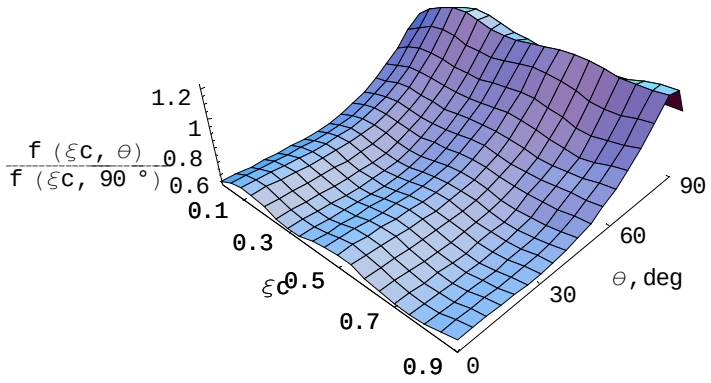

(b) Normalized at $\theta = 90°$ for each crack location

Figure 3.15 Variation of the fourth natural frequency as a function of the normalized crack location (ξ_c) and fiber angle (θ).

Similar to the results in section A) where the crack ratio and fiber angle are taken as variables, the frequency change when bending and torsion are highly coupled has a pattern different from that when the coupling is "weak" at smaller fiber angles. When the fiber angle is fixed, the frequency change for different crack locations is affected by the corresponding mode shape.

C) In the case of high bending-torsion coupling

Assume that θ = 70° and V = 0.5. Bending and torsion are highly coupled with Ψ = 0.846. The natural frequency changes are plotted in Figure 3.16.

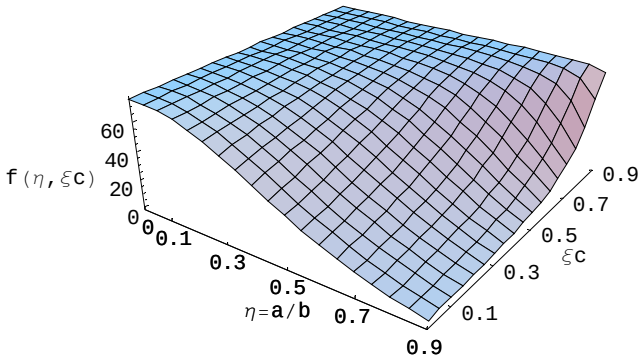

(a) The first natural frequency, rad/s (f_{intact} = 75.2 rad/s)

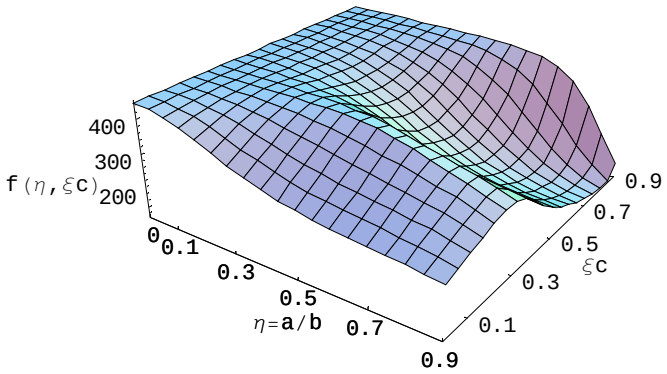

(b) The second natural frequency, rad/s (f_{intact} = 445.6 rad/s)

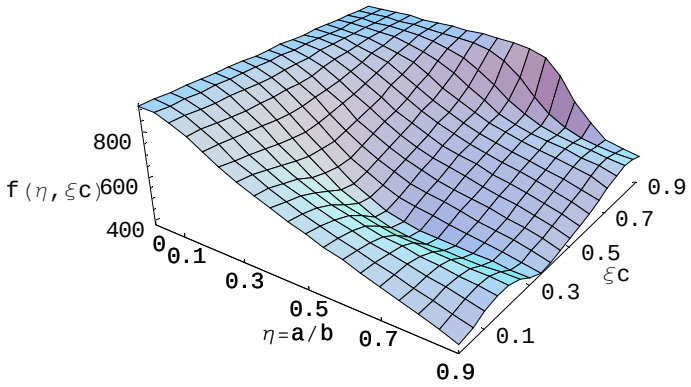

(c) The third natural frequency, rad/s (f_{intact} = 916.1 rad/s)

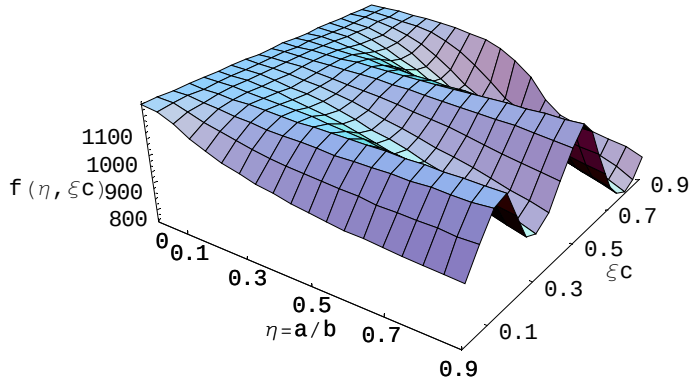

(c) The fourth natural frequency, rad/s (f_{intact} = 1179.7 rad/s)

Figure 3.16 Variation of natural frequencies as a function of the crack ratio (a/b) and the normalized crack location, ξ_c, for highly coupled situation due to material properties.

In general the natural frequencies experience further reduction with the crack ratio increased. Figure 3.16 indicates clearly that for high crack ratio, the frequencies have a different variation in terms of the crack location. As noticed in Krawczuk and Ostachowicz (1995) and Song *et al*. (2003) where only bending vibration is investigated, the higher frequency reduction may be expected for the crack located around the largest curvature of the mode related to that frequency. While the trend is still shown in Figure 3.16, the largest frequency reduction no longer coincides with either the largest bending curvature or torsion curvature, since bending and torsional mode usually do not have the largest curvature or node at the same location.

D) In cases of low bending-torsion coupling and bending-torsion decoupled

When θ = 30° and V = 0.5, bending and torsion are weakly coupled with Ψ = 0.0545. The natural frequency changes are plotted in Figure 3.17.

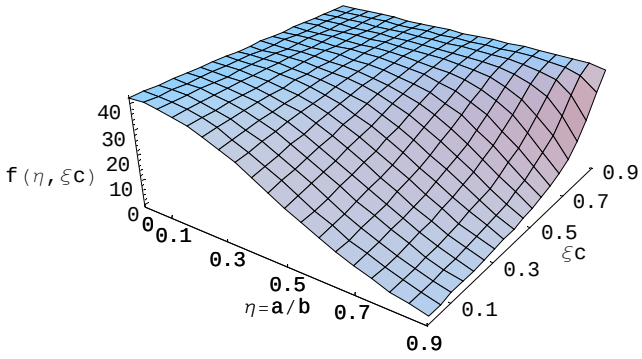

(a) The first natural frequency, rad/s (f_{intact} = 42.35 rad/s)

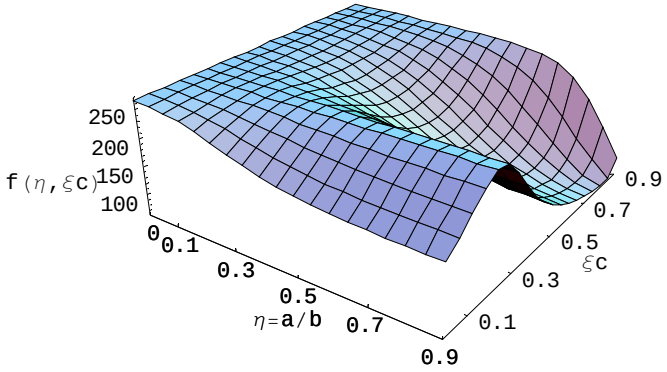

(b) The second natural frequency, rad/s (f_{intact} = 265.42 rad/s)

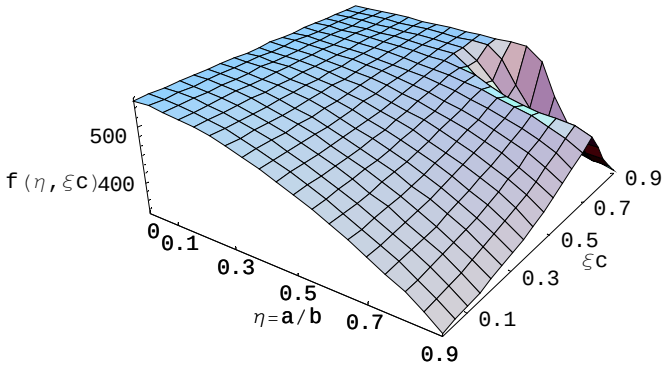

(c) The third natural frequency, rad/s (f_{intact} = 554.38 rad/s)

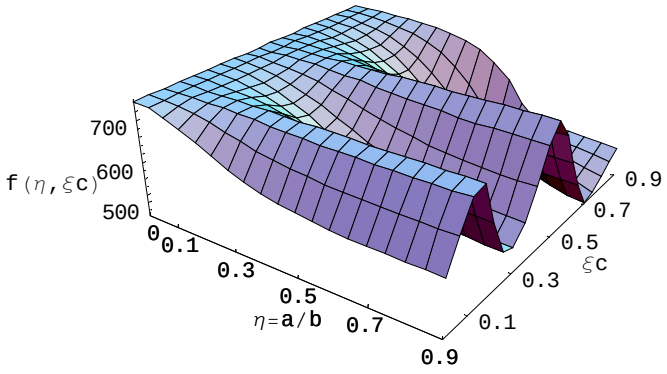

(c) The fourth natural frequency, rad/s (f_{intact} = 743.41 rad/s)

Figure 3.17 Variation of natural frequencies as a function of the crack ratio, a/b, and the normalized crack location, ξ_c, for weakly coupled situation.

It is obvious that the third natural frequency does not show a similar variation as that in Figure 3.16(c) of section C) where bending and torsion are highly coupled. When the coupling due to the material properties is weak, i.e. the coupling measure Ψ is very small, the frequency variation exhibits quite a similar feature as the case where bending and torsion are initially decoupled due to the material properties, and then coupled only due to the presence of the crack. The frequency variation for the latter case is shown in Figure 3.18.

When θ = 0° or 90°, the bending and torsion are decoupled if there are no cracks. The natural frequencies for bending and torsion are listed in Table 3.1 as follows.

Table 3.1 The first five natural frequencies for θ = 0° and 90°, rad/s

rad/s	θ = 0°					θ = 90°				
	1st	2nd	3rd	4th	5th	1st	2nd	3rd	4th	5th
Bending	43.6	273.1	764.7	1498.5	2477.2	181.0	1134.5	3176.7	6225.0	10290.4
Torsion	413.5	1240.6	2067.7	2894.7	3721.8	same as θ = 0°				

However, the presence of an edge crack introduces coupling through the additional boundary condition at the crack location. For θ = 0° and V = 0.5, the natural frequency changes are plotted in Figure 3.18 as a function of the crack ratio and location.

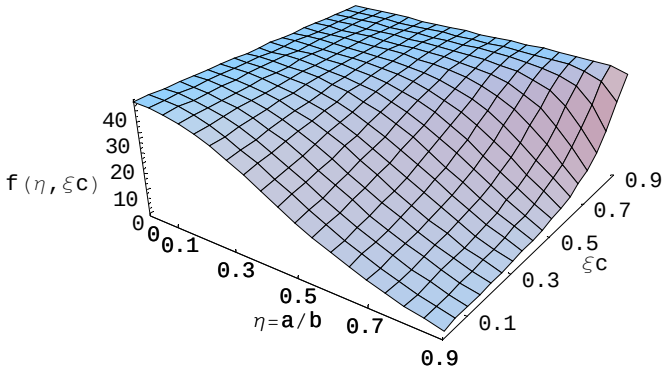

(a) The first natural frequency, rad/s

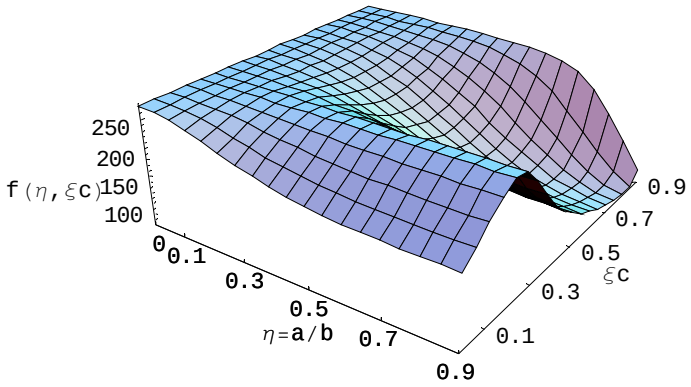

(b) The second natural frequency, rad/s

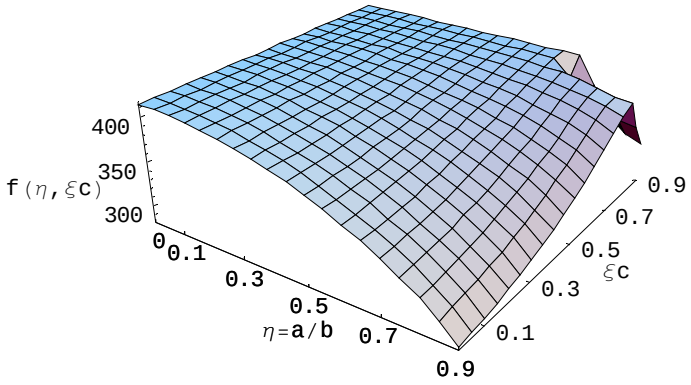

(c) The third natural frequency, rad/s

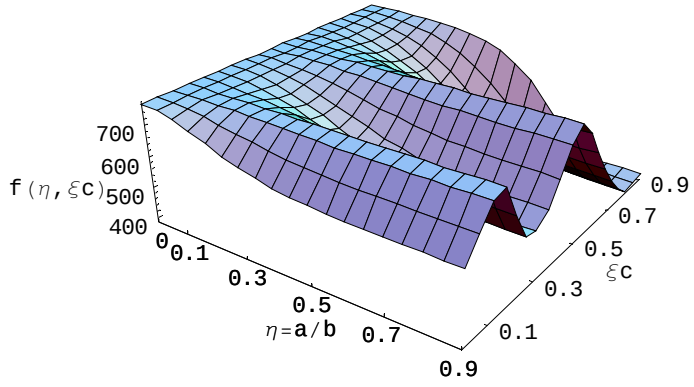

(d) The fourth natural frequency, rad/s

Figure 3.18 Variation of natural frequencies as a function of the crack ratio, a/b, and the normalized crack location, ξ_c, for situation that the coupling is introduced by the crack only.

When the coupling of bending and torsion is introduced by the crack only (no coupling if there was no cracks), the third natural frequency has very similar variation as that of the first natural frequency. The coupled natural frequency is predominantly controlled by either the bending mode or the torsional mode, while the surface crack introduces only a "weak" coupling between bending and torsion. The third coupled frequency is actually close to the first torsional frequency so that the variation is quite close to that of the first coupled frequency that is controlled by the first bending mode.

For the situation shown in Figure 3.17 where coupling due to material properties is "weak", the coupling seems predominantly controlled by the local flexibility due to the crack such that the frequency variation exhibits a similar trend as in Figure 3.18.

3.7 Mode Shape Changes

For theoretical analysis, the change of mode shapes may help to locate the crack as well as its magnitude, in conjunction with the change of natural frequencies. In the situation of highly coupled bending and torsion (θ = 70° and V = 0.5 as in Section 3.6) due to the material properties, the first three mode shapes are plotted in Figure 3.19-24 for different crack depths and locations.

A) For crack at location $\xi_c = 0.2$

In the following figures, each mode shape is obtained with the crack ratio at 0.2, 0.4 and 0.6, while the crack ratio of 0 indicates no cracks.

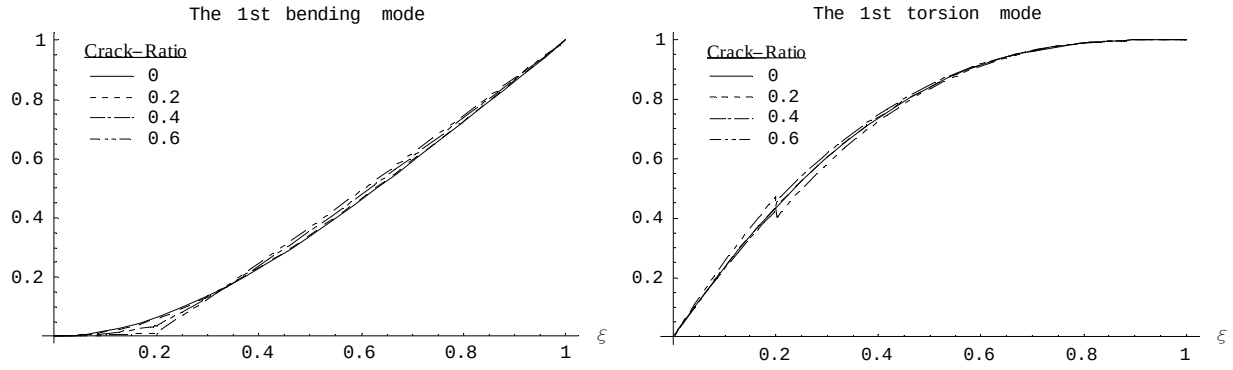

Figure 3.19 The first mode shapes for $\xi_c = 0.2$, $V = 0.5$ and $\theta = 70°$ as the crack ratio changes. Note that the discontinuity increases with the crack ratio at the crack location.

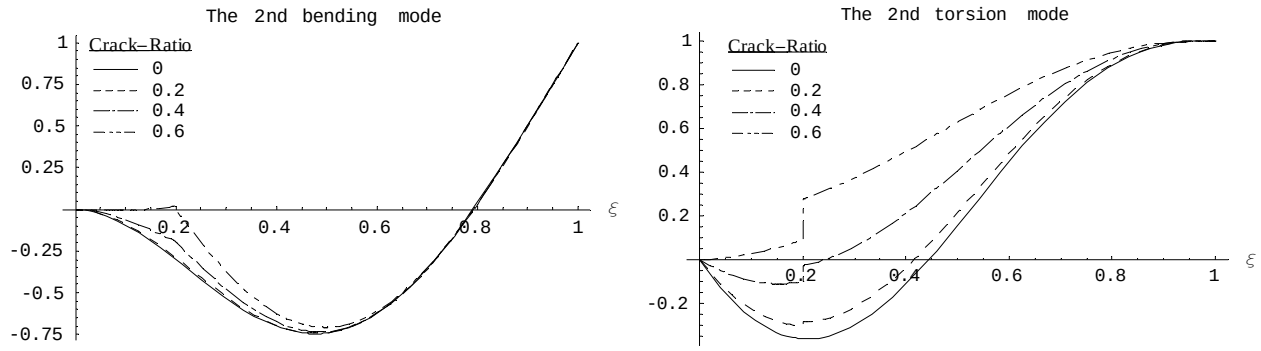

Figure 3.20 The second mode shapes for $\xi_c = 0.2$, $V = 0.5$ and $\theta = 70°$ as the crack ratio changes.

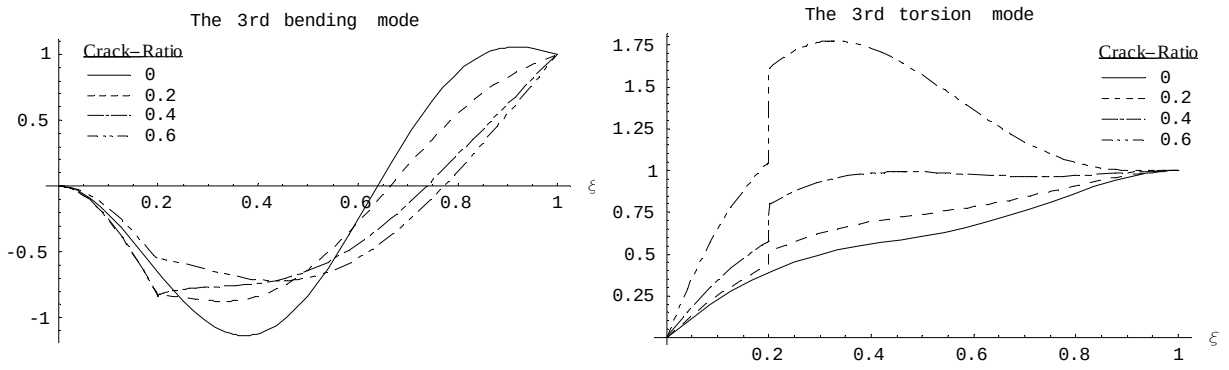

Figure 3.21 The third mode shapes for $\xi_c = 0.2$, $V = 0.5$ and $\theta = 70°$ as the crack ratio changes.

Each of the first three modes is normalized by the value at the free end of the cantilever. The higher mode seems more sensitive to the crack depth, even though the crack is not located at the large curvature position. The discontinuity of the torsional mode is more obvious than the bending mode. Since the characteristic equation consists of 12 simultaneous equations, any small deviation from the exact frequency solution changes the magnitude of the mode shape a lot (especially for the torsional modes). However, the shape and increasing distortion at the crack location may still be of value for detecting the crack location, particularly when both bending and torsional modes are taken into consideration.

B) For crack at location $\xi_c = 0.5$

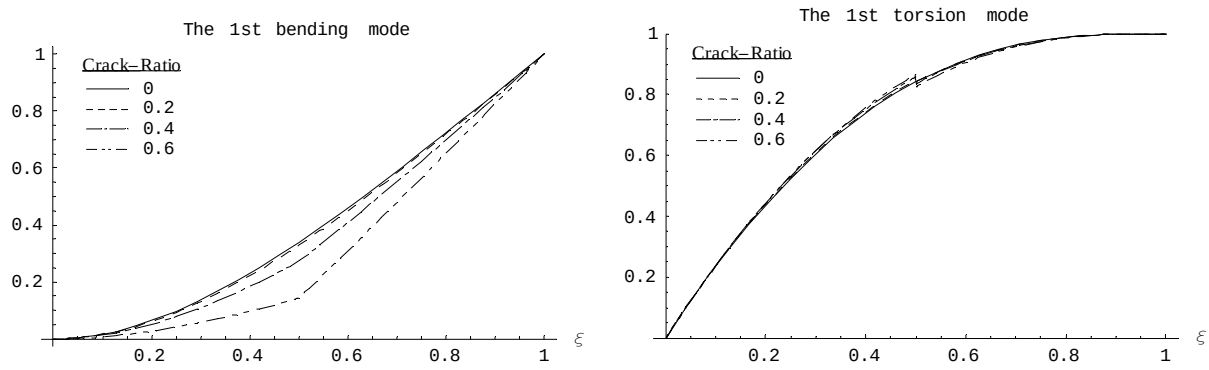

Figure 3.22 The first mode shapes for $\xi_c = 0.5$, V = 0.5 and $\theta = 70°$ as the crack ratio changes. Note that the discontinuity increases with the crack ratio at the crack location.

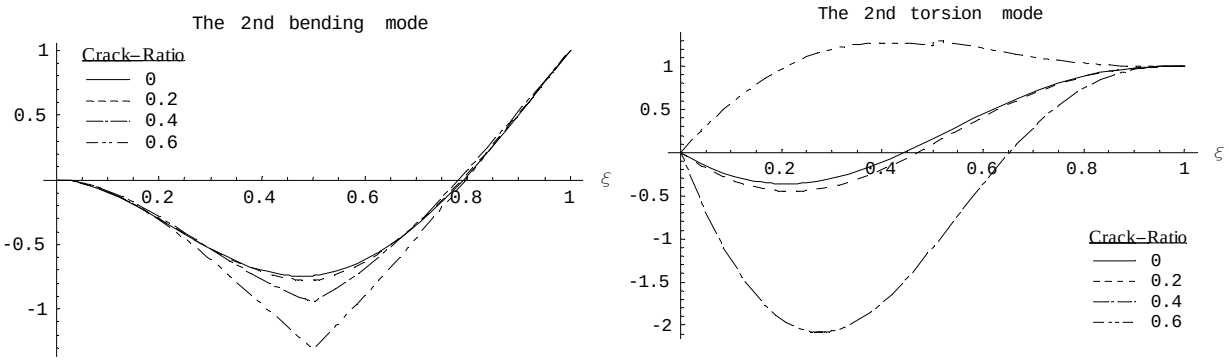

Figure 3.23 The second mode shapes for $\xi_c = 0.5$, V = 0.5
and $\theta = 70°$ as the crack ratio changes.

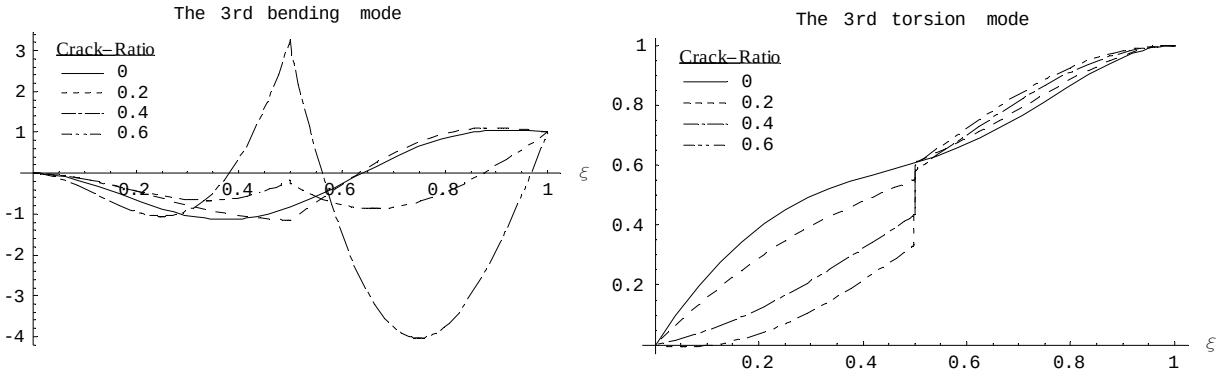

Figure 3.24 The third mode shapes for $\xi_c = 0.5$, V = 0.5
and $\theta = 70°$ as the crack ratio changes.

For the crack located at the mid-point of the cantilever, distortion of higher mode shapes is even more obvious. Compared with those where only the bending mode, either for the Euler-Bernoulli beam or for the Timoshenko beam, is studied, the change of mode shapes due to the crack for the composite beam with bending and torsion coupled is more significant. This change may be utilized to locate the crack as well as to quantify its magnitude.

3.8 Summary

A composite beam with an edge crack and of high aspect ratio vibrates in coupled bending and torsional modes, either due to the material properties, due to the crack or both. The beam consists of several fiber-reinforced plies with all fibers orientated in the same direction. The local flexibility approach based on linear fracture mechanics is taken to model the crack and a local compliance matrix at the crack location is derived. Changes in natural frequencies and mode shapes of a cantilevered beam are investigated. Some observations include:

1) The dimensionless coefficients of the compliance matrix exhibit double symmetry with respect to the fiber orientation and fiber volume fraction. The internal bending moment distribution due to the crack affects the bending mode most significantly through the local flexibility matrix; the effect is same for the torsional mode; the internal shear force distribution plays the least role in the local flexibility.
2) The decrease of natural frequencies for a cracked composite beam depends not only on the crack location and its depth, but also on the material properties, as shown in Krawczuk and Ostachowicz (1995) for an Euler-Bernoulli beam. However, for the composite cantilever with bending and torsional modes coupled, the largest frequency reduction no longer coincides with the case that crack is located at either the largest bending or torsion curvatures.
3) A “strong” coupling between the bending and torsion is observed for the fiber angle around ±60°, while the coupling is “weak” for the fiber angle between ±35°. The frequency variation with respect to either the crack ratio or its location usually experiences a transient state when the coupling is “strong”, such that the pattern is significantly different from the “weakly” coupled case. At this transient state the frequency variation previously controlled mainly by the bending mode (or the torsional mode) becomes controlled by the torsional mode (or the bending mode).
4) When the fiber angle is 0 or ±90°, bending and torsion are decoupled if there is no crack. The edge crack introduces coupling to the initially uncoupled bending and torsion. The decrease of natural frequencies exhibits a similar pattern as that when

the fiber angle is between ±35°; the pattern is predominantly controlled by either bending or torsional mode, but not both.

5) The coupled mode shapes are more sensitive to both the crack location and its depth. Higher modes exhibit more distortion at the crack location.

An analytical model of a fiber-reinforced composite beam with an edge crack has been developed. The spectrum of the natural frequency reduction, along with observations on the mode shape changes indicated by this model, may be used to detect both the crack location and its depth for on-line structural health monitoring. When the cracked beam vibrates with a specific loading spectrum, the model presented in this paper may help analyze the stress distribution around the crack tip such that a crack propagation model may be developed to investigate damage prognosis, and make predictions regarding the behavior of the structure to future loads. For instance these results may be useful for predicting flutter speed reduction in aircraft with composite wings due to fatigue cracking.

Contributions

The following lists contributions to the literature on cracked composite beams:

1) An analytical model of cracked composite beam vibrating in coupled bending and torsion is developed. The effects of the crack in conjunction of the material anisotropy to the modal parameters are investigated.
2) The local flexibility concept is extended in the cracked composite beam model. One new coefficient (tearing mode by torsional moment) in the local flexibility matrix is calculated from linear fracture mechanics and classical theory of elasticity. The final 3×3 flexibility matrix is obtained including the bending-torsion coupling term in the off-diagonal position.
3) The model developed here is new, and no analytical model of cracked composite beams vibrating in coupled bending-torsion exists in the literature prior to this research.

Chapter 4

Crack Induced Changes in Aeroelastic Stabilities of a Composite Wing

4.1 Introduction

The one-dimensional beam model presented in Chapter 3 is selected as the basic elastic model of an aircraft composite wing in this chapter. The wing is assumed to be unswept with a large aspect ratio and uniform cross-section. The elastic coupling between bending and torsion modes is introduced by the unbalanced laminates as shown in Chapter 3. In addition, the offset of the center of gravity from the reference axis introduces an inertial coupling between the two modes as recognized in most wing structures. The final equation of motion will then include the coupling of both types. Other elastic interactions such as extension-bending coupling, warping of cross section, rotary inertia and shear deformation are relatively less significant and therefore neglected here again. It is assumed that the elastic axis of the composite wing coincides with the reference axis of the beam model. The edge crack introduces additional boundary conditions at the crack location. The local flexibility matrix has the same components as determined in Chapter 3. Steady and quasi-steady aerodynamic forces are assumed in calculating flutter and divergence speeds, considering the fact that many UAVs with slender composite wings fly at relatively low speed. Unidirectional fiber orientation is used again to better understand the effect of material properties in conjunction with the edge crack. The fundamental mode shapes of both the intact and cracked beam are used in Galerkin's method to provide an approximate solution

for flutter and divergence speeds. Free vibration of the cracked composite wing is analyzed. Changes in the flutter/divergence speed with respect to the crack ratio, its location and the fiber orientation are presented.

4.2 Free Vibration of an Unswept Composite Wing with an Edge Crack

The unswept composite wing modeled by a cantilever beam with uniform cross section is shown in Figure 4.1 where a transverse edge crack has a uniform depth and a crack plane parallel to the *x*-*z* plane. The elastic axis of the wing coincides with the reference axis of the beam model (the *y*-axis). The 1-2 axes are the material's principle axes in each ply and at an angle of θ with respect to the *x*-*y* axes. The fiber angle in each ply as well as the ply sequence does not affect the formulation of the beam model. However, without losing generality it is assumed that the fiber in each ply is orientated in the same direction, in order to investigate the effect of material properties on the flutter/divergence speed in the presence of the edge crack.

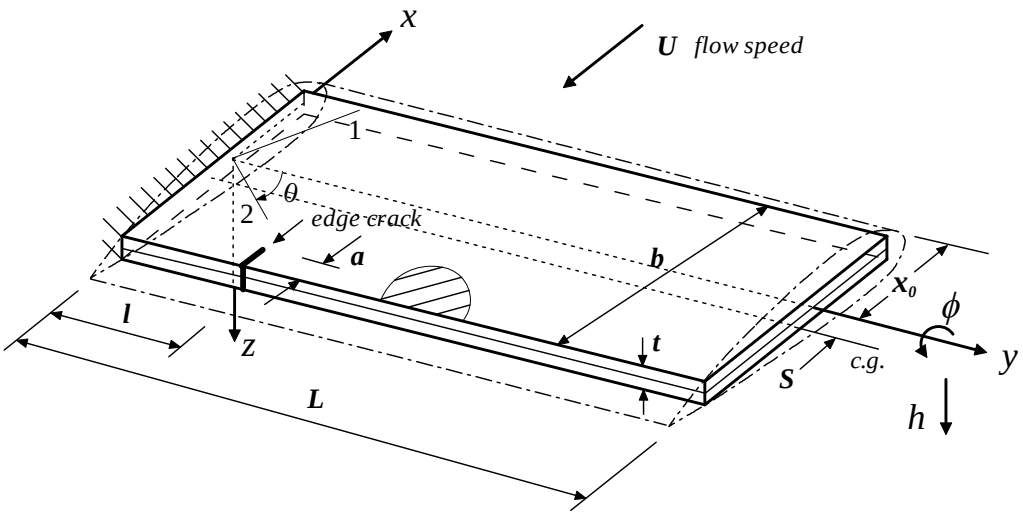

Figure 4.1 A cantilever beam model for an unswept composite wing with an edge crack. (*L* – beam length; *b* – beam width; *t* – beam height; *l* – crack location; *a* – crack width; x_0 – elastic axis location; *S* – offset of the center of gravity; *U* – flow speed; ϕ - rotation of beam around the reference axis; *h* – transverse displacement of the reference axis.)

The bending stiffness parameter *EI*, the torsional stiffness parameter *GJ* and the bending-torsion coupling parameter *K* are formulated the same way as in Chapter 3. Once the stiffnesses *EI*, *K* and *GJ* are obtained, free vibration of the composite wing model with damping neglected becomes

$$\begin{aligned} EI\frac{\partial^4 h}{\partial y^4} - K\frac{\partial^3 \phi}{\partial y^3} + m\frac{\partial^2 h}{\partial t^2} + S_y\frac{\partial^2 \phi}{\partial t^2} = 0 \\ GJ\frac{\partial^2 \phi}{\partial y^2} - K\frac{\partial^3 h}{\partial y^3} - I_y\frac{\partial^2 \phi}{\partial t^2} - S_y\frac{\partial^2 h}{\partial t^2} = 0 \end{aligned} \tag{4.1}$$

where m is the mass per unit length, I_y the polar mass moment of inertia per unit length about the y-axis ($I_y = I_{c.g.} + mS^2$ with $I_{c.g.}$ the polar mass moment of inertia per unit length about the center of gravity), and $S_y = mS$. Note equation (4.1) now includes the additional inertia coupling term containing S_y, compared to the composite beam equation (3.19) in Chapter 3.

Based on separation of variables $h(y,t) = H(y)e^{i\omega t}$, $\phi(y,t) = \Phi(y)e^{i\omega t}$, equation (4.1) is transferred to the eigenproblem

$$\begin{aligned} EIH^{iv} - K\Phi''' - \omega^2(mH + S_y\Phi) = 0 \\ GJ\Phi'' - KH''' + \omega^2(I_y\Phi + S_yH) = 0 \end{aligned} \tag{4.2}$$

where the primes or Roman numeral indicate differentiation with respect to y, and are used throughout this chapter. Let $\xi = y/L$ and $D = d(\cdot)/d\xi$, then eliminating either H or Φ in equation (4.2) yields the auxiliary equation

$$(D^6 + aD^4 - bD^2 - abc)W = 0 \tag{4.3}$$

where $W = \Phi$ or H and

$$a = \frac{I_y EIL^2\omega^2}{EI \cdot GJ - K^2}$$

$$b = \frac{mGJL^4\omega^2}{EI \cdot GJ - K^2}$$

$$c = (1 - \frac{S_y^2}{I_y m})(1 - \frac{K^2}{EI \cdot GJ})$$

Since $I_y = I_{c.g.} + mS^2 > 0$ and $0 < K^2/(EI \cdot GJ) < 1$, it is obvious that $0 < c < 1$. The closed form solution given in Appendix B is still valid for equation (4.2). Expressions of *a*, *b* and *c* are now different as the counterparts for the composite beam equation (3.21) in Chapter 3.

The general solution of equation (4.2) becomes

$$\begin{aligned} H(\xi) &= A_1 \cosh\alpha\xi + A_2 \sinh\alpha\xi + A_3 \cos\beta\xi + A_4 \sin\beta\xi + A_5 \cos\gamma\xi + A_6 \sin\gamma\xi \\ \Phi(\xi) &= B_1 \cosh\alpha\xi + B_2 \sinh\alpha\xi + B_3 \cos\beta\xi + B_4 \sin\beta\xi + B_5 \cos\gamma\xi + B_6 \sin\gamma\xi \end{aligned} \tag{4.4}$$

where

$$\alpha = [2(q/3)^{1/2} \cos(\varphi/3) - a/3]^{1/2}$$

$$\beta = [2(q/3)^{1/2} \cos((\pi - \varphi)/3) + a/3]^{1/2}$$

$$\gamma = [2(q/3)^{1/2} \cos((\pi + \varphi)/3) + a/3]^{1/2}$$

with

$$q = b + a^2/3$$

$$\varphi = \cos^{-1}[(27abc - 9ab - 2a^3)/(2(a^2 + 3b)^{3/2}]$$

and *a*, *b* and *c* are given in equation (4.3).

Similarly, coefficients $A_{1\text{-}6}$ and $B_{1\text{-}6}$ are related, but the relations no longer bear the same formulae as in Chapter 3 for the case of no inertia coupling. After an algebraic manipulation, the relationships are determined to be:

$$\begin{aligned} B_1 &= (k_\alpha A_2 - m_\alpha A_1)/L, \; B_2 = (k_\alpha A_1 - m_\alpha A_2)/L \\ B_3 &= (m_\beta A_3 + k_\beta A_4)/L, \; B_4 = (m_\beta A_4 - k_\beta A_3)/L \\ B_5 &= (m_\gamma A_5 + k_\gamma A_6)/L, \; B_6 = (m_\gamma A_6 - k_\gamma A_5)/L \end{aligned} \tag{4.5}$$

where

$$m_\alpha = -L^3 S_y \omega^2 t_\alpha, \; k_\alpha = K\alpha^3 t_\alpha$$

$$m_\beta = L^3 S_y \omega^2 t_\beta, \; k_b = K\beta^3 t_\beta$$

$$m_\gamma = L^3 S_y \omega^2 t_\gamma, \; k_\gamma = K\gamma^3 t_\gamma$$

with

$$t_\alpha = \frac{EI\alpha^4 - L^4 m\omega^2}{K^2\alpha^6 - L^6 S_y^2 \omega^4},\ t_\beta = \frac{EI\beta^4 - L^4 m\omega^2}{K^2\beta^6 + L^6 S_y^2 \omega^4},\ t_\gamma = \frac{EI\gamma^4 - L^4 m\omega^2}{K^2\gamma^6 + L^6 S_y^2 \omega^4}$$

In particular, rather than the one-to-one relation in equation (3.21), two coefficients in $A_{1\text{-}6}$ and now coupled with two coefficients in $B_{1\text{-}6}$.

Substituting equation (4.5) to (4.4) yields the dimensionless expression for the twisting angle $\Phi(\xi)$:

$$\begin{aligned}\Phi(\xi) = [&(k_\alpha \sinh\alpha\xi - m_\alpha \cosh\alpha\xi)A_1 + (k_\alpha \cosh\alpha\xi - m_\alpha \sinh\alpha\xi)A_2 \\ &+ (m_\beta \cos\beta\xi - k_\beta \sin\beta\xi)A_3 + (m_\beta \sin\beta\xi - k_\beta \cos\beta\xi)A_4 \\ &+ (m_\gamma \cos\gamma\xi - k_\gamma \sin\gamma\xi)A_5 + (m_\gamma \sin\gamma\xi - k_\gamma \cos\gamma\xi)A_6]/L\end{aligned} \tag{4.6}$$

At any cross section, the cross-sectional rotation $\Theta(\xi)$, the bending moment $M(\xi)$, the shear force $S(\xi)$ and the torsional moment $T(\xi)$ with the normalized coordinate ξ become:

$$\begin{aligned}\Theta(\xi) = \frac{1}{L}\frac{dH(\xi)}{d\xi} = \frac{1}{L}[&A_1\alpha\sinh\alpha\xi + A_2\alpha\cosh\alpha\xi - A_3\beta\sin\beta\xi \\ &+ A_4\beta\cos\beta\xi - A_5\gamma\sin\gamma\xi + A_6\gamma\cos\gamma\xi]\end{aligned} \tag{4.7}$$

$$\begin{aligned}M(\xi) &= \frac{EI}{L^2}\frac{d^2H(\xi)}{d\xi^2} - \frac{K}{L}\frac{d\Phi(\xi)}{d\xi} \\ &= \frac{EI}{L^2}[(r_\alpha \sinh\alpha\xi - n_\alpha \cosh\alpha\xi)A_1 + (r_\alpha \cosh\alpha\xi - n_\alpha \sinh\alpha\xi)A_2 \\ &\quad + (n_\beta \cos\beta\xi + r_\beta \sin\beta\xi)A_3 + (n_\beta \sin\beta\xi - r_\beta \cos\beta\xi)A_4 \\ &\quad + (n_\gamma \cos\gamma\xi + r_\gamma \sin\gamma\xi)A_5 + (n_\gamma \sin\gamma\xi - r_\gamma \cos\gamma\xi)A_6]\end{aligned} \tag{4.8}$$

$$\begin{aligned}S(\xi) &= -\frac{1}{L}\frac{dM(\xi)}{d\xi} \\ &= \frac{EI}{L^3}[\alpha(n_\alpha \sinh\alpha\xi - r_\alpha \cosh\alpha\xi)A_1 + \alpha(n_\alpha \cosh\alpha\xi - r_\alpha \sinh\alpha\xi)A_2 \\ &\quad + \beta(n_\beta \sin\beta\xi - r_\beta \cos\beta\xi)A_3 - \beta(n_\beta \cos\beta\xi + r_\beta \sin\beta\xi)A_4 \\ &\quad + \gamma(n_\gamma \sin\gamma\xi - r_\gamma \cos\gamma\xi)A_5 - \gamma(n_\gamma \cos\gamma\xi + r_\gamma \sin\gamma\xi)A_6]\end{aligned} \tag{4.9}$$

$$\begin{aligned}T(\xi) &= -\frac{K}{L^2}\frac{d^2H(\xi)}{d\xi^2} + \frac{GJ}{L^2}\frac{d\Phi(\xi)}{d\xi} \\ &= \frac{GJ}{L^2}[-(p_\alpha \cosh\alpha\xi + g_a \sinh\alpha\xi)A_1 - (p_\alpha \sinh\alpha\xi + g_a \cosh\alpha\xi)A_2 \\ &\quad + (p_\beta \cos\beta\xi - g_\beta \sin\beta\xi)A_3 + (p_\beta \sin\beta\xi + g_\beta \cos\beta\xi)A_4 \\ &\quad + (p_\gamma \cos\gamma\xi - g_\gamma \sin\gamma\xi)A_5 + (p_\gamma \sin\gamma\xi + g_\gamma \cos\gamma\xi)A_6]\end{aligned} \tag{4.10}$$

where

$$n_R = R(Kk_R - R \cdot EI)/EI\ ,\ r_R = RKm_R/EI$$

$$p_R = R(RK - GJk_R)/GJ\ ,\ g_R = Rm_R\ ,\ R = \alpha, \beta, \gamma.$$

Expressions for $\Theta(\xi)$, $M(\xi)$, $S(\xi)$ and $T(\xi)$ become more sophisticated as apposed to the counterparts in equation (3.22) in Chapter 3.

The local flexibility matrix [C] is the same as expressed in equation (3.15) with components given in equation (3.14). Let the edge crack be located at $\xi_c = l/L$, as shown in Figure 4.1. The beam can be replaced with two intact beams connected at the crack location. let $\Gamma = [\cosh\alpha\xi\ \ \sinh\alpha\xi\ \ \cos\beta\xi\ \ \sin\beta\xi\ \ \cos\gamma\xi\ \ \sin\gamma\xi]^T$, then

$0 \le \xi \le \xi_c$,

$$\begin{aligned} H_1(\xi) &= [A_1\ A_2\ A_3\ A_4\ A_5\ A_6]\Gamma, \\ \Phi_1(\xi) &= [B_1\ B_2\ B_3\ B_4\ B_5\ B_6]\Gamma; \end{aligned} \tag{4.11.1}$$

$\xi_c \le \xi \le 1$,

$$\begin{aligned} H_2(\xi) &= [A_7\ A_8\ A_9\ A_{10}\ A_{11}\ A_{12}]\Gamma, \\ \Phi_2(\xi) &= [B_7\ B_8\ B_9\ B_{10}\ B_{11}\ B_{12}]\Gamma. \end{aligned} \tag{4.11.2}$$

There are 12 unknowns in equation (4.11) since $B_{1\text{-}12}$ are related to $A_{1\text{-}12}$ by the relationship in equation (4.5). Again, at the crack location, $\xi = \xi_c$, the local flexibility concept demands

$$\begin{aligned} M_1(\xi_c) &= M_2(\xi_c) \\ S_1(\xi_c) &= S_2(\xi_c) \\ T_1(\xi_c) &= T_2(\xi_c) \\ H_2(\xi_c) &= H_1(\xi_c) + c_{22}S_1(\xi_c) + c_{26}T_1(\xi_c) \\ \Theta_2(\xi_c) &= \Theta_1(\xi_c) + c_{44}M_1(\xi_c) \\ \Phi_2(\xi_c) &= \Phi_1(\xi_c) + c_{62}S_1(\xi_c) + c_{66}T_1(\xi_c) \end{aligned} \tag{4.12.1-6}$$

For a cantilever wing, the fixed-free boundary conditions require that

at the fixed end, $\xi = 0$,

$$H_1(0) = \Theta_1(0) = \Phi_1(0) = 0\ ; \tag{4.13.1-3}$$

at the free end, $\xi = 1$,

$$M_2(1) = S_2(1) = T_2(1) = 0\,. \tag{4.13.4-6}$$

Substitution of equation (4.11) into (4.12) and (4.13) will yield the characteristic equation:

$$[\Lambda]A = 0 \tag{4.14}$$

where $A = [A_1\ A_2\ A_3\ A_4\ A_5\ A_6\ A_7\ A_8\ A_9\ A_{10}\ A_{11}\ A_{12}\ ]^T$ and $[\Lambda]$ the 12×12 characteristic matrix being a function of frequency. Natural frequencies can be obtained by solving equations $\det[\Lambda] = 0$. Substituting each natural frequency back into equation (4.14) yields the corresponding mode shape. Here the bending-torsion coupling is permanently present due to the inertial coupling, even though the elastic coupling vanishes when fiber angle θ = 0° or 90° as seen in Chapter 3.

4.3 Aeroelastic Stabilities of the Cracked Composite Wing

A) Location of the elastic axis

One of the important structural properties in aeroelastic analysis of an aircraft wing is the location of the elastic axis. The elastic axis of a beam is usually defined as the locus of shear centers of the cross sections along the wing span (Fung, 1969), while the shear center is defined as a point through which a shear force produces only bending and no torsional deflection at *any* cross section of the beam. However, except in some special cases such as when the composite laminate has a symmetric stacking, it is nearly impossible to find such an elastic axis of a composite beam in a closed form for arbitrary lay-ups. The beam model without the inertia coupling as presented in Chapter 3 is taken here as a simple example to illustrate this issue.

By equation (3.16), the bending curvature and twisting rate of the beam's mid-surface, defined as one-dimensional variables along the reference axis, can be written as

$$\begin{Bmatrix} h'' \\ \phi' \end{Bmatrix} = \frac{1}{EI \cdot GJ - K^2} \begin{bmatrix} GJ & K \\ K & EI \end{bmatrix} \begin{Bmatrix} M \\ T \end{Bmatrix} = \begin{bmatrix} a_{11} & a_{12} \\ a_{12} & a_{22} \end{bmatrix} \begin{Bmatrix} M \\ T \end{Bmatrix} \tag{4.15}$$

where $a_{11} = \dfrac{GJ}{EI \cdot GJ - K^2}, a_{12} = \dfrac{K}{EI \cdot GJ - K^2}, a_{22} = \dfrac{EI}{EI \cdot GJ - K^2}$.

Assume that a shear force, P, in the negative z-axis, is applied at the point $M(x_0, y_0)$, such that only bending and no twisting result on the cross section perpendicular to y-axis and containing Point M. Then at any other cross section between the fixed end and the point M, one has the internal bending and torsional moments as $M = -P(y_0 - y)$ and $T = Px_0$, respectively. Substituting these back into equation (4.15) and solving for ϕ by imposing the boundary condition $\phi(0) = 0$ yields

$$\phi(y) = \frac{1}{2} a_{12} P y^2 + (x_0 a_{22} - y_0 a_{12}) P y \tag{4.16}$$

The assumption requires that $\phi(y_0) = \frac{1}{2} a_{12} P y_0^2 + (x_0 a_{22} - y_0 a_{12}) P y_0 = 0$, which implies that

$$x_0 = \frac{1}{2} \frac{a_{12}}{a_{22}} y_0 = \frac{K}{2EI} y_0 \tag{4.17}$$

However, condition (4.17) only ensures that the cross section (containing point M) on which the shear force P is applied has only bending and no twisting deflection. Substituting equation (4.17) back to (4.16) gives the twist angle of any other cross section between the fixed end and up to $y = y_0$ as:

$$\phi(y) = \frac{1}{2} a_{12} P (y^2 - y_0 y) = \frac{KP}{2(EI \cdot GJ - K^2)} (y^2 - y_0 y) \tag{4.18}$$

It is obvious that on any cross section for $0 < y < y_0$ there is always twisting, and the angle depends not only on the material properties, but also on the magnitude of the shear force P. Therefore, the straight line defined by equation (4.17) is *not* the elastic axis defined earlier in this section, but the flexural line as defined in Fung (1969).

The inertia axis, elastic axis, aerodynamic center and airfoil are fundamental factors to determine aerodynamic forces (steady, quasi-steady or unsteady). Before the lifting force L and pitching moment M can be selected, some assumptions should be made. The beam model is used only as the load-carrying structure; the real wing must have upper and lower skins such that specific airfoil profile is obtained to meet aerodynamic requirements. The actual elastic axis of the wing, if it exists, may never coincide with the one of the beam model (also if it exists). In other words, the assumption on the elastic axis may be independent on the beam model; it may result from actual aerodynamic requirements on the airfoil profile and

the wing structure in detail. In short, the elastic axis, as well as the inertia axis, is used only to provide the external forces to the beam model, and could have nothing to do with the actual elastic axis of the beam model. In the following analysis, it is assumed that the elastic axis of the wing coincides with the reference axis of the beam model, and the inertia axis is parallel to the elastic axis at a constant distance *S* as shown in Figure 4.1.

B) Aeroelastic analysis by Galerkin's method

Since the flight speed is presumed to be low enough and little vortex could be produced due to the low angle of attack and small displacements, it is reasonable to consider that the flow is incompressible and irrotational. Furthermore, the large aspect ratio also justifies the use of two-dimensional strip theory, which means that the aerodynamic lift and moment at one chord section depends only on the angle of attack at that section, and is independent of the angle of attack at any other spanwise locations. Under these circumstances, the lifting force and pitching moment per unit span by a steady aerodynamic model can be expressed as (Dowell et al., 1978):

$$\begin{aligned} L &= \frac{\rho U^2}{2}\frac{\partial C_L}{\partial \phi} b\phi \\ M &= Lb\left(\frac{x_o}{b} - \frac{1}{4}\right) \end{aligned} \tag{4.19}$$

where L is the lifting force, positive upward, and M the pitching moment, positive nose up; C_L is the lifting coefficient with the theoretical value $dC_L/d\phi = 2\pi$; U is the speed of an incompressible air fluid; ρ is the air density; x_0 is the distance between the leading edge and the assumed elastic axis as shown in Figure 4.1. If the effective angle of attack contribution is also taken into account, the slightly more complex counterparts by a quasi-steady aerodynamic model may be expressed as (Fung, 1969):

$$\begin{aligned} L &= \frac{\rho U^2}{2}\frac{\partial C_L}{\partial \phi} b\left[\phi + \frac{1}{U}\frac{\partial h}{\partial t} + \frac{b}{U}\left(\frac{3}{4} - \frac{x_o}{b}\right)\frac{\partial \phi}{\partial t}\right] \\ M &= \frac{\rho U^2}{2}\frac{\partial C_L}{\partial \phi} b^2\left(\frac{x_o}{b} - \frac{1}{4}\right)\left[\phi + \frac{1}{U}\frac{\partial h}{\partial t} + \frac{b}{U}\left(\frac{3}{4} - \frac{x_o}{b}\right)\frac{\partial \phi}{\partial t}\right] - \frac{\rho U b^3 \pi}{16}\frac{\partial \phi}{\partial t} \end{aligned} \tag{4.20}$$

The equation of motion of the composite wing with aerodynamic forces applied becomes:

$$\begin{aligned} EI\frac{\partial^4 h}{\partial y^4} - K\frac{\partial^3 \phi}{\partial y^3} + m\frac{\partial^2 h}{\partial t^2} + S_y\frac{\partial^2 \phi}{\partial t^2} + L = 0 \\ GJ\frac{\partial^2 \alpha}{\partial y^2} - K\frac{\partial^3 h}{\partial y^3} - I_y\frac{\partial^2 \phi}{\partial t^2} - S_y\frac{\partial^2 h}{\partial t^2} + M = 0 \end{aligned} \tag{4.21}$$

Flutter/divergence speed by steady aerodynamic forces

Substituting equation (4.19) to (4.21) yields the governing equation with steady aerodynamic forces as:

$$\begin{aligned} EI\frac{\partial^4 h}{\partial y^4} - K\frac{\partial^3 \phi}{\partial y^3} + m\frac{\partial^2 h}{\partial t^2} + S_y\frac{\partial^2 \phi}{\partial t^2} + L_1 U^2\phi = 0 \\ GJ\frac{\partial^2 \alpha}{\partial y^2} - K\frac{\partial^3 h}{\partial y^3} - I_y\frac{\partial^2 \phi}{\partial t^2} - S_y\frac{\partial^2 h}{\partial t^2} + M_1 U^2\phi = 0 \end{aligned} \tag{4.22}$$

where

$$L_1 = \frac{\rho b}{2}\frac{\partial C_L}{\partial \phi},\ M_1 = \frac{\rho b^2}{2}\frac{\partial C_L}{\partial \phi}\left(\frac{x_o}{b} - \frac{1}{4}\right)$$

The linear homogeneous equations (4.22) may have a solution in the form:

$$h(y,t) = Af(y)e^{\lambda t},\ \phi(y,t) = Bg(y)e^{\lambda t} \tag{4.23}$$

where A, B and λ are complex constants in general.

Since the flutter modes are not known at the beginning, an approximate solution by Galerkin's method is usually obtained by assuming that the functions $f(y)$ and $g(y)$ are real and satisfy the boundary conditions so that they can be taken as the fundamental mode shapes of free vibration. Similarly it is natural for the cracked beam model to assume that $f(y)$ and $g(y)$ are the fundamental mode shapes satisfying boundary conditions not only at the ends but also at the crack location. The real functions $f(y)$ and $g(y)$ are now piecewise continuous with a discontinuity at the crack location. Since both $f(y)$ and $g(y)$ satisfy the boundary condition at the crack location, they are carrying most of the information related directly to the presence of the crack. Meanwhile since the aerodynamic forces are derived from two-dimensional strip theory, they are determined by the airfoil and angle of attack at

each cross section; the aerodynamic forces at one cross section do not affect the forces at other cross sections. In other words, the discontinuity of $f(y)$ and $g(y)$ does not affect the validation of the aerodynamic forces as given in equation (4.19) or (4.20). In the following analysis, functions $f(y)$ and $g(y)$ are taken as the fundamental bending and torsional mode shapes, respectively. They are obtained during the free vibration analysis presented in the last sub-section. Note that $f(y)$ and $g(y)$ are not decoupled bending and torsional mode shapes as widely used in the preliminary aeroelastic analysis of a wing structure, but coupled mode shapes at the first natural frequency. Using coupled modes as trial functions certainly provides more accurate solutions than the decoupled modes in aeroelastic analysis (Fung, 1969).

Substituting equation (4.23) to equation (4.22), and eliminating $e^{\lambda t}$ yields

$$A[EIf^{iv} + \lambda^2 mf] + B[-Kg''' + \lambda^2 S_y g + L_1 U^2 g] = 0 \tag{4.24.1}$$

$$A[-Kf''' - \lambda^2 S_y f] + B[GJg'' + \lambda^2 I_y g + M_1 U^2 g] = 0 \tag{4.24.2}$$

The coupled bending and torsional mode shapes for the cracked wing model can be expressed, respectively, as:

$$f(y) = \begin{cases} f_1(y) & 0 \le y \le l \\ f_2(y) & l < y \le L \end{cases}, \; g(y) = \begin{cases} g_1(y) & 0 \le y \le l \\ g_2(y) & l < y \le L \end{cases} \tag{4.25}$$

where l is the crack location with $f_1(y)$, $f_2(y)$, $g_1(y)$ and $g_2(y)$ all continuous within the individual domain. Multiplying equation (4.24.1) by $f(y)$ and equation (4.24.2) by $g(y)$, and integrating over [0, L] yields:

$$\begin{aligned} A[a_{11} + c_{11}\lambda^2] + B[a_{12} + b_{12}U^2 + c_{12}\lambda^2] = 0 \\ A[a_{21} + c_{21}\lambda^2] + B[a_{22} + b_{22}U^2 + c_{22}\lambda^2] = 0 \end{aligned} \tag{4.26}$$

where

$$a_{11} = EI\left(\int_0^l f_1^{iv} f_1 dy + \int_l^L f_2^{iv} f_2 dy\right), \; a_{12} = -K\left(\int_0^l g_1''' f_1 dy + \int_l^L g_2''' f_2 dy\right)$$

$$a_{21} = K\left(\int_0^l f_1''' g_1 dy + \int_l^L f_2''' g_2 dy\right), \; a_{22} = -GJ\left(\int_0^l g_1'' g_1 dy + \int_l^L g_2'' g_2 dy\right)$$

$$b_{12} = L_1\left(\int_0^l g_1 f_1 dy + \int_l^L g_2 f_2 dy\right), \; b_{22} = -M_1\left(\int_0^l g_1^2 dy + \int_l^L g_2^2 dy\right)$$

$$c_{11} = m(\int_0^l f_1^2 dy + \int_l^L f_2^2 dy),\ c_{12} = S_y(\int_0^l g_1 f_1 dy + \int_l^L g_2 f_2 dy)$$

$$c_{21} = c_{12},\ c_{22} = I_y(\int_0^l g_1^2 dy + \int_l^L g_2^2 dy)$$

A non-trivial solution of equation (4.26) requires that

$$\det\begin{bmatrix} a_{11} + c_{11}\lambda^2 & a_{12} + b_{12}U^2 + c_{12}\lambda^2 \\ a_{21} + c_{21}\lambda^2 & a_{22} + b_{22}U^2 + c_{22}\lambda^2 \end{bmatrix} = 0$$

or,

$$A_1\lambda^4 + (B_1 + C_1U^2)\lambda^2 + D_1 + F_1U^2 = 0 \tag{4.27}$$

where coefficients A_1, B_1, C_1, D_1 and F_1 are all constants and depend only on integrals given in equation (4.26):

$$A_1 = c_{11}c_{22} - c_{12}c_{21},\ B_1 = a_{11}c_{22} + a_{22}c_{11} - a_{21}c_{12} - a_{12}c_{21},\ C_1 = b_{22}c_{11} - b_{12}c_{21}$$

$$D_1 = a_{11}a_{22} - a_{12}a_{21}, F_1 = a_{11}b_{22} - a_{21}b_{12}$$

The characteristic equation (4.27) can be rewritten as

$$A_0\lambda^4 + C_0\lambda^2 + E_0 = 0 \tag{4.28}$$

where the coefficients depend on the constants given in equation (26) and the speed of air flow U as

$$A_0 = A_1,\ C_0 = B_1 + C_1U^2,\ \ E_0 = D_1 + F_1U^2.$$

For non-zero A_0, Equation (4.28) has a solution in the form:

$$\lambda^2 = \frac{-C_0 \pm \sqrt{C_0^2 - 4A_0E_0}}{2A_0} \tag{4.29}$$

Solving equation (4.28) for λ^2 would yields a pair of real or complex values, depending on the sign of $C_0^2 - 4A_0E_0$. Since the system has no damping as shown in the governing equation (4.22), a solution of $h(y, t)$ and $\phi(y, t)$ is stable only in the case that all values of λ^2 are purely real and negative. A positive real value of λ^2 yields a positive real root of λ in equation (4.28) while a complex value of λ^2 yields that at least one root of λ has a positive real part – both indicate an unstable motion. Meanwhile, it can be shown easily that $A_0 = A_1$ is a positive constant, not depending on air speed. Therefore, a stable solution requires that the following coefficients must be all positive simultaneously:

$$C_0 > 0,\ E_0 > 0,\ C_0^2 - 4A_0E_0 > 0 \tag{4.30}$$

When air speed U increases from zero, C_0, E_0 and $C_0^2 - 4A_0E_0$ must be all greater than zero for a stable motion. With the increasing of U, it is obvious that either E_0 or $C_0^2 - 4A_0E_0$ will become zero before C_0 does if the system becomes unstable. Hence, it is needed only to check the signs of E_0 and $C_0^2 - 4A_0E_0$. At the critical speed, $E_0 = 0$ or $C_0^2 - 4A_0E_0 = 0$.

1) If $E_0 = 0$, equation (4.28) has a root $\lambda = 0$, which results in the divergence speed as

$$U_{div}^2 = -\frac{D_1}{F_1} = \frac{a_{12}a_{21} - a_{11}a_{22}}{a_{11}b_{22} - a_{21}b_{12}} \tag{4.31}$$

2) If $C_0^2 - 4A_0E_0 = 0$, substitution of C_0, A_0 and E_0 in equation (4.28) yields

$$RU^4 + SU^2 + T = 0 \tag{4.32}$$

where

$$R = C_1^2,\ S = 2(B_1C_1 - 2A_1F_2),\ T = B_1^2 - 4A_1D_1.$$

The flutter speed can then be determined from equation (4.32) to be:

$$U_{flutt}^2 = -\frac{S}{2R} \pm \frac{1}{2R}\sqrt{S^2 - 4RT} \tag{4.33}$$

where the smaller positive value corresponds to the critical flutter speed.

In the cases that $F_1 = 0$ or $D_1/F_1 > 0$ in equation (4.31), or $J = 0$ or $S^2 - 4RT < 0$ in equation (4.33), the stability condition can be determined from the criterion (4.30) by calculating all coefficients in equation (4.28) with a slightly increased air speed, U, above zero. This may result in infinite (or zero) divergence/flutter speed, indicating aerodynamically stable (or unstable) motion in each situation. The flutter instability is usually reached first in the design of an aircraft wing. However, in some cases such as when the fibers are orientated at a certain angle, divergence can occur first, thus divergence needs to be considered as well.

Flutter/divergence speed by quasi-steady aerodynamic forces

Similarly, substituting equation (4.20) to (4.21) yields the governing equation with quasi-steady aerodynamic forces as:

$$\begin{aligned} EI\frac{\partial^4 h}{\partial y^4} - K\frac{\partial^3 \phi}{\partial y^3} + m\frac{\partial^2 h}{\partial t^2} + S_y\frac{\partial^2 \phi}{\partial t^2} + L_1 U(\frac{\partial h}{\partial t} + U\phi) + L_2 U\frac{\partial \phi}{\partial t} = 0 \\ GJ\frac{\partial^2 \alpha}{\partial y^2} - K\frac{\partial^3 h}{\partial y^3} - I_y\frac{\partial^2 \phi}{\partial t^2} - S_y\frac{\partial^2 h}{\partial t^2} + M_1 U(\frac{\partial h}{\partial t} + U\phi) + M_2 U\frac{\partial \phi}{\partial t} = 0 \end{aligned} \tag{4.34}$$

where L_1 and M_1 are the same as in equation (4.22) and

$$L_2 = L_1 b\left(\frac{3}{4} - \frac{x_o}{b}\right),\ M_2 = M_1 b\left(\frac{3}{4} - \frac{x_o}{b}\right) - \frac{\rho b^3 \pi}{16}$$

Substituting the same assumed harmonic solution by equation (4.23) into equation (4.34) and eliminating $e^{\lambda t}$ yields

$$A[EIf^{iv} + f(m\lambda^2 + L_1\lambda U)] + B[-Kg''' + g(L_1U^2 + S_y\lambda^2 + L_2\lambda U)] = 0 \tag{4.35.1}$$

$$A[Kf''' + f(S_y\lambda^2 - M_1\lambda U)] + B[-GJg'' - g(M_1U^2 - I_y\lambda^2 + M_2\lambda U)] = 0 \tag{4.35.2}$$

where L_1, L_2, M_1 and M_2 are the same as in equation (4.34). With the same assumption on $f_1(y)$, $f_2(y)$, $g_1(y)$ and $g_2(y)$ as expressed with equation (4.25), multiplying equation (4.35.1) by $f(y)$ and equation (4.35.2) by $g(y)$, and integrating over [0, L] yields:

$$\begin{aligned} A[a_{11} + c_{11}\lambda^2 + d_{11}\lambda U] + B[a_{12} + b_{12}U^2 + c_{12}\lambda^2 + d_{12}\lambda U] = 0 \\ A[a_{21} + c_{21}\lambda^2 + d_{21}\lambda U] + B[a_{22} + b_{22}U^2 + c_{22}\lambda^2 + d_{22}\lambda U] = 0 \end{aligned} \tag{4.36}$$

where

$$a_{11} = EI(\int_0^l f_1^{iv} f_1 dy + \int_l^L f_2^{iv} f_2 dy),\ a_{12} = -K(\int_0^l g_1''' f_1 dy + \int_l^L g_2''' f_2 dy)$$

$$a_{21} = K(\int_0^l f_1''' g_1 dy + \int_l^L f_2''' g_2 dy),\ a_{22} = -GJ(\int_0^l g_1'' g_1 dy + \int_l^L g_2'' g_2 dy)$$

$$b_{12} = L_1(\int_0^l g_1 f_1 dy + \int_l^L g_2 f_2 dy),\ b_{22} = -M_1(\int_0^l g_1^2 dy + \int_l^L g_2^2 dy)$$

$$c_{11} = m(\int_0^l f_1^2 dy + \int_l^L f_2^2 dy),\ c_{22} = I_y(\int_0^l g_1^2 dy + \int_l^L g_2^2 dy)$$

$$c_{12} = S_y(\int_0^l g_1 f_1 dy + \int_l^L g_2 f_2 dy) = c_{21}$$

$$d_{11} = L_1(\int_0^l f_1^2 dy + \int_l^L f_2^2 dy),\ d_{12} = L_2(\int_0^l g_1 f_1 dy + \int_l^L g_2 f_2 dy)$$

$$d_{21} = -M_1(\int_0^l f_1 g_1 dy + \int_l^L f_2 g_2 dy), d_{22} = -M_2(\int_0^l g_1^2 dy + \int_l^L g_2^2 dy).$$

A non-trivial solution of equation (4.36) requires that

$$\det\begin{bmatrix} a_{11} + c_{11}\lambda^2 + d_{11}\lambda U & a_{12} + b_{12}U^2 + c_{12}\lambda^2 + d_{12}\lambda U \\ a_{21} + c_{21}\lambda^2 + d_{21}\lambda U & a_{22} + b_{22}U^2 + c_{22}\lambda^2 + d_{22}\lambda U \end{bmatrix} = 0$$

or,

$$A_1\lambda^4 + B_2 U\lambda^3 + (B_1 + C_1 U^2)\lambda^2 + (D_2 U + F_2 U^3)\lambda + D_1 + F_1 U^2 = 0 \tag{4.37}$$

where the constants are given by

$$A_1 = c_{11}c_{22} - c_{12}c_{21}$$

$$B_1 = a_{11}c_{22} + a_{22}c_{11} - a_{21}c_{12} - a_{12}c_{21},\ B_2 = c_{11}d_{22} + c_{22}d_{11} - c_{21}d_{12} - c_{12}d_{21}$$

$$C_1 = b_{22}c_{11} + d_{11}d_{22} - b_{12}c_{21} - d_{12}d_{21}$$

$$D_1 = a_{11}a_{22} - a_{12}a_{21},\ D_2 = a_{11}d_{22} + a_{22}d_{11} - a_{21}d_{12} - a_{12}d_{21}$$

$$F_1 = a_{11}b_{22} - a_{21}b_{12},\ F_2 = b_{22}d_{11} - b_{12}d_{21}$$

The characteristic equation (4.37) can then be rewritten as

$$A_0\lambda^4 + B_0\lambda^3 + C_0\lambda^2 + D_0\lambda + E_0 = 0 \tag{4.38}$$

where

$$A_0 = A_1,\ B_0 = B_2 U,\ C_0 = B_1 + C_1 U^2,\ D_0 = D_2 U + F_2 U^3,\ E_0 = D_1 + F_1 U^2.$$

The stability condition requires that all roots of equation (4.38) have negative real parts. The necessary and sufficient condition is that the coefficients A_0, B_0, C_0, D_0, E_0 and the Routh discriminant

$$R = B_0 C_0 D_0 - B_0^2 E_0 - D_0^2 A_0$$

have the same sign (Fung, 1969). Since $A_0 = A_1$ is always positive, the stability condition becomes

$$B_0 > 0,\ C_0 > 0,\ D_0 > 0,\ E_0 > 0 \text{ and } R > 0 \tag{4.39}$$

Again, since E_0 and R become zero before either B_0, C_0 or D_0 does with increasing air speed, the stability condition can be further simplified to evaluate the signs of E_0 and R. At the critical condition, $E_0 = 0$ or/and $R = 0$.

1) If $E_0 = 0$, equation (4.38) has a root $\lambda = 0$, which results in the same divergence speed as in equation (4.31).

2) If $R = 0$, substitution of B_0, C_0, D_0 and E_0 for R yields

$$U^2(JU^4 + MU^2 + N) = 0 \tag{4.40}$$

where

$$J = B_2C_1F_2 - A_1F_2^2$$

$$M = B_2C_1D_2 - B_2^2F_1 + B_1B_2F_2 - 2A_1D_2F_2$$

$$N = B_1B_2D_2 - B_2^2D_1 - A_1D_2^2$$

The solution $U = 0$ in equation (4.40) is trivial since it only indicates that the beam has a harmonic response in still air. The actual flutter speed can be determined from equation (4.40) to be:

$$U_{flutt}^2 = -\frac{M}{2J} \pm \frac{1}{2J}\sqrt{M^2 - 4JN} \tag{4.41}$$

where the smaller positive value corresponds to the critical flutter speed. Following the same procedure aforementioned for the cases that $J = 0$ or $M^2 - 4JN < 0$ in equation (4.41), the stability condition can be finally determined.

C) Some plots for the wing without cracks

The composite beam consists of several plies aligned in the same direction. In each ply the material is assumed orthotropic with respect to its axes of symmetry. Material properties of each ply are taken to be the same as in Chapter 3. Although the three elastic parameters (*EI*, *GJ* and *K*) are calculated directly form the beam model, they are equivalent to those obtained by a box-beam model, and can be further determined numerically or experimentally by the real composite wing structure. Values from a real composite wing certainly benefit the analysis, affecting the actual flutter/divergence speed. However, the present research does not aim at an accurate calculation of either flutter or divergence speed; instead our focus is on the variation or rate of variation in the presence of a surface crack. Therefore, the variation of flutter and divergence speeds predicted by Galerkin's method here for an intact wing with respect to different fiber angles should be treated as a profile, rather than an accurate

mapping. The model geometry of the cantilever wing is taken to be: length L = 1.0 m, width b = 0.25 m, thickness t = 0.02 m and offset of the center of gravity S = 0.05 m. In the following sections, θ stands for the fiber angle, and V the fiber volume fraction, $\eta = a/b$ the crack ratio, and $\xi_c = l/L$ the dimensionless crack location.

It may be of interest to first explore the variation of the three elastic parameters, natural frequencies and flutter/divergence speed with respect to fiber angles for the beam without any cracks. Figure 4.2 illustrates the variation of EI, GJ, K and Ψ ($= K/\sqrt{EI \cdot GJ}$) for fiber angles between 0° and 180°. Figure 4.3 shows the variation of the first four natural frequencies for the same range of fiber angles. Figure 4.4 is the plot of normalized flutter and divergence speeds for steady aerodynamic forces, while the same plot for quasi-steady aerodynamic forces is shown in Figure 4.5.

Figure 4.2 indicates the symmetry of EI and GJ and antisymmetry of K and Ψ with respect to the fiber angle at 90° (or 0°), which is expected as the same characteristics presented in Chapter 3. However, the symmetric nature of natural frequencies for beams without the inertia coupling no longer exists for the wing model including the inertia coupling, except for the very first natural frequency as shown in Figure 4.3. The lowest mode is predominantly controlled by the bending mode during the variation of fiber angles. Plots of higher modes show the effect that either the bending or torsional mode is no longer in the shape of a certain mode but “distorted” to some extent, especially in the range that two consecutive frequencies are close to each other. However, for the variation of the lowest frequency, both the bending and torsional modes bear the shape of its first mode. The lowest coupled bending and torsional modes will be selected in the following analysis, for both the intact and cracked beams.

In Figures 4.4 and 4.5, V_D and V_F represent the divergence speed and flutter speed, respectively, and V_R is a reference speed selected to normalized V_D and V_F. Although the divergence speed is the same for either steady or quasi-steady aerodynamic models, flutter speeds predicted by the steady aerodynamics model are about 60% higher than those by the quasi-steady aerodynamic model for fiber angles less than 50° or greater than 149°, and about

35% higher for fiber angles between 50° and 94°. Flutter speeds predicted by the steady aerodynamic model are much less conservative. Another significant difference is that the quasi-steady aerodynamic model predicts flutter instabilities for fiber angles between 94° and 149 with a severe instability around 97°, while the steady aerodynamic model indicates no flutter for the same range of fiber angles. Flutter speeds can be higher or lower than divergence speeds, depending on the range of fiber angles; either speed can go to infinity at a certain range of fiber angles. The same phenomena were also observed by Cesnik *et al*. (1996) who investigated variation of flutter and divergence speeds of composite wing with box-beam models. Moreover, changing the elastic axis location or inertia axis location significantly affects both divergence and flutter curves in the way that the curves are not only shifted but also "re-shaped." The inertia axis ahead of the elastic axis (with a negative *S* value) tends to improve aerodynamic stabilities by increasing both flutter and divergence speeds for the same range of fiber angles, the same phenomenon for conventional wing structures (Dowell *et at*., 1978). The current research assumes that the elastic axis is located in the leading half chord with the distance to the leading edge as $x_o = 0.45b$, close to the center line, while the inertia axis is $0.2b$ aft. This is a reasonable assumption for a cantilever composite wing with a large aspect ratio.

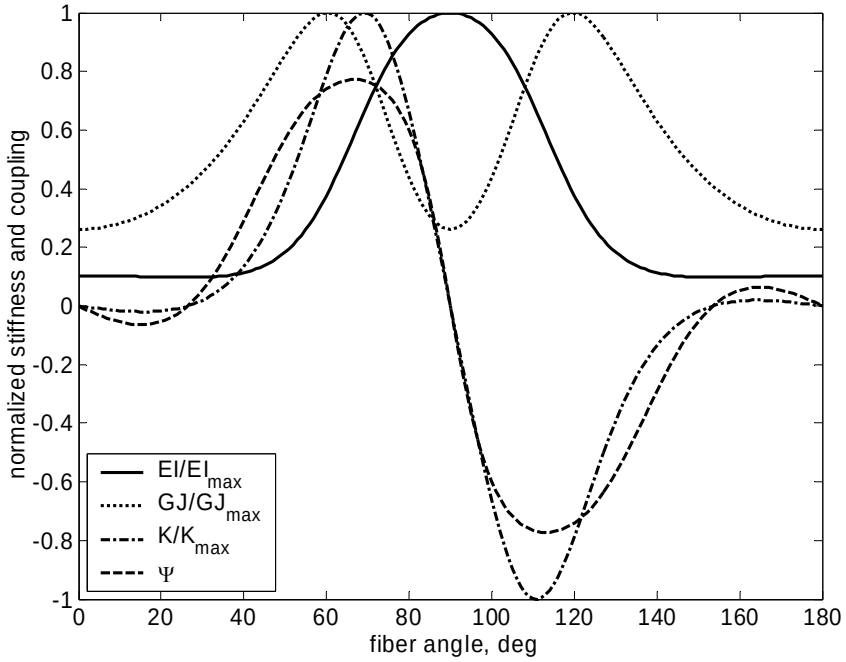

Figure 4.2 Variation of the elastic parameters *EI*, *GJ*, *K* and Ψ with respect to fiber angles.

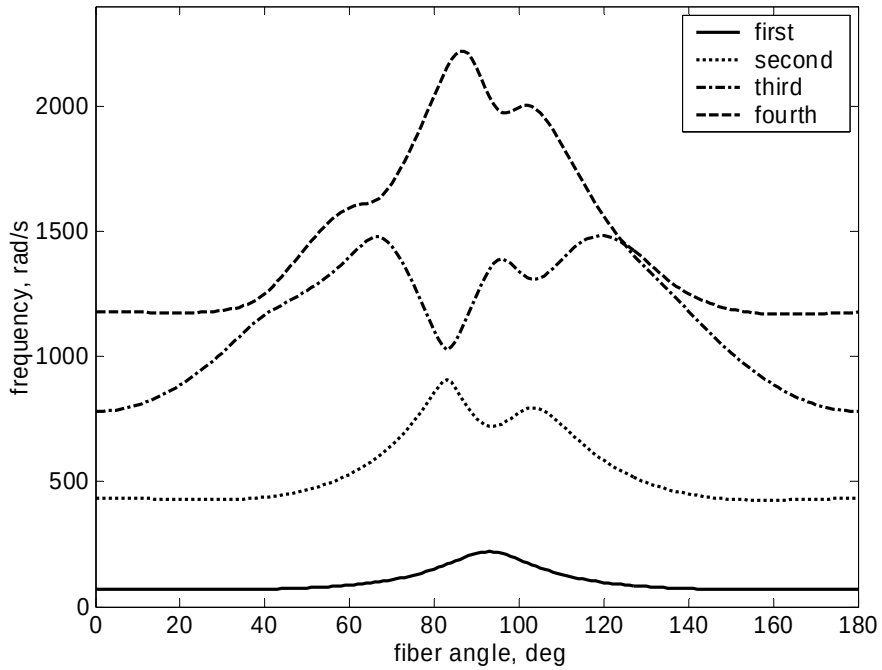

Figure 4.3 Variation of the first four natural frequencies with respect to fiber angles.

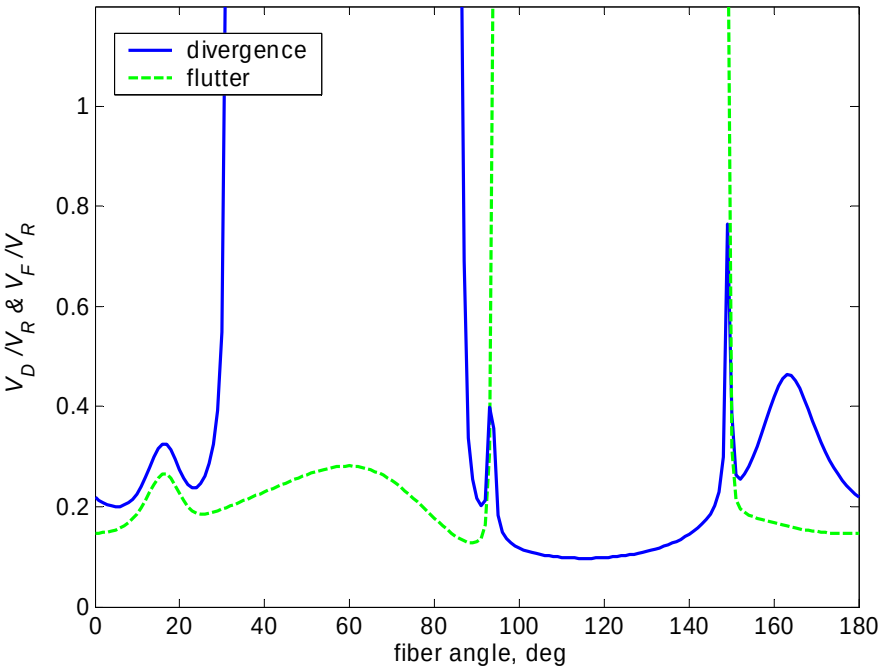

Figure 4.4 Variation of flutter and divergence speeds w.r.t. fiber angles (steady aero forces).

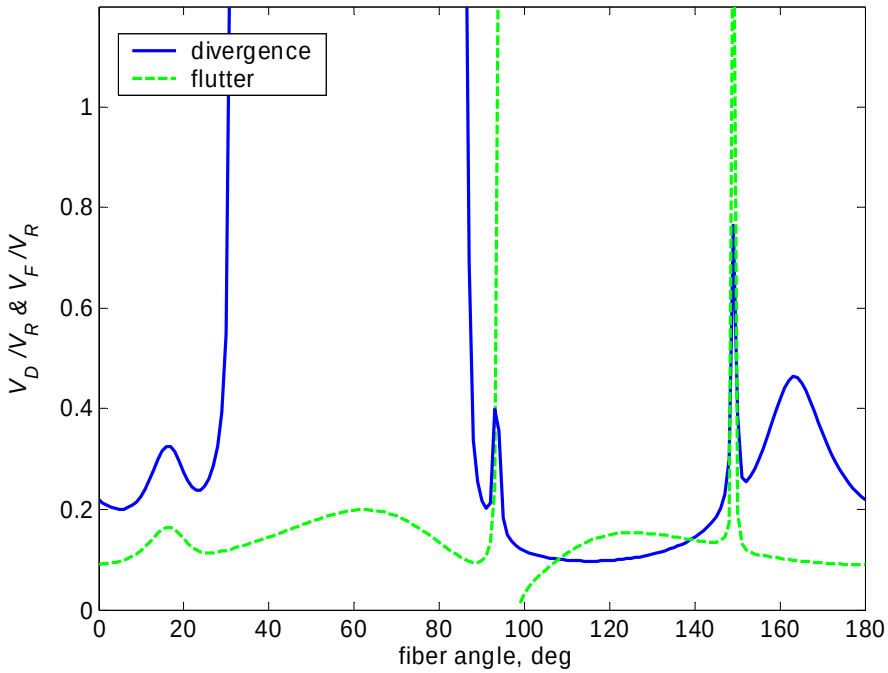

Figure 4.5 Variation of flutter and divergence speeds w.r.t. fiber angles (quasi-steady aero forces).

4.4 Effects of Crack Ratios and Fiber Angles

The edge crack reduces the stiffness of the composite wing so that the global vibration modes are disturbed. The disturbance is not equally exerted on the coupled bending mode or torsional mode, as indicated in the case of no inertia coupling in Chapter 3. A plot of the first coupled bending and torsional modes in terms of the crack ratio indicates that the bending mode is always disturbed more than the torsional mode due to the crack.

To investigate effects of crack to flutter/divergence speed at different fiber angles, the following 9 fiber angles are selected: 10°, 20°, 30°, 75°, 90°, 110°, 130°, 146° and 155°. The selection is based on the variation of flutter speed shown in Figure 4.4 and 4.5. A fiber angle is chosen for the range in which the flutter speed experiences either increasing or decreasing. For the crack located at ξ_c = 0.2, the normalized divergence speed with respect to the crack

ratio is plotted in Figure 4.6, and Figure 4.7 and 4.8 illustrate the variation of flutter speeds. The corresponding speed in the absence of the crack is selected as the reference speed V_R.

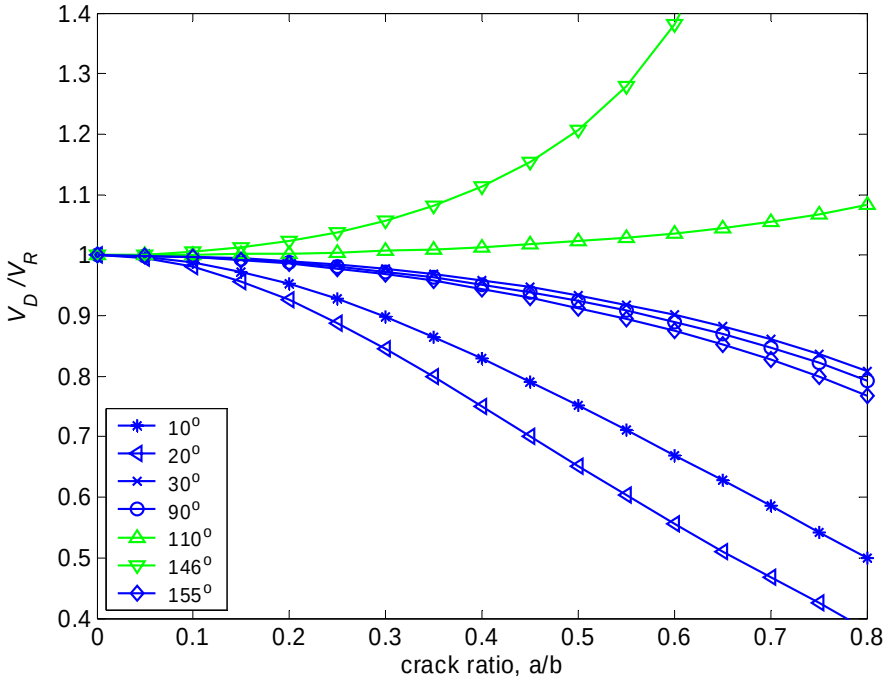

Figure 4.6 Variation of divergence speed w.r.t. crack ratio.

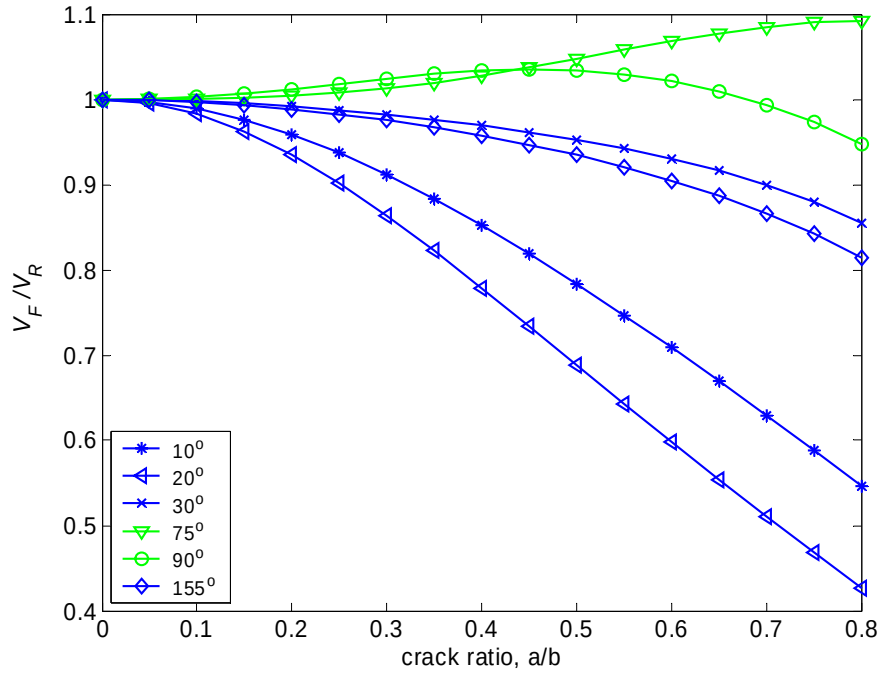

Figure 4.7 Variation of flutter speed w.r.t. crack ratio (steady aero-forces).

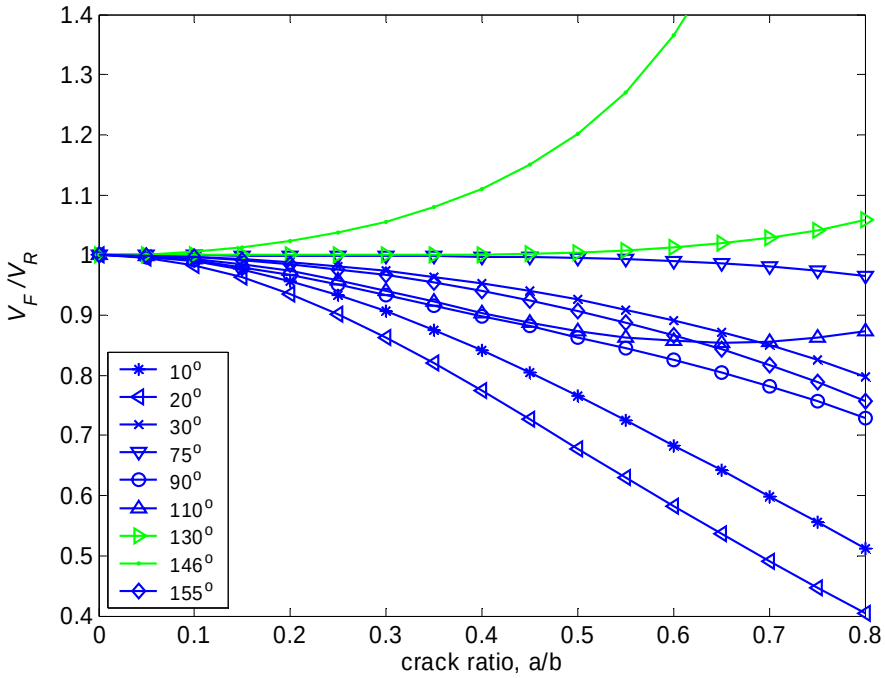

Figure 4.8 Variation of flutter speed w.r.t. crack ratio (quasi-steady aero-forces).

The divergence speed shown in Figure 4.6 tends to increase with the crack ratio increased for the fiber angle at 110° or 146°, while in any other situations the divergence speed decreases with the increasing crack ratio. On the other hand, the flutter speed predicted by the steady aerodynamic model tends to increase slightly for fiber angle at 75°, with an increase-decrease variation for fiber angle at 90°. At any other fiber angles the speed decreases with the increasing crack ratio. The flutter speed predicted by the quasi-steady aerodynamic model, however, decreases with the increasing crack ratio for most fiber angles. The rate of decrease is much higher for smaller fiber angles. An increase is only observed for the fiber angle at 130° and 146° where the steady aerodynamic model predicts no flutter instability. Recall that due to the existence of inertia coupling, the cracked mode shapes are no longer symmetric when the fiber angle is symmetric by the elastic axis. The change in divergence/flutter speed of the composite wing is now affected by the interaction of the crack ratio, the elastic bending-torsion coupling of the material and the inertia bending-torsion coupling of the wing structure.

The phenomenon that a crack tends to increase divergence/flutter speeds at a certain range of fiber angles was also observed by Lin *et al*. (1991) who investigated the aeroelastic stabilities of a cracked anisotropic panel. For a wing structure, the flutter instability usually occurs when two consecutive frequencies coalesce or tend to "merge" (Bisplinghoff *et al*., 1996). It is true that at any fiber angles and for a fixed crack (both magnitude and location), solving equation (4.38) for the quasi-steady aerodynamic model indicates that the first two critical frequencies tend to merge with increasing airspeed. However, with the directional stiffness changing with fiber angles, the presence of a crack may cause changes in mode shapes such that certain critical frequencies may be increased or remain unchanged while other critical frequencies may be decreased. In other words, there exists the chance that a crack may result in two consecutive frequencies separating rather than merging with each other.

To illustrate the crack effects, two fiber angles (20° and 146°) are selected in solving equation (4.38) for critical frequencies with the quasi-steady aerodynamic model. When the wing has no cracks, there is no significant difference between elastic parameters and the first two natural frequencies for the two fiber angles, as shown in Table 4.1. For the airspeed is fixed at 100 m/s (below divergence and flutter speeds), Figure 4.9 clearly indicates that with increasing crack ratio, the two critical frequencies (obtained by equation (4.38)) tend to coalesce for fiber angle at 20° and separate for fiber angle at 146°.

Table 4.1 Elastic parameters and the first two natural frequencies of the intact wing

Fiber angle	EI, N·m^2	GJ, N·m^2	Ψ, N·m^2	The 1st natural frequency, rad/s	The 2nd natural frequency, rad/s
$\theta = 20°$	3635.2	7537.1	-0.054	69.8	429.1
$\theta = 146°$	3722.3	11391.3	-0.132	70.5	435.9

It should be noted that the cracked composite beam model as well as the cracked composite wing model is valid only for small cracks, since a larger crack may violate the assumption that the system is linear and involves only small displacements. Therefore, it is suggested that for a crack ratio larger than 0.5, predictions shown in all related plots should not be relied on as an accurate result.

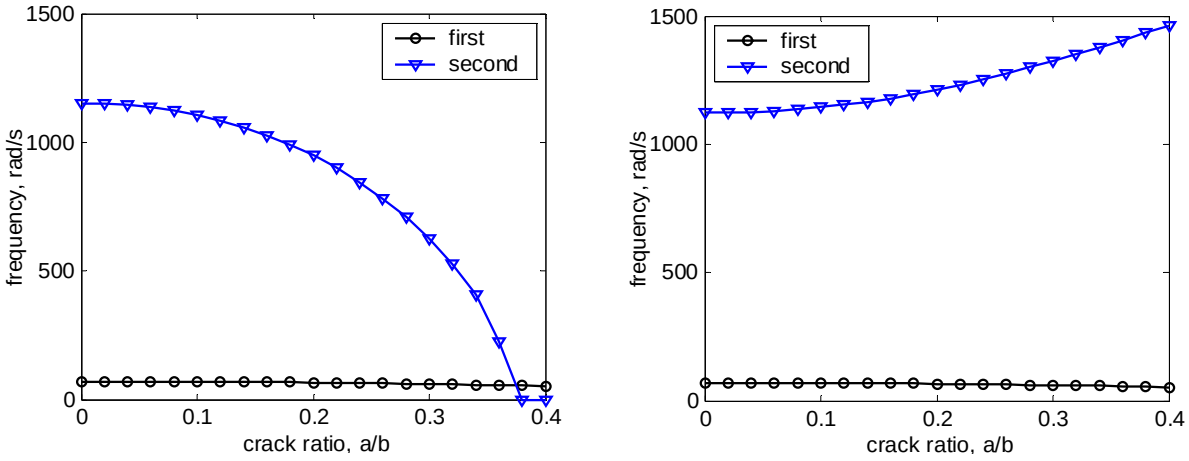

(a) Fiber angle $\theta = 20°$ (b) Fiber angle $\theta = 146°$

Figure 4.9 Variation of the two critical frequencies w.r.t. crack ratio at a constant airspeed.

4.5 Effects of Crack Locations and Fiber Angles

For the case that the crack ratio is constant at η = a/b = 0.3, effects of the dimensionless crack location are shown in Figure 4.10 for divergence speeds and Figures 4.11 and 4.12 for flutter speeds.

For smaller fiber angles (θ = 10° or 20°) where the bending stiffness is low and the elastic coupling is weak, the lowest flutter and divergence speeds are found near the root of the wing as shown in the figures below. For the fiber angle larger than 30°, the overall variation in divergence speeds is within the 5% range. When the crack location moves along the wing span, the flutter speed predicted by the quasi-steady aerodynamic model usually does not change monotonically with the crack location. Whether a crack near the wing root reduces the flutter speed more than the one at other locations is certainly affected by the elastic and inertia properties of the wing, and the question may not be answered simply by "yes" or "no."

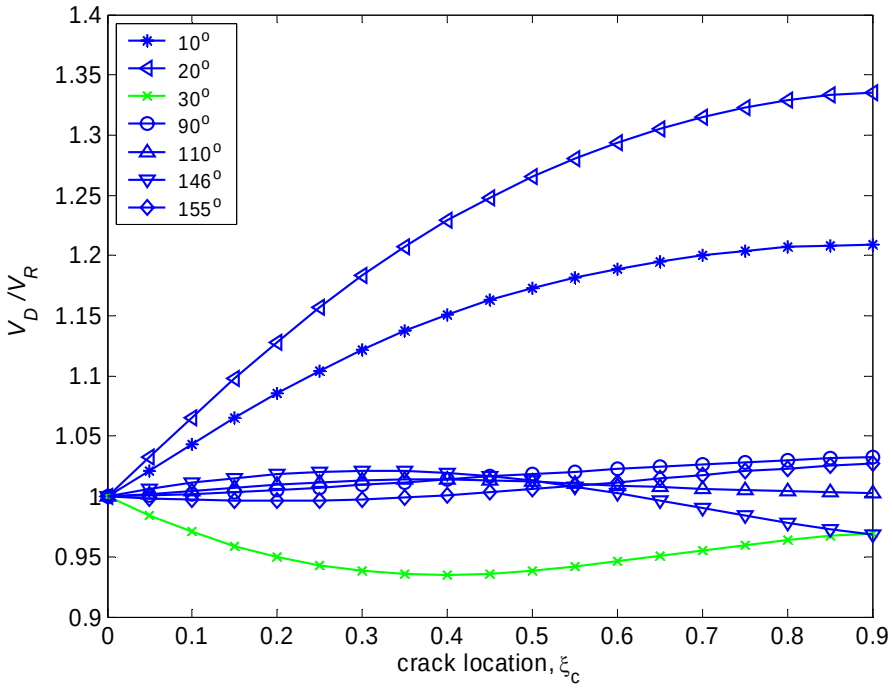

Figure 4.10 Variation of divergence speed w.r.t. crack location.

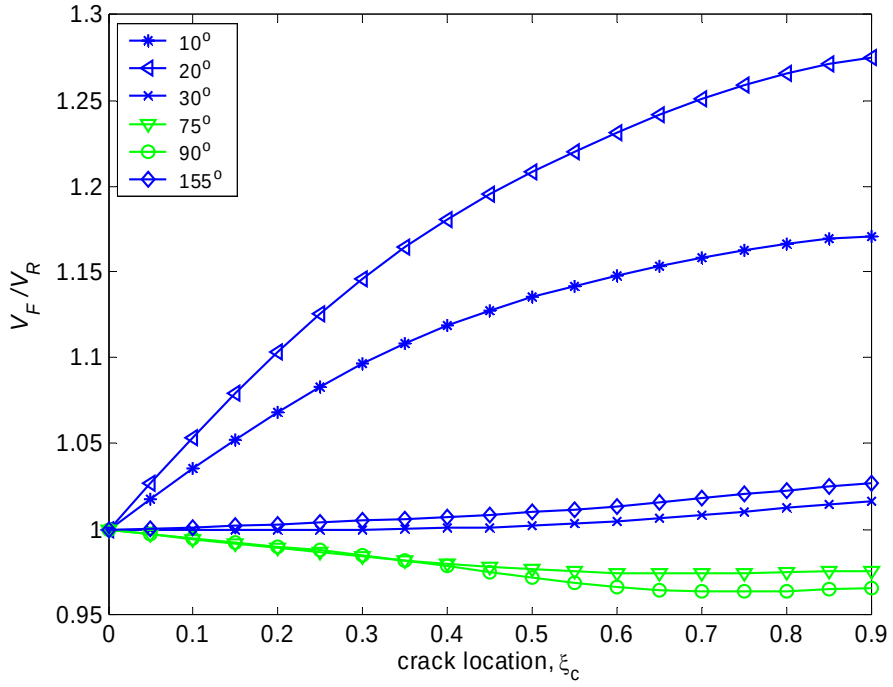

Figure 4.11 Variation of flutter speed w.r.t. crack location (steady aero-forces).

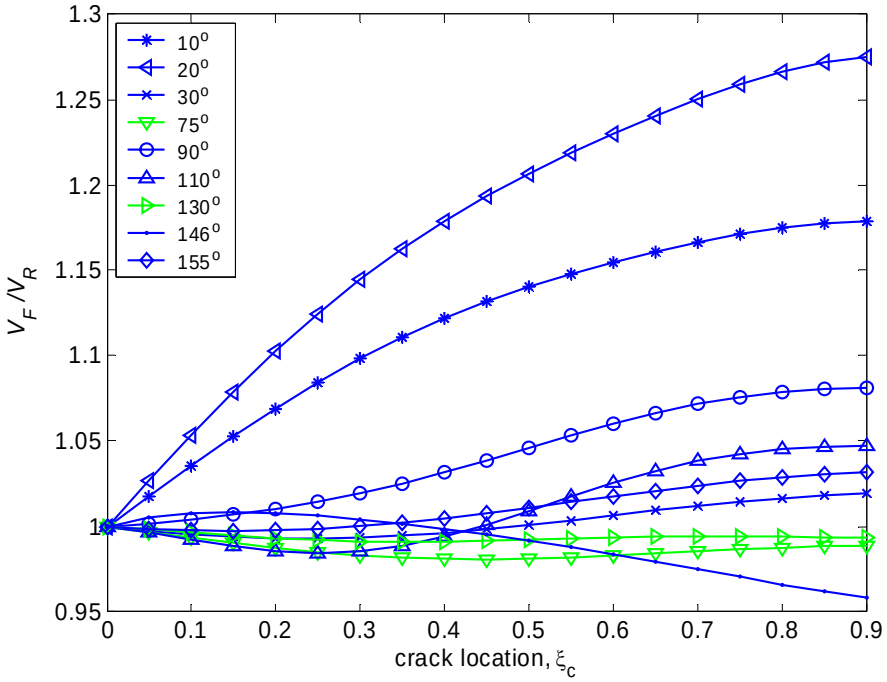

Figure 4.12 Variation of flutter speed w.r.t. crack location (quasi-steady aero-forces).

4.6 Summary

The aeroelastic characteristics of an unswept composite wing with an edge crack are investigated. The cracked wing is modeled by a cracked composite cantilever developed in Chapter 3 and the inertia coupling terms are included in the governing equations. The critical flutter and divergence speeds are obtained by Galerkin's method in which the fundamental mode shapes of the cracked beam in free vibration are used. The mode shapes satisfy all boundary conditions including those at the crack location and thus carry most of the information of the cracked beam for the final approximate solution. Both steady and quasi-steady aerodynamic forces are considered in the analysis.

The divergence/flutter speed varies with the elastic axis location, the inertia axis location, fiber angles, and the crack ratio and location. For the elastic axis fixed in the leading half chord with the inertia axis aft, the divergence/flutter speed is more sensitive to the stiffness orientation than to the crack itself. At certain fiber angles, the presence of a

crack tends to increase the flutter or divergence speed, a similar phenomenon as observed by Lin *et al* (1991). The instability boundaries that are constant for an isotropic wing become alternating with the varying fiber angles of a composite wing (Lin *et al*, 1989). The anisotropy of the composite wing introduces many completely different phenomena in the aeroelastic instability.

The flutter speed tends to increase with the crack ratio increased at certain fiber angles. However, in most situations the flutter speed decreases with the increasing crack ratio, especially for that predicted by the quasi-steady aerodynamic model. The rate of change is higher with smaller fiber angles. Although an edge crack does not always reduce either flutter or divergence speed, it does reduce the stability boundaries in most cases in terms of stiffness orientation considered in the present research. As to a crack of fixed magnitude, the lowest flutter speed is observed when the crack approaches the root of the composite wing with smaller fiber angles. However, both flutter and divergence speeds experience variation with different crack locations, and the magnitude of variation with respect to the crack location is relatively small.

Once a crack is found on a composite wing, monitoring of the crack growth could be more critical to determine the aeroelastic stability of the wing, especially in the case that the crack does not result in a flutter speed drop due to certain fiber orientation. But in the case that a crack does reduce the flutter speed, a fast drop in flutter speed might result in a catastrophic failure by a small crack that has not ever grown. When coupled with a crack detection algorithm, the connection presented here between crack properties and flutter speed may be used as a damage prognosis tool to predict how the system will behave under future loading.

Contribution

The following lists contributions to the literature on cracked composite wings:

1) An analytical model of cracked composite wings including both elastic and inertia couplings between bending and torsion is developed. Free vibration of the cracked composite wing is analyzed with the model.

2) Aeroelastic characteristics of an unswept composite wing with an edge crack are investigated. Changes in flutter and divergence speeds due to the presence of the crack and under the condition of varying stiffness orientation are studied. The current research contributes to the literature by adding an analytical model on a cracked composite wing along with the primary study on the crack induced changes in aeroelastic stabilities. It may also be used as a damage prognosis for future composite wing structures.

Chapter 5

Crack Detection by Changes in Natural Frequencies

5.1 Introduction

Damage detection by changes in natural frequencies has been widely implemented in model-based damage monitoring. Compared to other modal parameters, natural frequencies are relatively easier to measure with significantly high accuracy. Sensor locations and numbers are usually not restricted as opposed to the determination of mode shapes. As the global nature of a structure, natural frequencies may not be sensitive to the local incipient damage. In some situations such as damage detection on bridges and buildings, changes in environmental conditions (e.g., climate changes) even in a single day could affect natural frequencies more than the possible damage by changing mass and stiffness of the structure. Precaution should be taken by using frequency changes alone for damage detection.

On the other hand, many researchers have successfully demonstrated the identification of various damages by using frequency changes, both theoretically and experimentally. For structures that can be accurately modeled by finite element methods or analytical approaches, the location of damage can be related to relative frequency changes or the rate of change of frequency. In this chapter, the Cawley-Adams criterion (Cawley and Adams, 1979) is taken to explore the possibility of determining both the crack location and magnitude. Criteria based on frequency sensitivities are usually capable of locating the damage accurately with

the help of reliable models. In the presence of measurement errors, it is very difficult to determine the damage magnitude, even with an accurate model (Palacz and Krawczuk, 2002). In this chapter, a strategy similar to the rank-ordering of eigenfrequency shifts developed by Armon *et al*. (1994) is applied so that the Cawley-Adams criterion become capable of detecting both the crack location and magnitude even when measurement errors are considered.

The threshold of measurement errors related to the crack size and location is also investigated. The cracked composite cantilever beam addressed in Chapter 3 is used as the reference model. Several assumptions are made before the application: 1) the beam model is calibrated and natural frequencies of the intact beam are measured accurately in a lab environment so that they can be taken as the baseline; 2) the cracked beam model developed in Chapter 3 is validated as well as calibrated so that little modeling errors exist in predicting natural frequencies of the cracked beam; 3) changes in natural frequencies result only from the single crack and no other factors such as boundary conditions, other form of damage, or changes in environmental conditions; 4) when the beam is deployed in service (e.g., aircraft wings in the middle of flight), the source of error in determining natural frequencies results from the online measurement. The sensitivity of natural frequency to model parameter uncertainties will be addressed in Chapter 6. Note with inexplicit assumptions on the first three conditions, many researchers did not consider measurement errors for their successful damage detection based on changes in natural frequencies, e.g., Messina *et al*. (1996) and Chinchalkar (2001).

5.2 The Cawley-Adams Criterion

The Cawley-Adams criterion is based on the premise that change in stiffness is independent of frequency. The rate of frequency changes in two modes is then only a function of the damage location. For the cracked composite cantilever beam, let the non-dimensional crack location be $\lambda = \xi_c$ and the crack ratio be $\eta = a/b$. The lowest M natural frequencies are measured when the beam is free from damage and after the crack is formed.

Let $\delta\Omega_k$ be the change in frequency k by measurement with unknown damage, and $\delta\omega_k(\lambda,\eta)$ be the change in frequency k from the model prediction on a crack (λ,η). Then a matching error used to validate the prediction can be defined as

$$e_{ij}(\lambda,\eta)=\begin{cases}\dfrac{\delta\Omega_i/\delta\Omega_j}{\delta\omega_i/\delta\omega_j}-1 & if\ \dfrac{\delta\Omega_i}{\delta\Omega_j}\geq\dfrac{\delta\omega_i}{\delta\omega_j}\\ \dfrac{\delta\omega_i/\delta\omega_j}{\delta\Omega_i/\delta\Omega_j}-1 & if\ \dfrac{\delta\omega_i}{\delta\omega_j}\geq\dfrac{\delta\Omega_i}{\delta\Omega_j}\end{cases} \tag{5.1}$$

A total matching error of the prediction on the crack is summed by

$$e(\lambda,\eta)=\sum_{i=1}^{M-1}\sum_{j=i+1}^{M}e_{ij}(\lambda,\eta) \tag{5.2}$$

If normalized with the minimum value, equation (5.2) will give a crack indicator as

$$E(\lambda,\eta)=\frac{e_{\min}}{e(\lambda,\eta)} \tag{5.3}$$

where $E(\lambda,\ \eta)$ is less than or equal to 1, with 1 indicating the crack location and magnitude. In the following analysis otherwise specifically stated, "crack detection" means determining both the location and magnitude of the crack.

For one-dimensional cracked beams made of isotropic materials where only bending modes are concerned, the largest frequency reduction of a certain mode always happens when the crack is located at the largest curvature of that mode shape. A plot of the relative frequency reduction with respect to the crack location for each mode provides a unique tool for crack identification. Based on this observation, Armon *et al*. (1994) used the first four natural frequencies by re-ordering the fractional shifts and resorting to the plot to locate the crack vicinity. However, for the cracked composite beam involving coupled bending and torsional modes, the largest frequency reduction no longer coincides with either the largest bending curvature or torsional curvature, as indicated in Chapter 3. A similar plot (of either bending mode or torsional mode) can not be readily used to locate the crack. At certain fiber orientation, vibration of the composite beam may be predominantly controlled by either the bending mode or torsional mode. With the variation of fiber angles, both the mode and the order may be changed as illustrated by Figure 5.1 where 1B refers to the first bending mode, 1T the first torsional mode, and 2B the second bending mode, and so on.

As indicated in Chapter 3, frequency reduction in the case of strong bending-torsion coupling has a different pattern than does the weakly coupled case due to the different fiber orientation. In the next sub-section, two cases will be considered: strong bending-torsion coupling ($\theta = 70°$) and weak bending-torsion coupling ($\theta = 30°$).

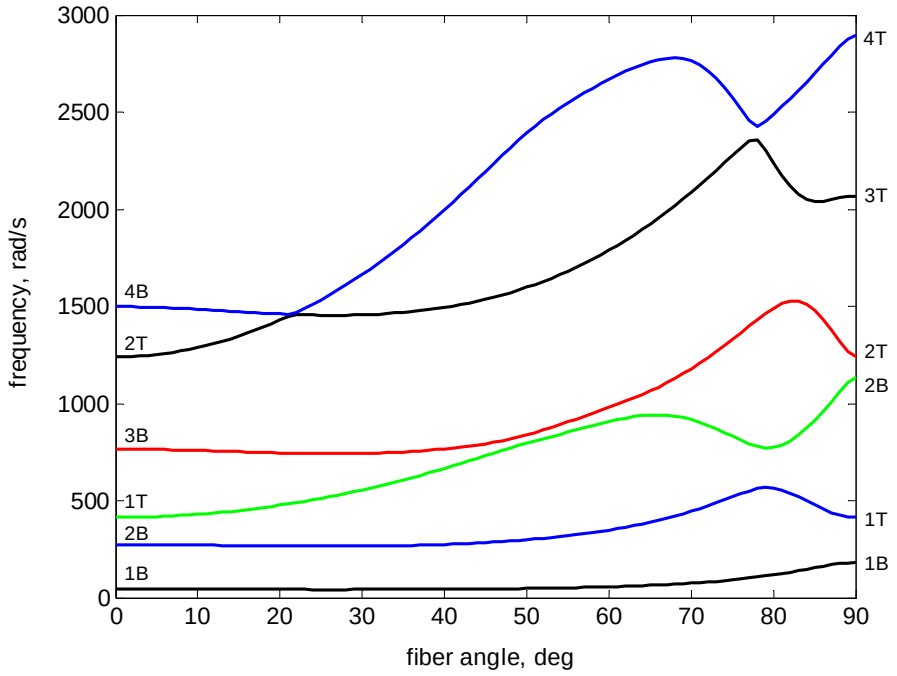

Figure 5.1 Variation of first 6 natural frequencies w.r.t. fiber angles.

5.3 Crack Detection by Means of Natural Frequency Changes

In the following sections, the composite beam is assumed to have the same geometry and material properties as in Chapter 3. The fiber volume fraction is set at $V = 0.5$. It is very common to consider the lowest natural frequencies. However, increasing the number of frequencies does not necessarily increase the accuracy in the presence of measurement errors. This issue is unsolved in Palacz and Krawczuk (2002) who replaced the first two frequency changes with the first four frequency changes and found the plots are still unable to identify both the crack location and size in the cracked isotropic beam. The following will address three fundamental questions: 1) the effects of the number of frequencies and the strategy to

select frequencies for crack detection; 2) the effects of measurement errors; 3) the threshold of measurement errors for different crack size and location.

A) When the bending-Torsion coupling is strong (θ = 70°)

Assume that the crack with ratio $\eta = a/b = 0.3$ is located at $\lambda = \xi_c = 0.3$. Without measurement errors involved, the first ten natural frequencies, before and after the damage, are listed in Table 5.1. In the table, f refers to natural frequencies of the intact beam while f_d refers to those of the damaged beam.

Table 5.1 The first ten natural frequencies, θ = 70°, without measurement errors

rad/s	1st	2nd	3rd	4th	5th	6th	7th	8th	9th	10th
f	75.26	445.90	916.12	1179.69	2089.93	2762.14	3253.14	4062.82	5162.14	5202.32
f_d	67.95	441.88	665.15	1144.80	2015.08	2758.13	3252.38	3879.50	4381.99	5023.80
f-f_d	7.31	4.02	250.97	34.89	74.85	4.01	0.76	183.32	780.15	178.52
(%)	(9.7)	(0.9)	(27.4)	(2.9)	(3.6)	(0.14)	(0.02)	(4.5)	(15.1)	(3.4)

Without measurement errors, the crack can be detected even with the first two natural frequencies as shown in Figure 5.2. Increasing the number of frequencies does not affect the accuracy.

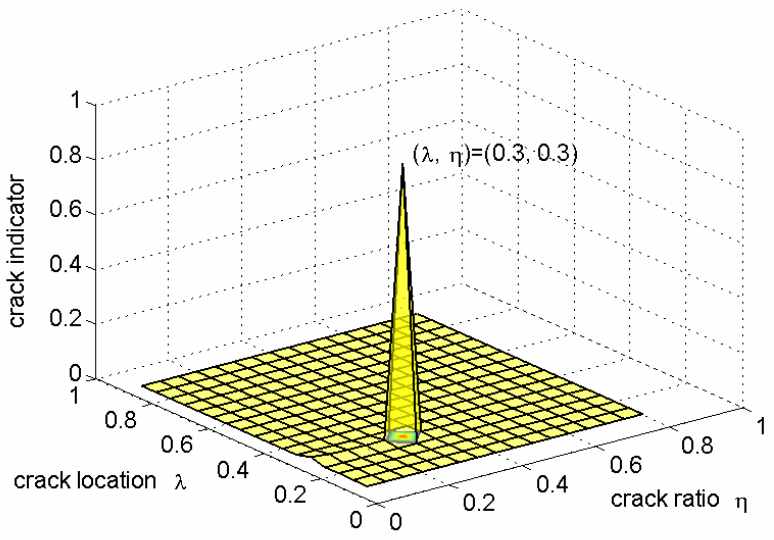

Figure 5.2 Crack detection by the first 2 frequencies, θ = 70°, no measurement errors.

However, with a 1% error in each measured frequency, it becomes difficult to detect the crack by using the first two up to the first ten frequencies. The first ten natural frequencies with the measurement errors are listed in Table 5.2. The plots of damage indicator of the first 4, 6, 8 and 10 frequencies are shown in Figures 5.3 – 5.6. Table 5.3 re-arranges the ten frequencies in the descending order by the percentage reduction.

Table 5.2 The first ten natural frequencies, with measurement errors

rad/s	1st	2nd	3rd	4th	5th	6th	7th	8th	9th	10th
f	75.26	445.90	916.12	1179.69	2089.93	2762.14	3253.14	4062.82	5162.14	5202.32
f_{d_err}	68.63	437.47	671.80	1133.36	1994.93	2730.55	3219.86	3918.30	4425.81	5074.04
f- f_{d_err}	6.63	8.43	244.32	46.33	95.0	31.59	33.28	144.52	736.33	128.28
(%)	(8.8)	(1.9)	(26.7)	(3.9)	(4.5)	(1.1)	(1.0)	(3.5)	(14.3)	(2.5)

Table 5.3 The re-ordered ten natural frequencies, with measurement errors

order	1	2	3	4	5	6	7	8	9	10
rad/s	3rd	9th	1st	5th	4th	8th	10th	2nd	6th	7th
f	916.12	5162.14	75.26	2089.93	1179.69	4062.82	5202.32	445.90	2762.14	3253.14
f_{d_err}	671.80	4425.81	68.63	1994.93	1133.36	3918.30	5074.04	437.47	2730.55	3219.86
f- f_{d_err}	244.32	736.33	6.63	95.0	46.33	144.52	128.28	8.43	31.59	33.28
(%)	(26.7)	(14.3)	(8.8)	(4.5)	(3.9)	(3.5)	(2.5)	(1.9)	(1.1)	(1.0)

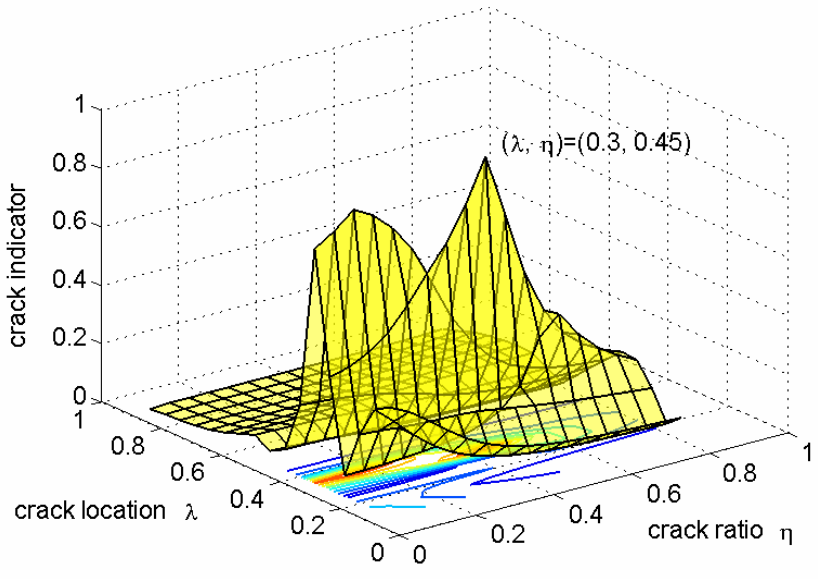

Figure 5.3 Crack detection by the first 4 frequencies, $\theta = 70°$.

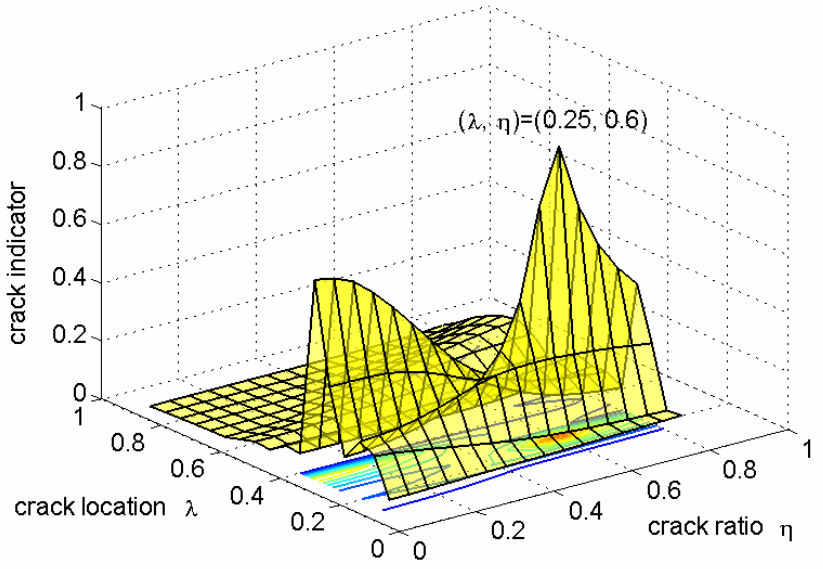

Figure 5.4 Crack detection by the first 6 frequencies, $\theta = 70°$.

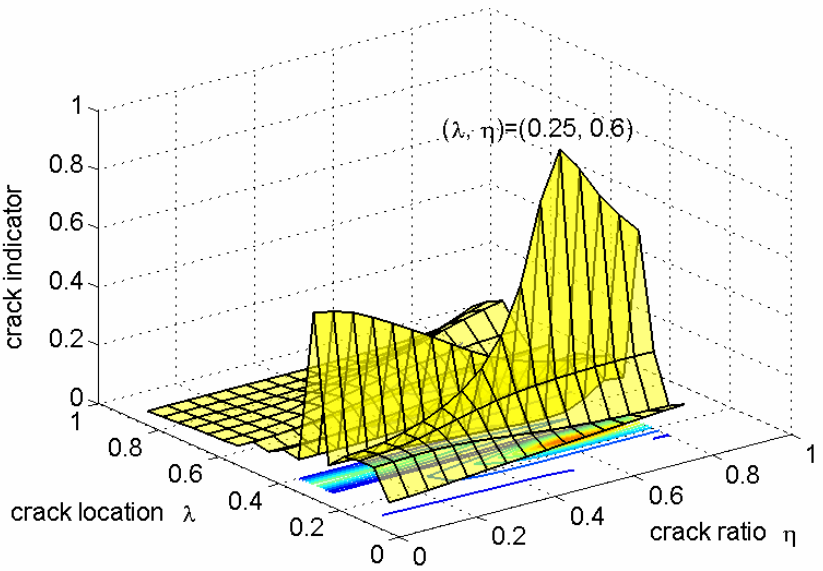

Figure 5.5 Crack detection by the first 8 frequencies, $\theta = 70°$.

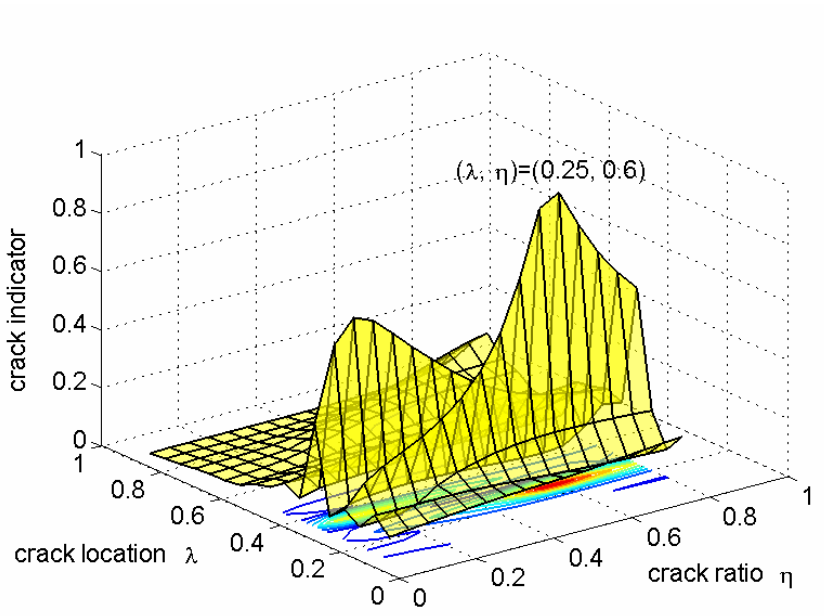

Figure 5.6 Crack detection by the first 10 frequencies, $\theta = 70°$.

If frequencies are re-ordered as listed in Table 5.3 and the higher priority is given to the frequency having larger reduction rate, the results are plotted in Figure 5.7 – 5.10.

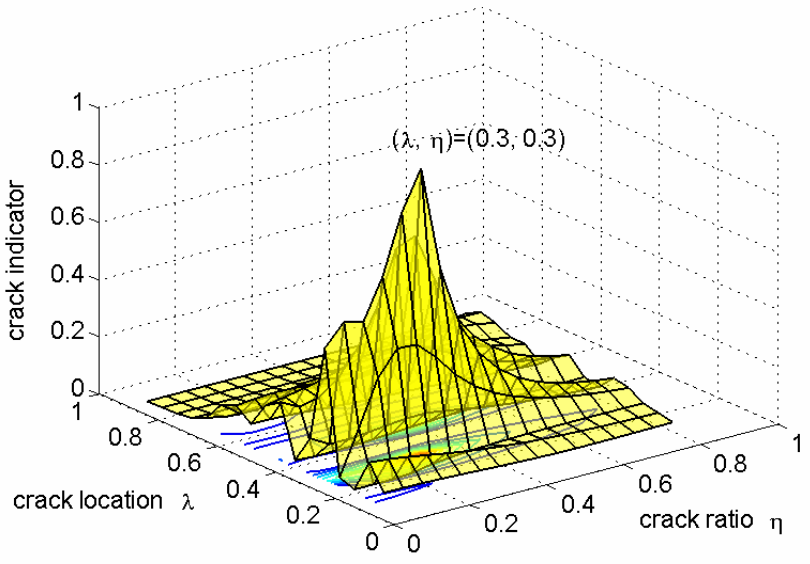

Figure 5.7 Crack detection by the first 4 re-ordered frequencies, $\theta = 70°$.

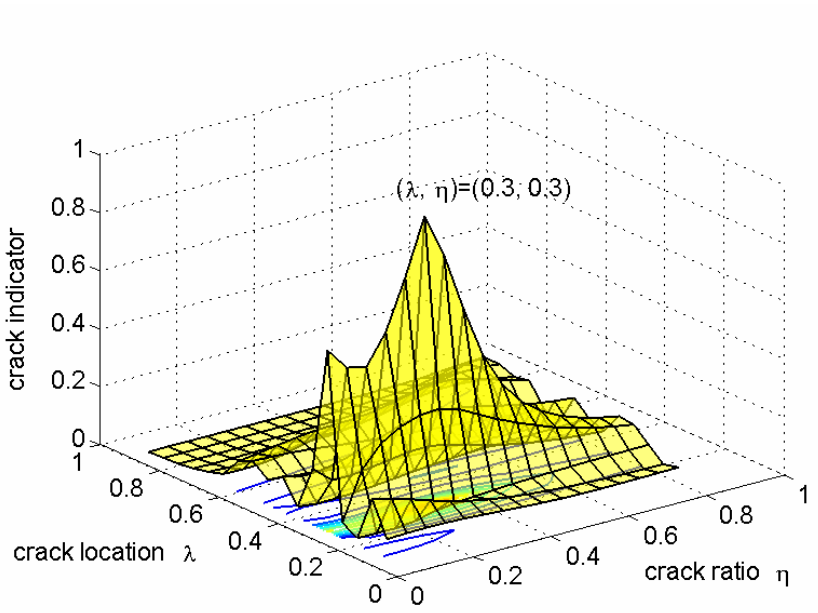

Figure 5.8 Crack detection by the first 5 re-ordered frequencies, $\theta = 70°$.

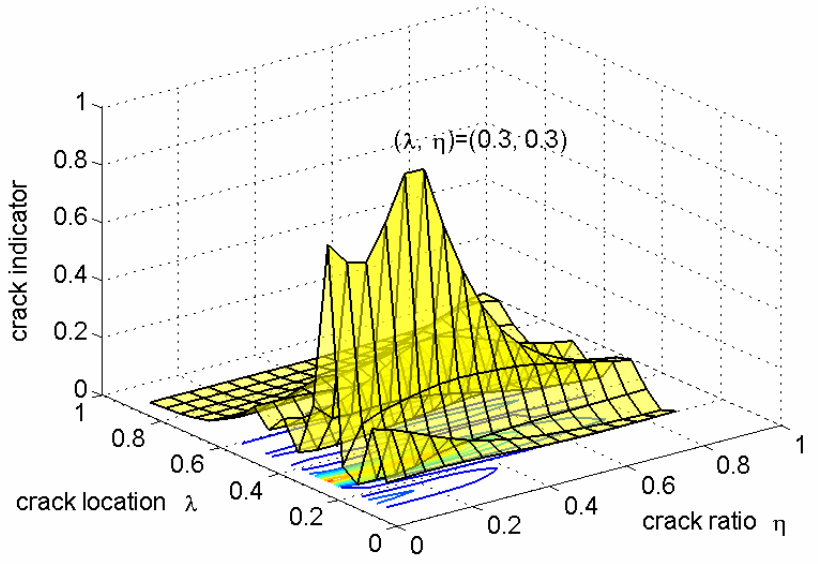

Figure 5.9 Crack detection by the first 6 re-ordered frequencies, $\theta = 70°$.

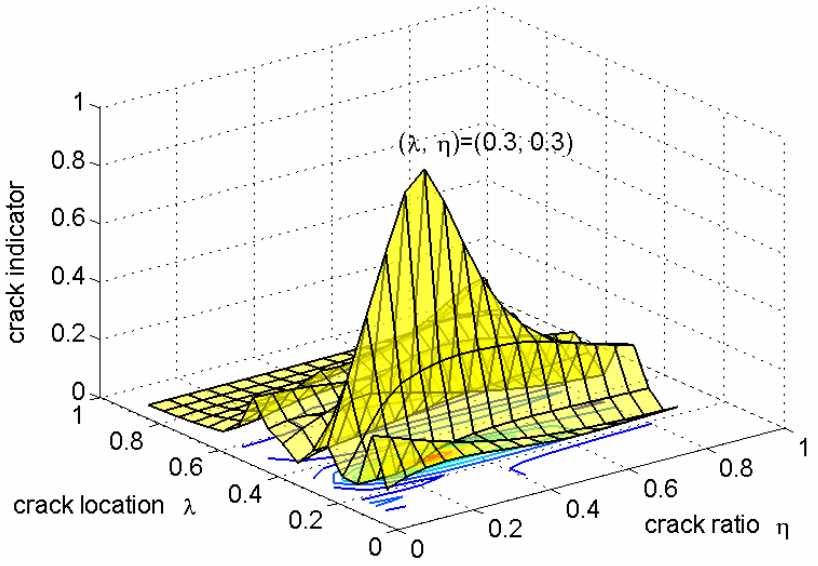

Figure 5.10 Crack detection by the first 7 re-ordered frequencies, $\theta = 70°$.

Figures 5.3 – 5.10 clearly indicate that compared to the crack size, the crack location can be detected relatively accurately by the Cawley-Adams criterion. These are consistent with published results that damage detection based on sensitivity of natural frequencies is relatively immune to measurement errors in determining damage location (Armon *et al*., 1994; Messina *et al*., 1996). However, the crack size can not be determined accurately if the number of frequencies is increased by adding frequencies consecutively from the lowest one to the highest one. The accuracy can not improved even by increasing the number of frequencies.

On the other hand, when the frequencies are re-ordered by the percentage reduction as listed in Table 5.3, an accurate result to determine both the crack location and size can be obtained. This indicates that although each natural frequency experiences a reduction due to the damage, the significance in crack detection is not equal for each frequency. The frequency having the larger percentage reduction is more significant than the one with lower percentage reduction. Again, increasing the number of frequencies does not necessarily increase the accuracy in crack detection.

To further verify the robustness of the strategy for crack detection as well as to determine the threshold of measurement error for various crack sizes and locations, the following numerical testing is conducted. Since there are ten frequencies available, they can be grouped in nine sets in terms of the number of frequencies such that Set 1 has 2 frequencies, Set 2 has 3 frequencies, and so on. In Strategy A, the frequency with lower order has higher priority to be selected to any set. In Strategy B, however, the frequency that has larger percentage reduction has higher priority to be selected. Figure 5.11 illustrates the procedure of the testing.

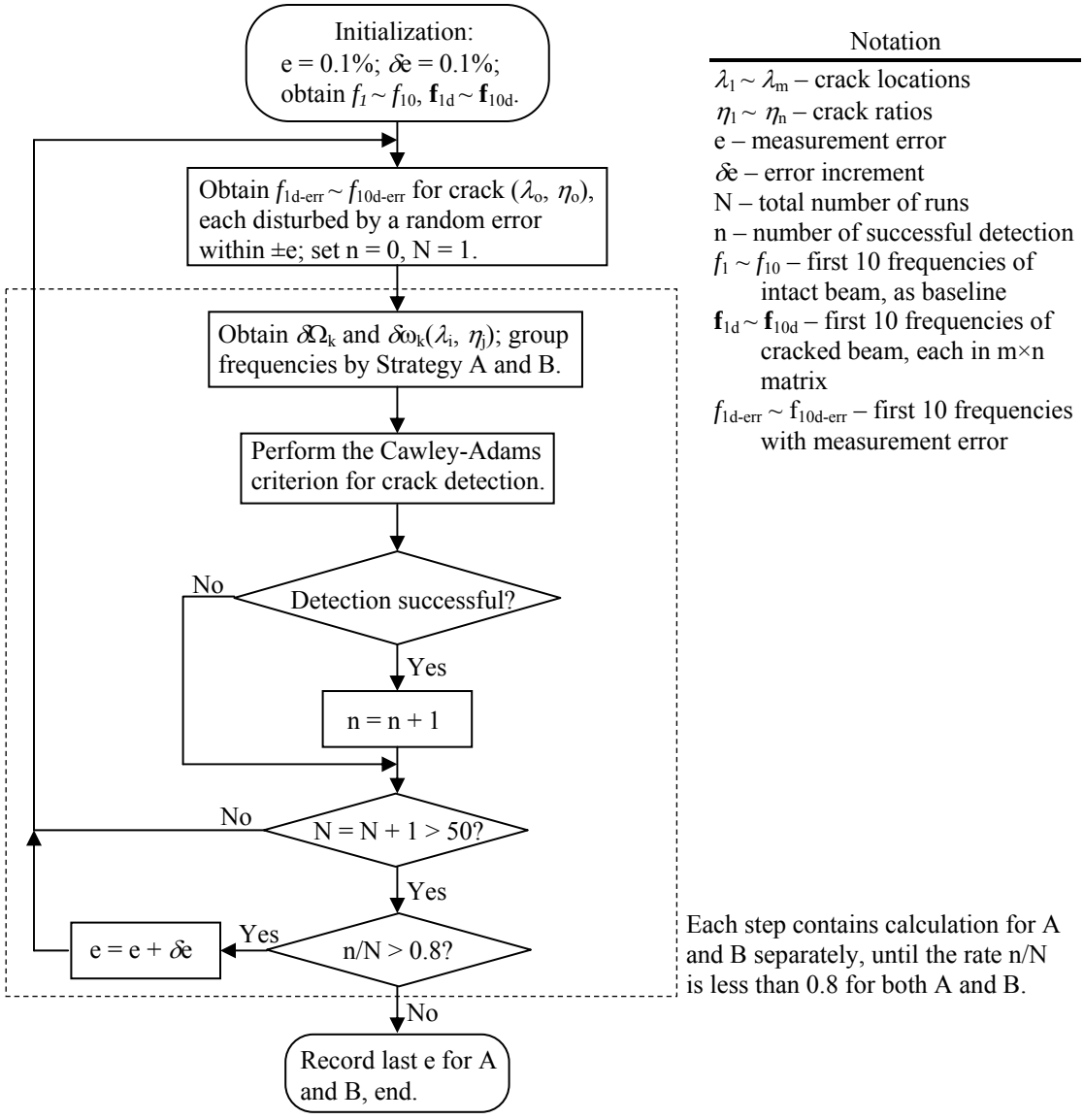

Figure 5.11 Flowchart of the numerical testing.

Since the crack location can be detected more accurately than the crack ratio, the testing is conducted with emphasis on an accurate determination of crack ratio for both strategies. For a crack located at λ_o with ratio η_o, detection is considered to be successful when more than 4 sets out of 9 sets indicate the crack at $\lambda_o \pm 0.05$ with the exact ratio η_o. The measurement error threshold is defined as the error by which 40 out of the 50 runs can successfully detect the crack. For various crack ratios and locations, the results are listed in Table 5.4.

Table 5.4 Measurement error threshold for strategy A and B, $\theta = 70°$

	$\eta = 0.1$				
%	$\lambda = 0.1 \pm 0.05$	0.3 ± 0.05	0.5 ± 0.05	0.7 ± 0.05	0.9 ± 0.05
A	0.1	≈ 0	≈ 0	≈ 0	≈ 0
B	0.2	0.2	0.1	0.2	≈ 0

	$\eta = 0.2$				
%	$\lambda = 0.1 \pm 0.05$	0.3 ± 0.05	0.5 ± 0.05	0.7 ± 0.05	0.9 ± 0.05
A	0.4	≈ 0	0.1	0.1	≈ 0
B	0.6	0.3	0.4	0.6	0.2

	$\eta = 0.3$				
%	$\lambda = 0.1 \pm 0.05$	0.3 ± 0.05	0.5 ± 0.05	0.7 ± 0.05	0.9 ± 0.05
A	0.5	0.1	0.4	0.6	≈ 0
B	1.2	1.8	1.1	2.1	0.5

	$\eta = 0.4$				
%	$\lambda = 0.1 \pm 0.05$	0.3 ± 0.05	0.5 ± 0.05	0.7 ± 0.05	0.9 ± 0.05
A	0.6	0.2	0.7	0.8	≈ 0
B	1.3	1.3	1.8	2.6	1.4

	$\eta = 0.5$				
%	$\lambda = 0.1 \pm 0.05$	0.3 ± 0.05	0.5 ± 0.05	0.7 ± 0.05	0.9 ± 0.05
A	0.7	0.3	0.8	0.9	0.1
B	1.3	2.1	2.8	2.7	2.5

It is obvious that Strategy B is more robust to measurement errors than Strategy A in this model-based crack detection. While larger measurement errors are allowed for larger cracks, the error threshold is not the same when the crack of the same size is located at

different locations. For instance, the crack close to the free end is relatively more difficult to detect, especially for Strategy A. It is reasonable since in that case the crack is located at a low stress area. When the crack ratio is less than 0.1, it is very difficult for both strategies to detect the crack accurately even in the presence of small measurement errors.

B) When the bending-Torsion coupling is weak (θ = 30°)

As addressed in Chapter 3, frequency reduction patterns are usually different when the bending-torsion coupling is strong (e.g., θ = 70°) or weak (e.g., θ = 30°). To further study the effect of fiber orientation, the same crack location and size are assumed, i.e., λ = 0.3 and η = 0.3. Table 5.5 lists the first ten natural frequencies of the beam before and after the damage. Similarly with 1% measurement errors, results by Strategy A and B are shown in Figures 5.12 – 19.

Table 5.5 The first ten natural frequencies, θ = 30°, without measurement errors

rad/s	1st	2nd	3rd	4th	5th	6th	7th	8th	9th	10th
f	42.37	265.52	554.59	743.40	1456.53	1663.86	2407.29	2773.25	3594.79	3883.13
f_d	39.03	259.77	531.15	683.31	1417.57	1661.62	2383.94	2692.07	3329.27	3695.83
f-f_d	3.34	5.75	23.44	60.09	38.96	2.24	23.35	81.18	265.52	187.30
(%)	(7.9)	(2.2)	(4.2)	(8.1)	(2.7)	(0.13)	(0.97)	(2.9)	(7.4)	(4.8)

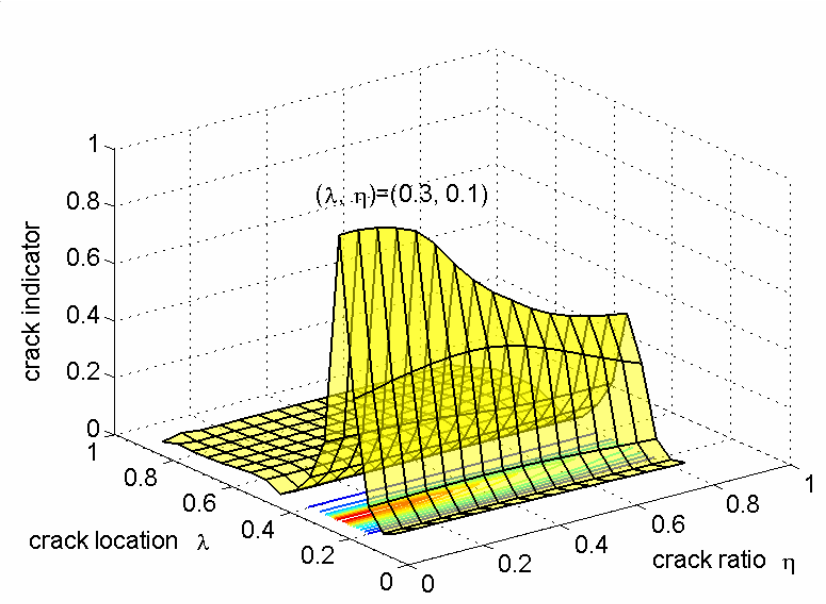

Figure 5.12 Crack detection by the first 4 frequencies, θ = 30°.

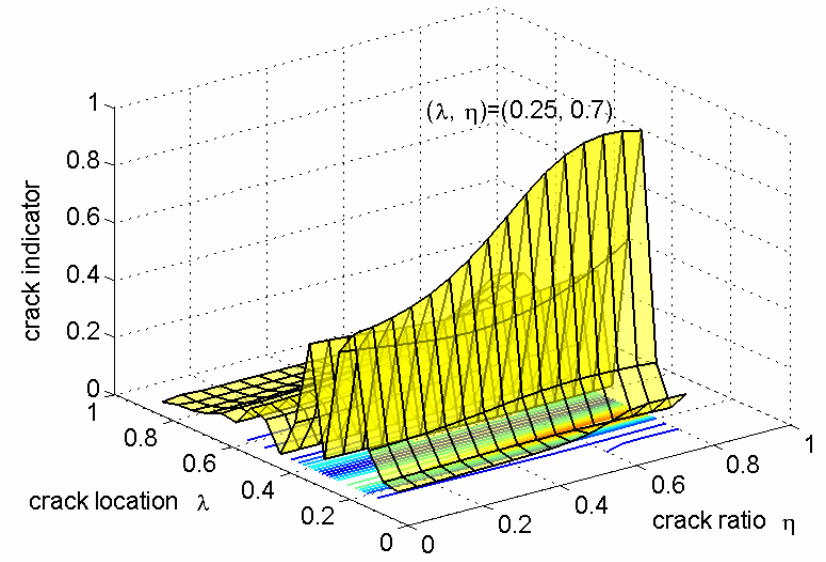

Figure 5.13 Crack detection by the first 6 frequencies, $\theta = 30°$.

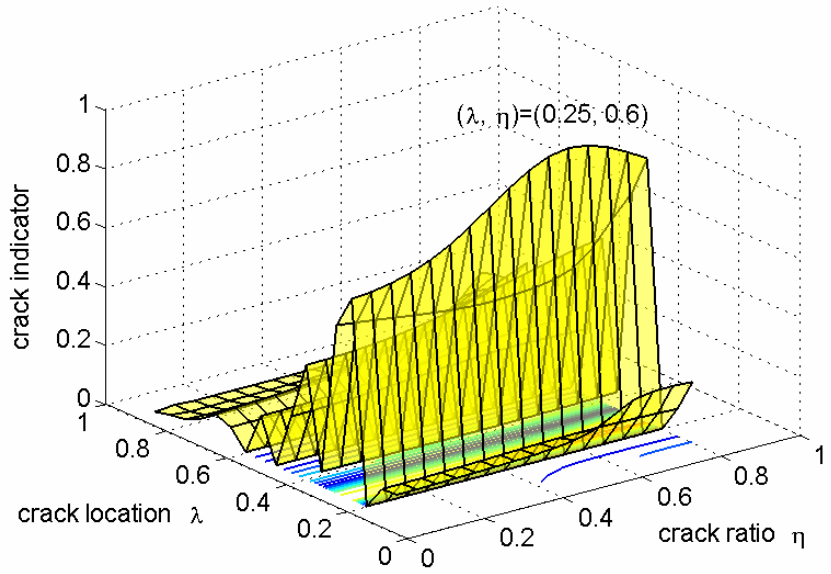

Figure 5.14 Crack detection by the first 8 frequencies, $\theta = 30°$.

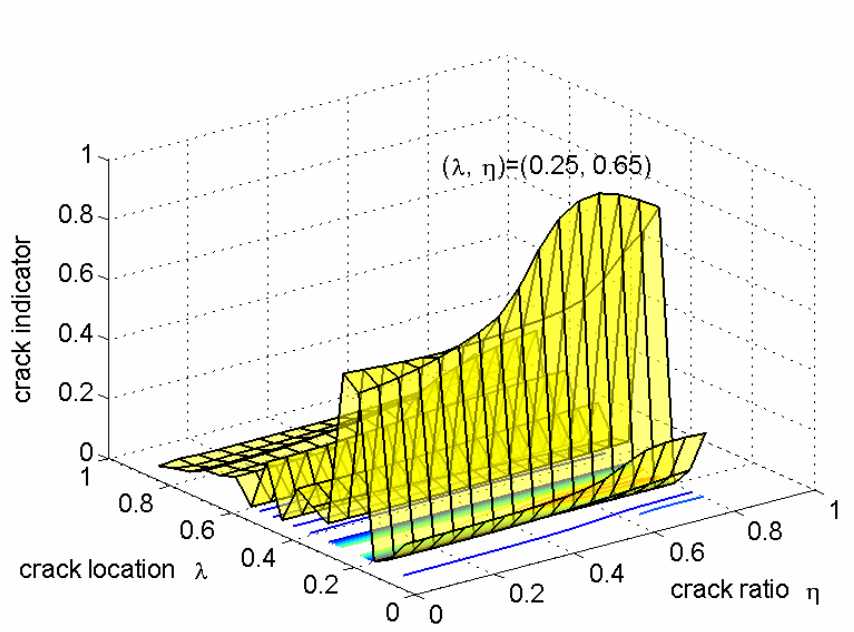

Figure 5.15 Crack detection by the first 10 frequencies, $\theta = 30°$.

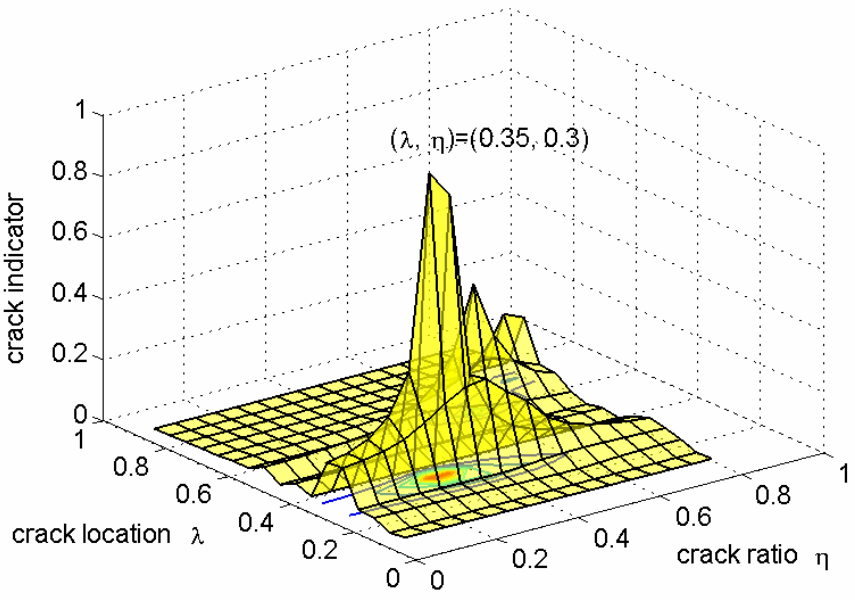

Figure 5.16 Crack detection by the first 4 re-ordered frequencies, $\theta = 30°$.

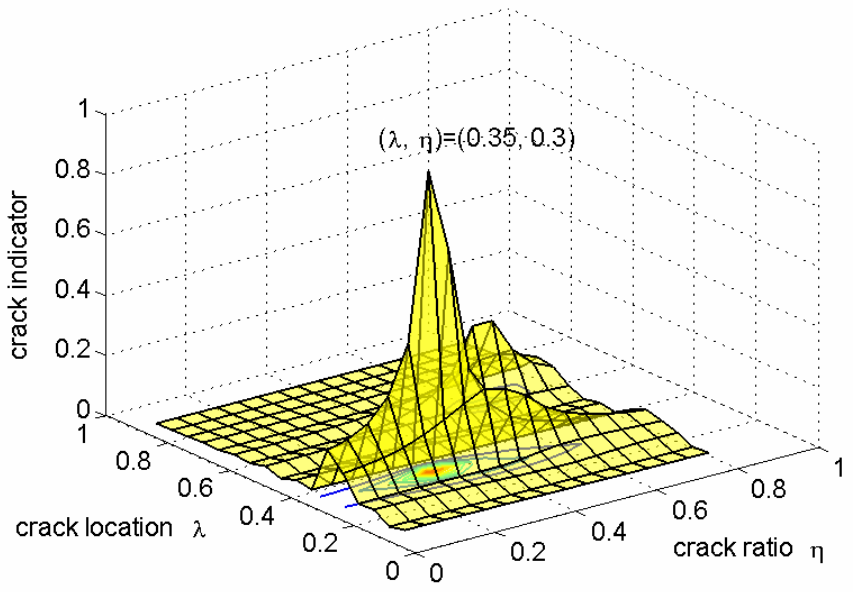

Figure 5.17 Crack detection by the first 5 re-ordered frequencies, $\theta = 30°$.

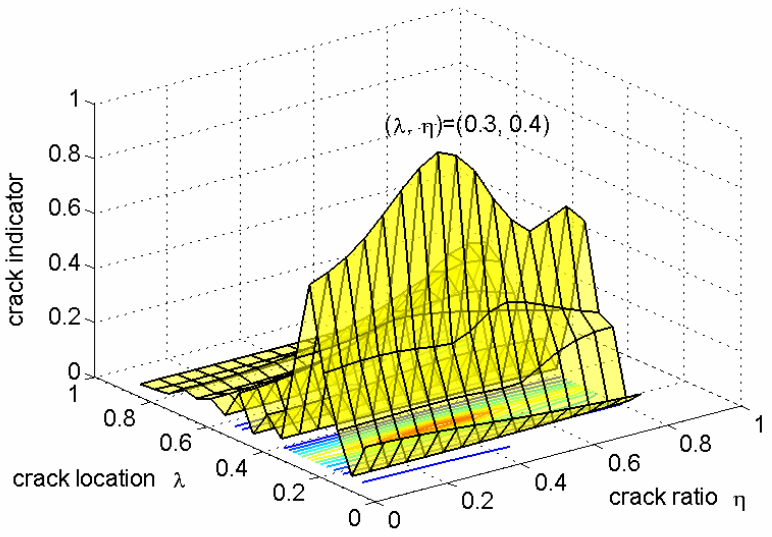

Figure 5.18 Crack detection by the first 6 re-ordered frequencies, $\theta = 30°$.

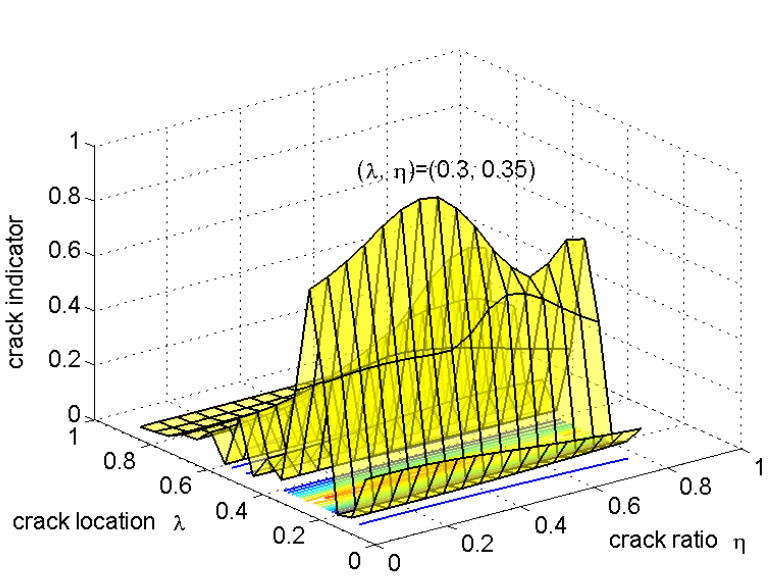

Figure 5.19 Crack detection by the first 7 re-ordered frequencies, $\theta = 30°$.

The same numerical testing is then run for various crack sizes and locations when the coupling is weak ($\theta = 30°$), and the results are listed in Table 5.6.

Table 5.6 Measurement error threshold for strategy A and B, $\theta = 30°$

	$\eta = 0.2$				
%	$\lambda = 0.1\pm0.05$	0.3±0.05	0.5±0.05	0.7±0.05	0.9±0.05
A	≈ 0	≈ 0	≈ 0	≈ 0	≈ 0
B	0.1	0.1	0.1	0.1	≈ 0

	$\eta = 0.3$				
%	$\lambda = 0.1\pm0.05$	0.3±0.05	0.5±0.05	0.7±0.05	0.9±0.05
A	≈ 0	0.2	0.1	≈ 0	≈ 0
B	0.2	0.4	0.3	0.4	0.3

	$\eta = 0.4$				
%	$\lambda = 0.1\pm0.05$	0.3±0.05	0.5±0.05	0.7±0.05	0.9±0.05
A	≈ 0	0.4	0.1	0.2	≈ 0
B	0.4	0.9	0.9	0.9	0.7

	$\eta = 0.5$				
%	$\lambda = 0.1\pm0.05$	0.3±0.05	0.5±0.05	0.7±0.05	0.9±0.05
A	0.1	0.5	0.2	0.6	0.1
B	0.6	1.5	1.7	1.5	1.2

For the crack with the same size and location, the measurement error thresholds are relatively smaller when the bending-torsion coupling is weak. Moreover, cracks with the ratio less than 0.2 are difficult to detect in the presence of measurement errors. A comparison of Table 5.1 with 5.5 indicates that when the coupling is weak, the span of percentage frequency reductions is much narrower than that when the coupling is strong. The different frequency reduction pattern along with the narrow span of percentage changes due to the fiber orientation does affect the accuracy of crack detection.

5.4 Summary

Crack detection (size and location) by changes in natural frequencies is presented in this chapter. The cracked beam model is used as the reference, and the size and location of the crack are determined by the Cawley-Adams criterion. If measurement errors are taken into account, it is demonstrated that increasing the number of frequencies for consideration does not necessarily improve the accuracy in crack detection. In fact, all frequencies are not equally significant in the sensitivity based approach. A new strategy in grouping frequencies is proposed by which the frequency with a larger percentage reduction has the priority to be selected. Numerical testing is conducted and the results indicate that the proposed strategy is less sensitive to measurement errors than the conventional idea by which the number of frequencies is increased by adding frequencies from the lowest to the highest order consecutively.

It is also demonstrated that both the size and location of the crack can be determined by the Cawley-Adams criterion within a certain level of measurement errors. It is more accurate to locate the crack than to determine the size. The smaller the crack size, the less the measurement errors that can be allowed to detect the crack accurately. The measurement error threshold is also affected by the crack location. Moreover, for the crack of the same size and at the same location, the threshold is smaller when the bending-torsion coupling is weak than that when the coupling is strong due to the fiber orientation. To accurately detect the crack on a composite beam with coupled bending-torsion modes, it is suggested that

allowable measurement errors be considered in conjunction with possible crack sizes and locations, as well as the situation whether the bending-torsion coupling is strong or weak.

Contribution

The following lists contributions to the literature on crack detection by changes in natural frequencies:

1) It is demonstrated that the model-based approach by using the Cawley-Adams criterion can be used to detect both the size and location of the crack on a composite beam. A new strategy is proposed in selecting natural frequencies for crack detection, which is much less sensitive to measurement errors than the conventional idea that frequencies are selected consecutively from the lowest order to the highest.
2) For a combination of different crack sizes and locations, measurement error thresholds are obtained by numerical testing. For the cracked composite beam, it is found that the threshold is affected not only by the crack size and location, but also by how strong the coupling between bending and torsion is due to the fiber orientation.

Chapter 6

Analysis of Model Parameter Uncertainties by Information-gap Theory

6.1 Introduction

The cracked composite beam model developed in Chapter 3 has not been verified or calibrated with experimental data. Although the analytical model may involve less systematic errors compared to numerical modeling, uncertainty in model parameters could result in erroneous prediction on various system outputs. The fact that some model parameters may not be measured directly and precisely in experiments introduces further difficulty in model verification and validation. On the other hand, with no experimental data available, uncertainties in model parameters can hardly be characterized by assuming some form of probability density functions. Under such circumstances, a methodology named information-gap decision theory (Ben-Haim, 2001), or info-gap theory in short, serves as a good alternative to model parameter uncertainties and their effects to system outputs. Info-gap theory is developed to model and manage severe uncertainties in system models for situations in which neither statistical methods nor fuzzy logic can be readily applied because of the large disparity between what is known and what could be known. In this chapter, the basic concept of info-gap modeling of parameter uncertainties is first explained briefly. A series of uncertain events are represented by a family of nested sets. Two immunity functions

– robustness and opportunity – are then constructed to account for two contrasting consequences of uncertainty. Parameters that may have uncertainties at higher levels are then discussed. While no restriction needs to be exerted in selection of performance parameters, natural frequencies are chosen to investigate the sensitivity of model prediction under various model parameter uncertainties.

6.2 Info-gap Modeling of Parameter Uncertainties

A structural model – either analytical or numerical – may be expressed symbolically as

$$\mathbf{y} = M(\mathbf{q}) \tag{6.1}$$

where M represents a mapping between the model performance or vector of output features $\mathbf{y}$ and the vector of model's decision parameters $\mathbf{q}$. In addition to model parameters, vector $\mathbf{q}$ may comprise other factors, such as design variables, constitutive laws, structure geometries and operational options. A model specified by $\mathbf{q}$ is usually considered to be validated if $\mathbf{q}$ is verified to be able to accurately represent the physical properties of the system throughout the design domain or operational space (Hemez and Ben-Haim, 2004). However in many cases, there exist a cluster of variables, denoted by vector $\mathbf{u}$, that are uncertain in the way that not only is information related to these variables fragmentary, but even the identity of some of them could be completely unknown or very difficult to characterize. It is therefore not uncommon that sometimes it is ambiguous to categorize a given variable to either vector $\mathbf{q}$ or $\mathbf{u}$. With both decision parameters and uncertain variables included, the model expressed by equation (6.1) becomes

$$\mathbf{y} = M(\mathbf{q};\mathbf{u}) \tag{6.2}$$

where the uncertain variables $\mathbf{u}$ possess characteristics that can not be represented by either probability density functions or fuzzy logic membership functions. However, an info-gap model (IGM), denoted by $U(\mathbf{u_n};\ \alpha)$ may be constructed such that $\mathbf{u} \in U(\mathbf{u_n};\ \alpha)$. Here the IGM U is simply a collection of nested sets. All sets are "centered" around the nominal values ($\mathbf{u_n}$) of corresponding uncertain variables, with the "size" determined by a uncertain level factor (α) which is a nonnegative real value. Therefore the set with a smaller value of α is completely contained in the set with a larger value of α, i.e., for $\alpha_1 < \alpha_2$, $U(\mathbf{u_n},\ \alpha_1) \subset U(\mathbf{u_n},\ \alpha_2)$.

Basically there is no restriction in formulating the IGM; the detailed format is typically case-dependent. For instance, if each uncertain variable has a lower bound and an upper bound, denoted by $\mathbf{u}^-$ and $\mathbf{u}^+$, respectively, the IGM may be expressed as

$$U(\mathbf{u}_\mathbf{n};\alpha) = \{\mathbf{u} \,|\, \alpha\mathbf{u}^- \le \mathbf{u} - \mathbf{u}_\mathbf{n} \le \alpha\mathbf{u}^+\}, \quad 0 \le \alpha \le 1 \tag{6.3}$$

The model's performance in the presence of uncertain model parameters can be evaluated in many different ways. One of the most widely used metrics is the correlation between test data and the model prediction. For instance, a correlation error function $R(\mathbf{q}; \mathbf{u})$, which is used to evaluate the magnitude of discrepancy between experiment data and the model prediction, may be defined as

$$R(\mathbf{q};\mathbf{u}) = [\mathbf{y}^{\mathbf{test}} - \mathbf{y}]^T \mathbf{W}[\mathbf{y}^{\mathbf{test}} - \mathbf{y}] \tag{6.4}$$

where $\mathbf{W}$ is a square weighting matrix. Hemez and Ben-Haim (2004) named this function as the fidelity function which depends on both the decision parameters and uncertain variables. It is simply a scalar performance function and directly related to the uncertain level factor α. Let R_c be the largest level of infidelity acceptable during the evaluation of the model's performance. Then the model is considered to be calibrated if

$$R(\mathbf{q};\mathbf{u}) \le R_c \tag{6.5}$$

There are two fundamental and unique functions in the implementation of info-gap decision theory for uncertainty analysis – robustness and opportunity functions. The robustness of decision $\mathbf{q}$ is the greatest level of uncertainty factor α at which the model performance is never worse than the critical value R_c. The robustness function $\hat{\alpha}$ can be formally defined as

$$\hat{\alpha}(\mathbf{q};R_c) = \max\left\{\alpha \,\middle|\, \alpha \ge 0, \max_{\mathbf{u}\in U(\mathbf{u}_\mathbf{n};\alpha)} R(\mathbf{q};\mathbf{u}) \le R_c\right\} \tag{6.6}$$

Since the robustness function reflects the degree of resistance to uncertainty, it addresses the detrimental facet of uncertainty and therefore a larger value of $\hat{\alpha}$ is desirable. On the other hand, the opportunity of decision $\mathbf{q}$ is the least level of uncertainty factor α at which the model performance can be – but not always – as good as a threshold value R_w. The opportunity function $\hat{\beta}$ can then be defined as

$$\hat{\beta}(\mathbf{q}; R_w) = \min\left\{\alpha \,\middle|\, \alpha \geq 0, \min_{\mathbf{u}\in U(\mathbf{u_n};\alpha)} R(\mathbf{q};\mathbf{u}) \leq R_w\right\} \tag{6.7}$$

The threshold R_w entails the possibility of an occasional reward. Due to the nature that the opportunity represents the least level of uncertainty that must be tolerated to ensure the possibility of an occasional reward as a result of decision **q**, a smaller value of $\hat{\beta}$ is desirable. Since a better performance is defined with a smaller value of R as in inequation (6.5), R_w is usually chosen such that it is much smaller than the critical value R_c, i.e., $R_w << R_c$. In contrary to the robustness function, the opportunity function addresses the beneficial aspect of uncertainty. Note that the above expressions about the performance, robustness and opportunity are presented to illustrate the basic concept of info-gap theory, and should not be considered to be unique. For instance, in some cases a larger performance value of R may be desirable rather than a smaller value, and the expressions for $\hat{\alpha}$ and $\hat{\beta}$ will change, respectively, to

$$\hat{\alpha}(\mathbf{q}; R_c) = \max\left\{\alpha \,\middle|\, \alpha \geq 0, \min_{\mathbf{u}\in U(\mathbf{u_n};\alpha)} R(\mathbf{q};\mathbf{u}) \geq R_c\right\} \tag{6.8.1}$$

$$\hat{\beta}(\mathbf{q}; R_w) = \min\left\{\alpha \,\middle|\, \alpha \geq 0, \max_{\mathbf{u}\in U(\mathbf{u_n};\alpha)} R(\mathbf{q};\mathbf{u}) \geq R_w\right\} \tag{6.8.2}$$

Accordingly R_w is chosen such that it is much larger than the critical value R_c, i.e., $R_w >> R_c$.

The following analysis is concerned with the former situation that a smaller value of R is preferred. Let R_n be the performance value corresponding to the nominal values, i.e., $\alpha = 0$ and $\mathbf{u} = U(\mathbf{u_n}, \alpha) = \mathbf{u_n}$. When the uncertainty level is increased from zero, a conceptual plot of α with respect to the performance level R is shown in Figure 6.1 for the robustness and opportunity functions. Given the uncertainty level, the opportunity curve is obtained by solving for the smallest performance value, while the robustness curve is obtained by solving for the largest performance value.

It is obvious that with the uncertainty level increased, the performance value is monotonously increasing on the robustness curve and on the other hand, monotonously decreasing on the opportunity curve. This is due to the fact that the IGM set with a smaller uncertainty level is completely included in the set with a larger uncertainty level. As

indicated by equation (6.6), the robustness of decision **q** for a larger critical value R_c can never be less than the one with smaller value of R_c. Likewise, by equation (6.7), if the threshold value R_w is reduced, the range of uncertainty must be increased in order to find a chance to ensure an occasional reward.

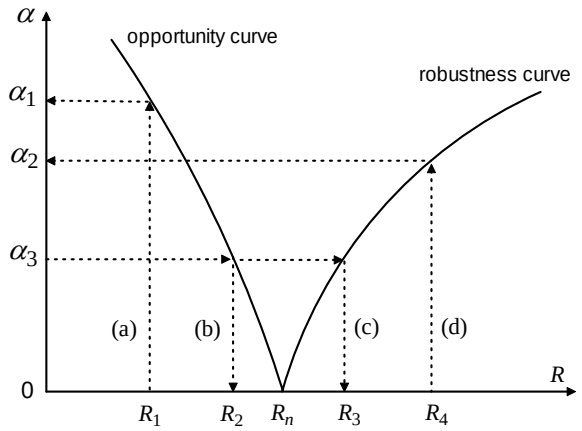

Figure 6.1 Conceptual illustration of info-gap robustness and opportunity curves.

In Figure 6.1, path (a) indicates that in order to find a chance to ensure an occasional reward of performance R_1, the uncertainty level needs to be as large as the value α_1. In other words, when the uncertainty level is less than α_1, it is impossible that the performance can reach the value R_1. On the other hand, path (d) indicates that if the critical performance value is required to be R_4, it is guaranteed only when the uncertainty level is less than the value α_2. Path (b) and (c) simply shows that at the uncertainty level α_3, all performance values are always in the range between R_2 and R_3. Moreover, the starting point of the performance, R_n, is determined by the nominal values. If all uncertain parameters have lower and upper bounds, the slope of the robustness and opportunity curves for an individual uncertain parameter may be affected by its corresponding bounds. Since changing the lower and upper bounds of an uncertain parameter affects only the domain of the largest IGM set of that parameter, at the same uncertain level the actual "size" of the IGM set varies so that the slope of both curves may change accordingly. When the performance is designated as the correlation between the model prediction and experimental data, the desirable situation is that the opportunity curve is very "flat" while the robustness curve is very "steep."

6.3 Uncertainties in Model Parameters

Model parameters selected for uncertainty analysis are usually those that may be hardly determined at a high level of accuracy by experimental measurement. When an experiment is conducted to verify the cracked composite model, some influences not included in the model may also affect the test-analysis correlation. For instance, the discrepancy could come from the added mass of an actuator/sensor (e.g., PZT patches) and the local stiffness changes, unless these external effects are taken into account by additional models. Assumptions in the modeling, such as the one-dimensional beam, LEFM and classical lamination theory, may also contribute to the correlation error. These "systematic" errors may be differentiated from the modeling errors if a composite beam without any cracks is tested first to verify as well as calibrate the intact beam model.

The following three tables list model parameters of the cracked composite beam, out of which some parameters may have more uncertainties than others. In particular, stiffness parameters may not be measured accurately in an experiment. The coupling term K can not be measured directly and may be subject to larger uncertainty.

Table 6.1 Material properties of each ply (subscript *m* stands for matrix and *f* for fiber)

Symbol	Definition	unit
E_m, E_f	Modulus of elasticity	GPa
ν_m, ν_f	Poisson's ratio	-
G_m, G_f	Modulus of rigidity	Gpa
ρ_m, ρ_f	Mass density	kg/m^3
V	Fiber volume fraction	-
θ	Fiber angle	degree

Table 6.2 Beam geometry

Symbol	Definition	unit
b	Beam width	m
t	Beam thickness	m
L	Beam length	m
l	Crack location	m
a	Crack depth	m

Table 6.3 Other parameters of the beam model

Symbol	Definition	unit	Function of
EI	Bending stiffness parameter	$N{\cdot}m^2$	E, G, ν, V, θ, b and t
GJ	Torsional stiffness parameter	$N{\cdot}m^2$	E, G, ν, V, θ, b and t
K	Coupling parameter	$N{\cdot}m^2$	E, G, ν, V, θ, b and t
m	Mass/length	kg/m	ρ, b and t
I_α	Polar mass moment of inertia/length	kg·m	ρ, b and t
c_{22}	Transverse flexibility at crack location	m/N	E, G, ν, V, t, a and b
c_{44}	Bending flexibility at crack location	1/(N·m)	E, G, ν, V, θ, t, a and b
c_{66}	Torsional flexibility at crack location	1/(N·m)	E, G, ν, V, t, a and b
c_{26}	Flexibility coupling at crack location	1/N	E, G, ν, V, t, a and b

Compared to other parameters, the stiffness parameters (EI and GJ) and the coupling term (K) may experience more uncertainty for the aforementioned reasons. It is also of interest to know the effects of uncertainties in crack location (λ) and ratio (η). In the following analysis the five parameters – EI, GJ, K, λ and η – are selected with uncertainties characterized by info-gap models, i.e., $\mathbf{u} = [u_i] = [EI \;\; GJ \;\; K \;\; \lambda \;\; \eta]$, $i = 1, 2, 3, 4, 5$.

6.4 Frequency Sensitivity to Model Parameter Uncertainties

Since natural frequencies of the cracked beam are relatively easier to measure in an experiment, the first four natural frequencies are selected as the system outputs. It has been shown in the last three chapters that a certain system output may exhibit different patterns with changes in fiber orientation, e.g., frequency patterns with the same crack are different when the bending-torsion coupling is strong or weak. The two situations in terms of fiber angles (70° or 30°) are again considered.

The same geometry as in Chapter 3 is assumed for the cracked beam. To simulate experimental data, natural frequencies obtained from the model for fiber volume fraction V = 0.5, crack location λ = 0.3 and crack ratio η = 0.3 are used as reference data. The info-gap modeling requires a nominal value for each uncertain parameter; the assumed nominal values along with the references are listed in Table 6.4 and 6.5.

Table 6.4 Reference and nominal values of uncertain parameters, $\theta = 70°$

unit	N·m^2	N·m^2	N·m^2	-	-
reference	EI = 89.5	GJ = 58.8	K = 61.3	λ = 0.3	η = 0.3
nominal	u_{1n} = 80.5	u_{2n} = 50.0	u_{3n} = 55.2	u_{4n} = 0.315	u_{5n} = 0.27

Table 6.5 Reference and nominal values of uncertain parameters, $\theta = 30°$

unit	N·m^2	N·m^2	N·m^2	-	-
reference	EI = 8.0	GJ = 22.8	K = 0.74	λ = 0.3	η = 0.3
nominal	u_{1n} = 7.2	u_{2n} = 19.4	u_{3n} = 0.67	u_{4n} = 0.315	u_{5n} = 0.27

The IGM of uncertain parameters is defined by

$$U(\mathbf{u_n};\alpha) = \{\mathbf{u} \,|\, |\mathbf{u} - \mathbf{u_n}| \leq \alpha \mathbf{u_n}\},\ \alpha \geq 0 \tag{6.9}$$

where $\mathbf{u_n} = [u_{1n}\ \ u_{2n}\ \ u_{3n}\ \ u_{4n}\ \ u_{5n}]$ and α is the uncertainty level. The model performance R is defined by

$$R_{ij}(\mathbf{q};u_j) = | y_{ij} - y_i^r | / y_i^r,\ \ i = 1,...,4;\ j = 1,...5 \tag{6.10}$$

where y_i^r is the i^{th} reference frequency and y_{ij} the i^{th} frequency as a result of uncertainty in model parameter u_j. Parameters such as the beam geometry and material properties of selected prepregs may be included in the decision vector **q** which should be decided before conducting an actual experiment. For comparison purposes, model performance is evaluated for uncertain parameters individually. When one parameter experiences uncertainty, all other parameters are set at the nominal values. With the uncertainty level increased from zero, opportunity and robustness curves for a single performance factor start from the same point so that the rate of change of each uncertain parameter can be compared on a single plot. Note that if the reference frequencies are obtained by experiment, the model performance becomes the test-analysis correlation. However, since the reference used here is directly obtained from the model, the performance evaluated is actually the sensitivity of natural frequencies to model parameter uncertainties.

Based on the implementation of info-gap theory, the following opportunity curves are obtained by solving the best performance at different uncertainty levels, while the robustness curves are obtained by solving the worst performance at the same uncertainty level.

A) When the bending-Torsion coupling is strong ($\theta = 70°$)

Frequency sensitivities are shown in Figures 6.2 – 6.5.

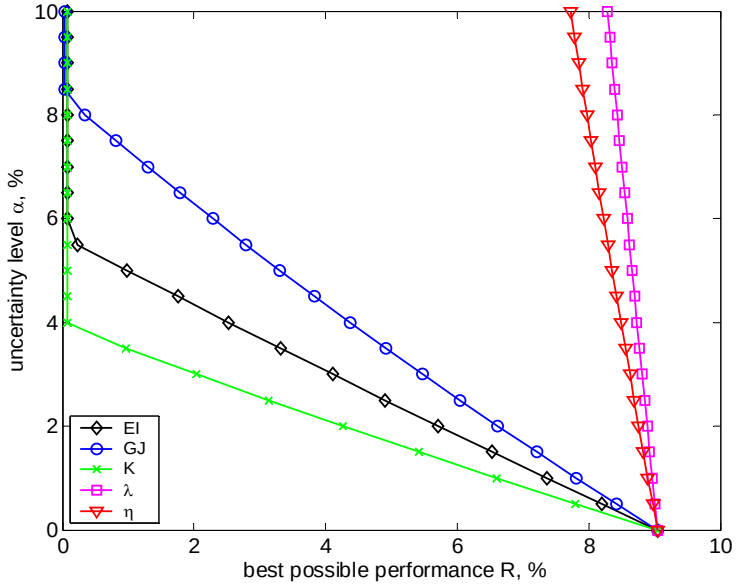

(a) Opportunity curves

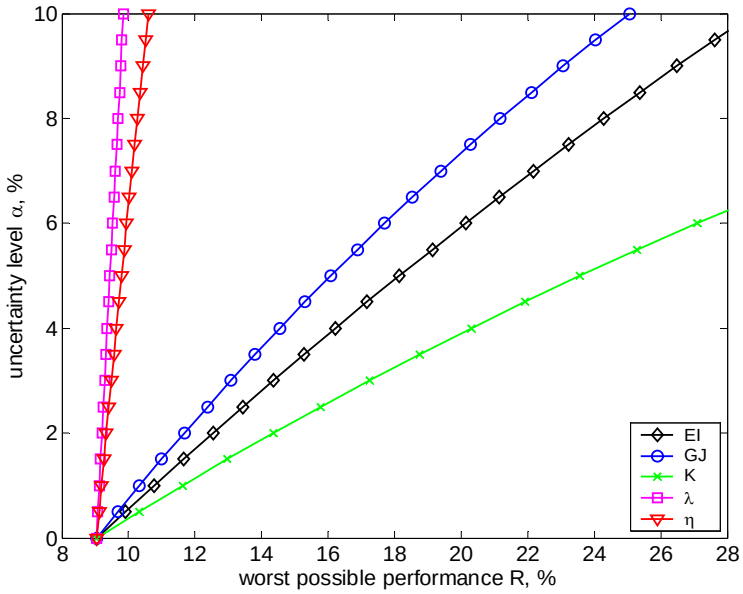

(b) Robustness curves

Figure 6.2 Sensitivity of the first natural frequency, $\theta = 70°$.

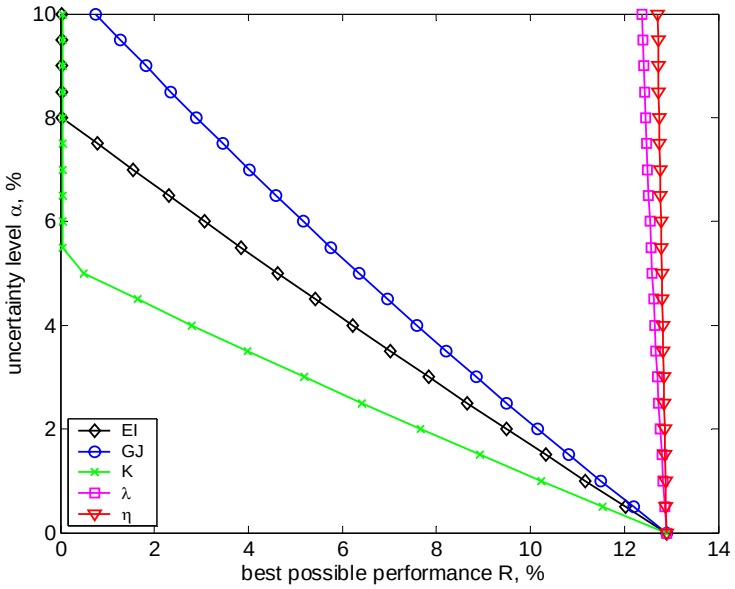

(a) Opportunity curves

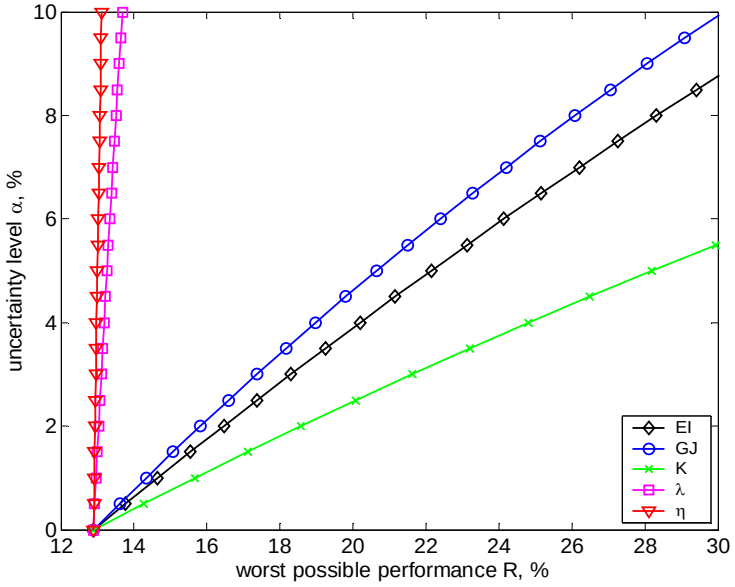

(b) Robustness curves

Figure 6.3 Sensitivity of the second natural frequency, $\theta = 70°$.

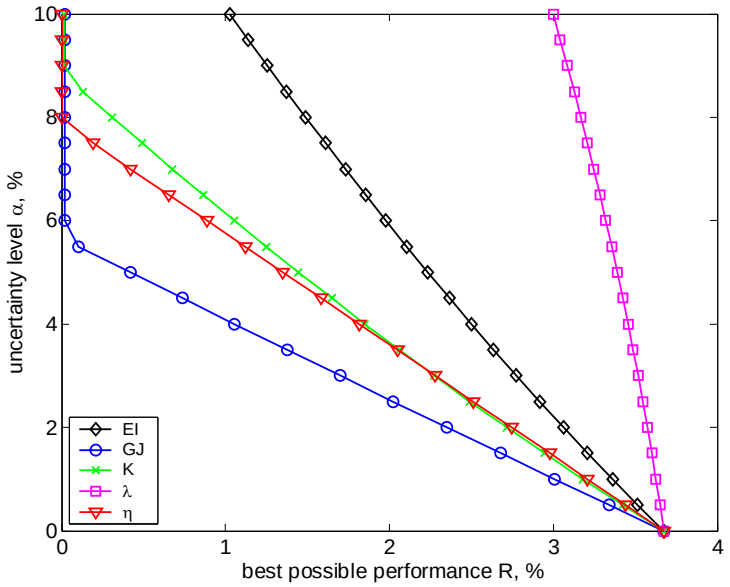

(a) Opportunity curves

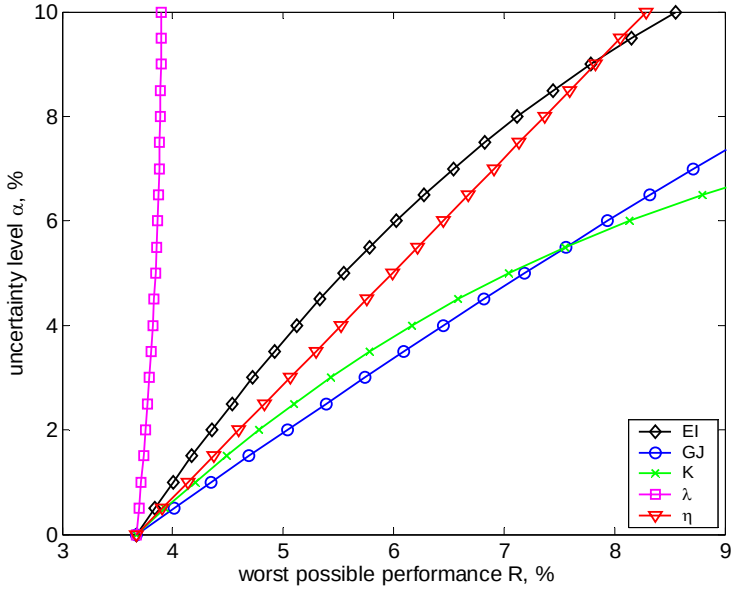

(b) Robustness curves

Figure 6.4 Sensitivity of the third natural frequency, $\theta = 70°$.

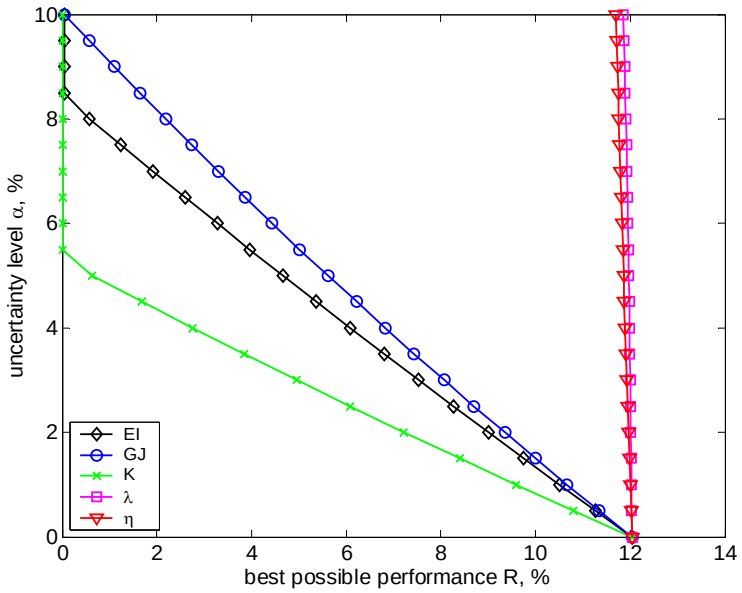

(a) Opportunity curves

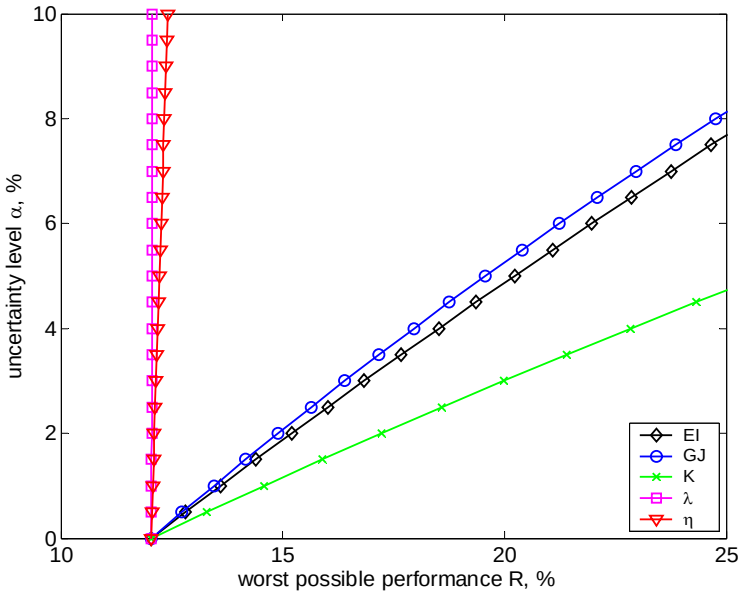

(b) Robustness curves

Figure 6.5 Sensitivity of the fourth natural frequency, $\theta = 70°$.

B) When the bending-Torsion coupling is weak ($\theta = 30°$)

Frequency sensitivities are shown in Figures 6.6 – 6.9.

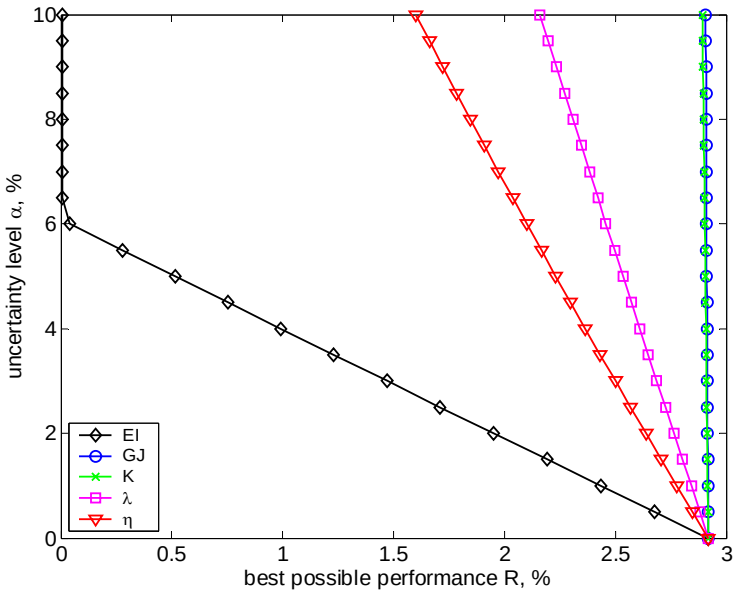

(a) Opportunity curves

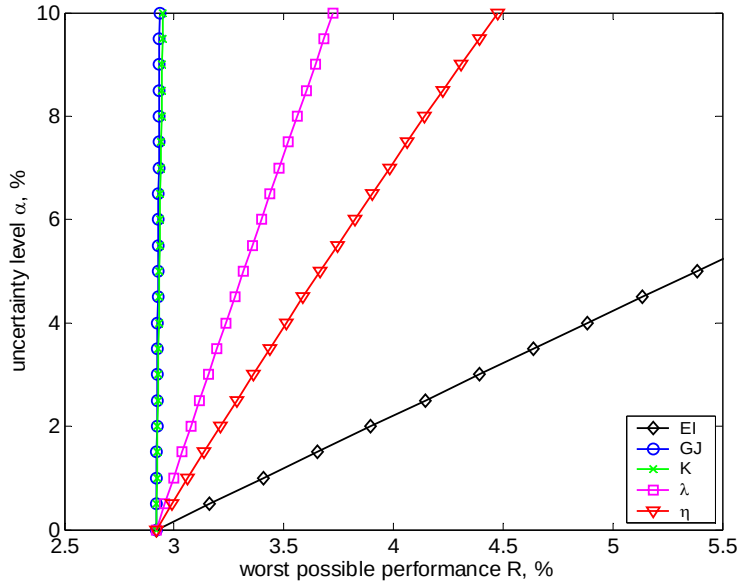

(b) Robustness curves

Figure 6.6 Sensitivity of the first natural frequency, $\theta = 30°$.

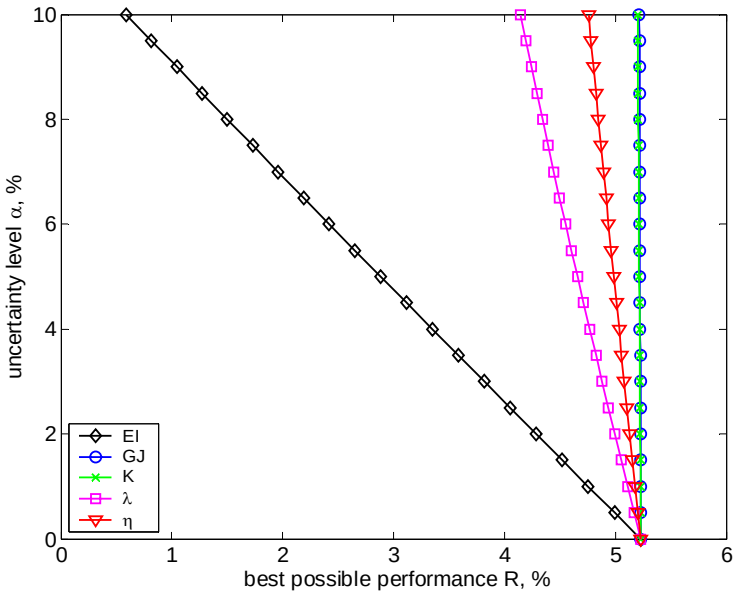

(a) Opportunity curves

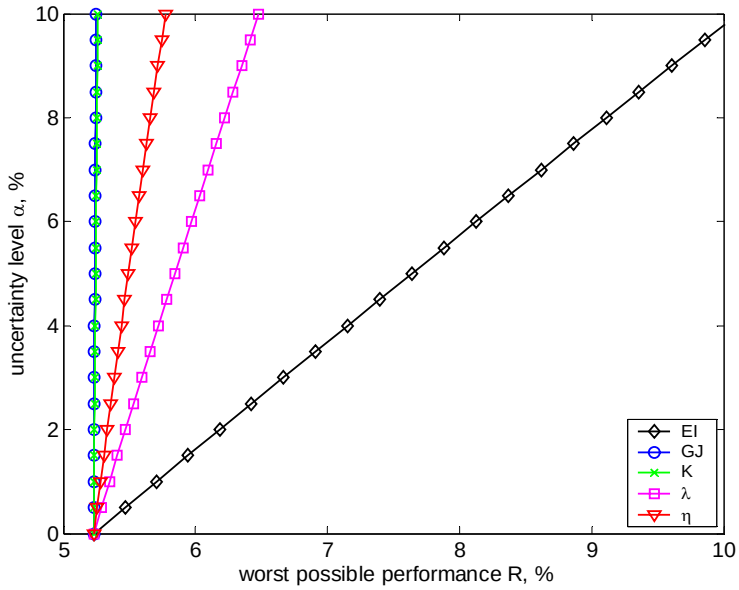

(b) Robustness curves

Figure 6.7 Sensitivity of the second natural frequency, $\theta = 30°$.

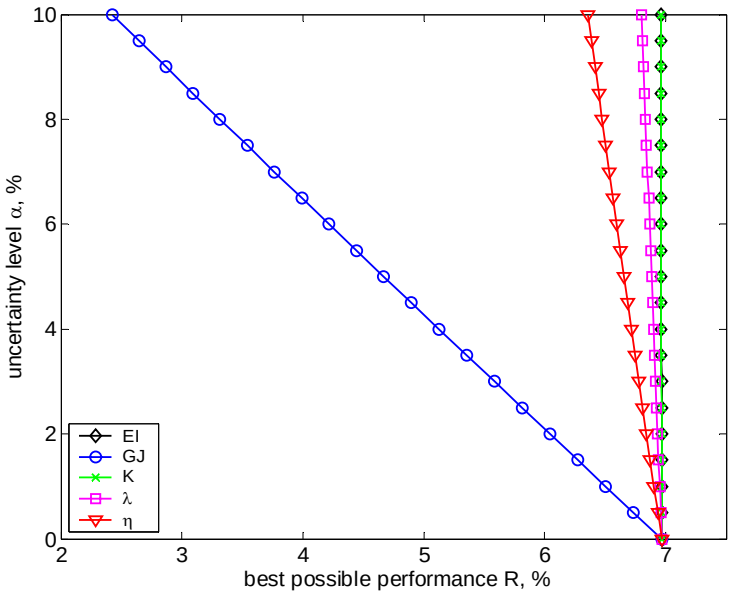

(a) Opportunity curves

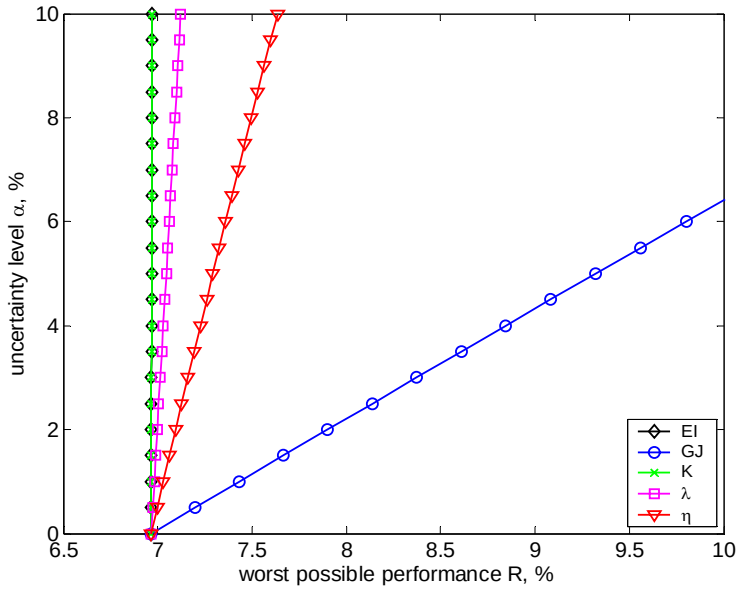

(b) Robustness curves

Figure 6.8 Sensitivity of the third natural frequency, $\theta = 30°$.

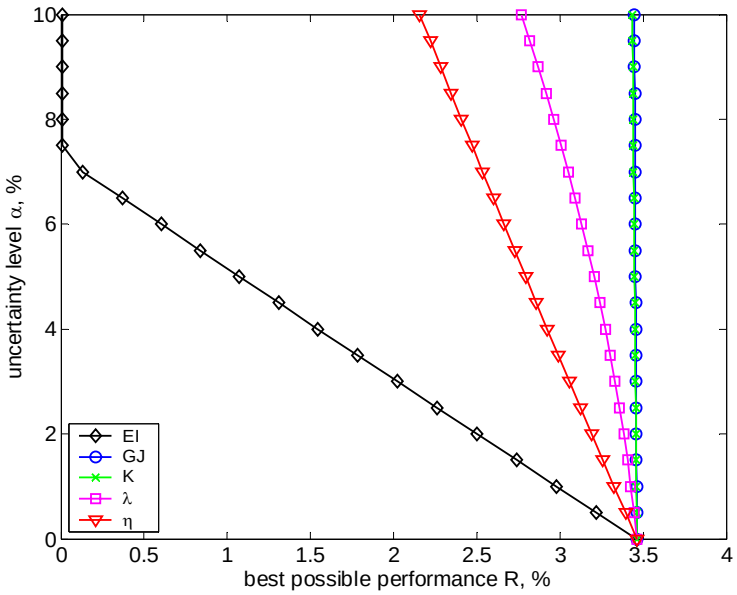

(a) Opportunity curves

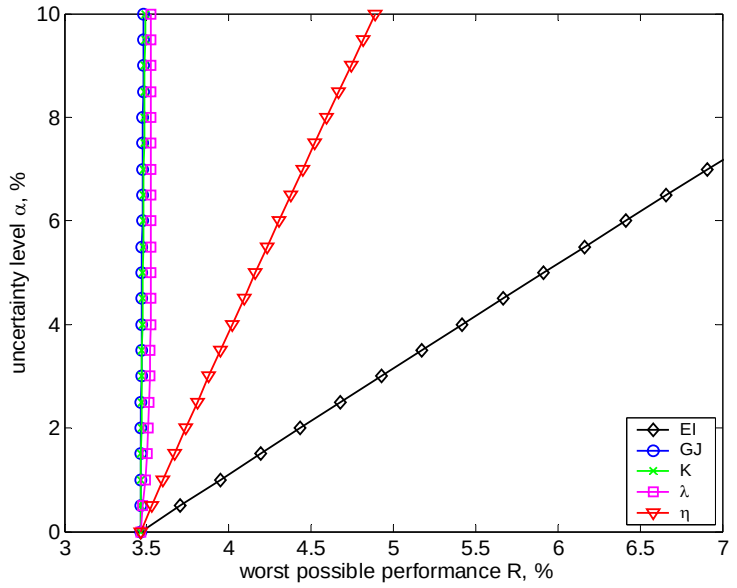

(b) Robustness curves

Figure 6.9 Sensitivity of the fourth natural frequency, $\theta = 30°$.

The reference frequencies are obtained when all uncertain parameters take their reference values such that $\mathbf{y}^r$ = [67.9 441.5 665.2 1143.8] rad/s for $\theta = 70°$ and $\mathbf{y}^r$ = [39.0

259.8 531.1 683.3] rad/s for $\theta = 30°$. Determination of either the opportunity or robustness curve starts from the uncertainty level at zero, and the procedure is same for each uncertain parameter. For instance, with no uncertainty in each parameter, i.e., the uncertain level $\alpha = 0$, all parameters have their nominal values given in Table 6.4 for $\theta = 70°$. The first four natural frequencies predicted by the model are $\mathbf{y}_n$ = [61.8 384.6 640.7 1006.2] where n refers to the nominal value. Therefore, when the uncertain level is zero, the performance denoted by $\mathbf{R}_n$ becomes

$$\mathbf{R}_n = \{R_{in}(\mathbf{q};\mathbf{u})\} = \{|\, y_i - y_i^r \,| / y_i^r\} = \begin{bmatrix} 9.0\% & 12.9\% & 3.7\% & 12.0\% \end{bmatrix} \tag{6.11}$$

Note that these percentage values are the starting points of opportunity and robustness curves shown in Figures 6.2 to 6.5. Next, consider only the sensitivity of the first natural frequency due to the uncertainty in the first parameter u_1 (i.e., *EI*), as illustrated in Figure 6.2. While other uncertain parameters still take their nominal values, the first parameter u_1 is now subject to some uncertainty governed by the IGM as defined in equation (6.10):

$$u_1 \in U(u_1;\alpha)\text{, or } (1-\alpha)u_{1n} \le u_1 \le (1+\alpha)u_{1n} \tag{6.12}$$

which means u_1 may take any value within this range confined by its nominal value u_{1n} and the uncertainty level α. The model performance defined by equation (6.10) in terms of the sensitivity of the first natural frequency in the presence of uncertainty in parameter u_1 becomes

$$R_{11}(\mathbf{q};u_1) = |\, y_{11} - y_1^r \,| / y_1^r \tag{6.13}$$

where y_{11} (the first natural frequency) is a function of u_1 and so is the performance R_{11}. With the uncertainty level α set at a specific value, solving the model for y_{11} will yield a minimum and maximum value of R_{11}, since u_1 is varying in the range defined by (6.12). The minimum value of R_{11} corresponds to the point on the opportunity curve of *EI* in Figure 6.2(a), while the maximum value corresponds to the point on the robustness curve of *EI* in Figure 6.2(b).

When the bending-torsion coupling is strong, uncertainty in the coupling term *K* affects the first, second and fourth natural frequencies the most, followed by the stiffness parameters *EI* and *GJ*. However, the third natural frequency is more sensitive to uncertainty in the torsional stiffness parameter. At a specific uncertainty level, the parameter that has the best chance for an occasional reward likely brings the worst performance. Therefore there is a

trade-off in deciding the acceptable uncertainty level for any parameters. The observation could be of great value to guide the crack detection by changes in natural frequencies, considering the results presented in Chapter 5 that some frequencies are more important than others measured by their percentage changes. For instance, more attention should be paid to uncertainties in the torsional stiffness parameter if the third natural frequency is more significant than the first two in crack detection.

When the bending-torsion coupling is weak, uncertainty in the coupling term K affects the frequency sensitivities much less than the two stiffness parameters. In fact, the coupling term has a much smaller nominal value compared to either EI or GJ, as indicated by Table 6.5. Since the uncertainty is measured by the percentage of a nominal value, the same amount of percentage results in a small change in magnitude for K, and hence the uncertainty has an insignificant effect on the model performance. Except for the third natural frequency which is more sensitive to GJ, the bending stiffness parameter EI affects the other three frequencies more significantly in the same way as the coupling term K in the case of strong bending-torsion coupling.

Compared to uncertainties in EI, GJ and K, the same percentage of disturbance in crack location and ratio does not affect the performance much. In most cases, natural frequencies are relatively more sensitive to uncertainties in crack ratio than those in crack location.

6.5 Summary

In this chapter, sensitivity of natural frequencies to uncertainty in model parameters is investigated. Uncertainties are modeled by info-gap theory and the info-gap models are represented with a series of nested sets. With reference frequencies obtained from the cracked beam model, the frequency sensitivities to uncertainties in five model parameters are compared in terms of two immunity functions – opportunity and robustness functions. When the bending-torsion coupling is strong due to the fiber orientation, the first, second and fourth natural frequencies are more sensitive to uncertainties in the coupling term K, while the third natural frequency is more sensitive to uncertainty in the torsional stiffness parameter GJ. On

the other hand, when the bending-torsion coupling is weak, the same group of frequencies is more sensitive to uncertainties in the bending stiffness parameter *EI*, while the third frequency is more sensitive to uncertainties in the torsional stiffness parameter *GJ*. At a fixed uncertainty level, the parameter that is more robust in model performance is also the one that has less chance to bring the best possible performance, and vice versa.

The sensitivity of natural frequencies to model parameter uncertainties is important to the model-based crack detection presented in Chapter 5. Since each natural frequency is not equally significant in crack detection as addressed in Chapter 5, the sensitivity analysis presented in this chapter provides a guideline to allocate the importance level among different model parameters, so that more attention can be paid to the parameter whose uncertainty affects the significant natural frequency more than uncertainties in the other parameters.

Contribution

The following lists contributions to the literature on the analysis of model parameter uncertainties:

1) Info-gap decision theory is implemented to investigate parameter uncertainties of the cracked composite beam model.
2) Model performance in terms of natural frequency sensitivities is evaluated as well as compared for several uncertain parameters, considering the situation that the bending-torsion coupling is strong or weak. The analysis provides guidance to crack detection by changes in natural frequencies.

Chapter 7

Conclusions and Future Work

7.1 Conclusions and Contributions

This research was first motivated by cracking failure of composite wings in some unmanned aerial vehicles (UAVs). A crack on the composite wing changes the local stiffness, causes stress concentration around the crack front, affects structural dynamics, and influences the wing's aeroelastic instabilities. Many UAVs fly at a relatively low speed with unswept composite wings of large aspect ratio. To this end, this research models cracked composite wings with a composite beam of large aspect ratio that has an edge crack and vibrates in coupled bending and torsional modes, either due to the material properties, due to the crack, or both. Moreover, cracked beams made of isotropic materials have been extensively studied in the structural health monitoring (SHM) community during the last few decades; cracked composite beams vibrating in bending mode only were also studied by several researchers. This research introduces to the SHM community a new analytical model of cracked composite beams in which bending and torsional modes are coupled, providing modal analysis of the cracked beam, and presenting an enhanced crack detection strategy using changes in natural frequencies.

The first part of this dissertation addresses modeling of a surface crack, and analyzes vibration characteristics of a cracked composite beam that consists of several fiber-reinforced plies with all fibers orientated in the same direction. The local flexibility approach based on

linear fracture mechanics is used to model the crack and a local compliance matrix at the crack location is derived. Changes in natural frequencies and mode shapes of the cracked beam in clamped-free boundary conditions are investigated. The spectrum of the natural frequency reduction, along with observations on the mode shape changes indicated by this model, may be used to detect both the crack location and its magnitude for on-line structural health monitoring. Detailed observations include:

1) The dimensionless coefficients of the flexibility matrix exhibit double symmetry with respect to the fiber angle and fiber volume fraction.
2) The decrease of natural frequencies depends not only on the crack location and its magnitude, but also on the material properties. However, for a cracked composite beam with coupled bending-torsion, the largest frequency reduction no longer coincides with the case that crack is located at either the largest bending or torsion curvatures.
3) Frequency variation with respect to either the crack ratio or its location usually experiences a different pattern when the bending-torsion coupling is “strong” or “weak.” The variation previously controlled mainly by the bending mode can be controlled by the torsional mode with a change of fiber orientation, and vice versa.
4) When the fiber angle is 0 or ±90°, bending and torsion are essentially decoupled if there is no crack. The edge crack introduces coupling to the initially uncoupled bending and torsion. The pattern of frequency variation is predominantly controlled by either bending or torsional mode, but not both.

Next, the aeroelastic characteristics of an unswept composite wing with an edge crack are investigated. The cracked composite wing is modeled by a cracked composite cantilever with inertia coupling terms included in the model. The governing equation of the cracked wing is then different from that of the cracked composite beam in which no inertia coupling is involved, although the additional boundary conditions at the crack location do not change in either case. An approximate solution on critical flutter and divergence speeds is obtained by Galerkin’s method in which the fundamental mode shapes of the cracked wing model in free vibration are used. The mode shapes satisfy all boundary conditions including those at

the crack location and thus carry most of the information of the cracked wing. Both steady and quasi-steady aerodynamic forces are considered in the analysis. Compared to that of an isotropic wing, the anisotropy of a composite wing introduces many completely different phenomena in aeroelastic instabilities. Some observations include:

1) The critical divergence/flutter speed is affected by the elastic axis location, the inertia axis location, fiber angles, and the crack ratio and location. Considering that the elastic axis is fixed in the leading half chord with the inertia axis aft, the divergence/flutter speed is more sensitive to the stiffness orientation than to the crack itself.
2) The presence of a crack does not necessarily decrease the flutter or divergence speed of a composite wing. The flutter speed tends to increase as the crack ratio increases at certain fiber angles. However, in most situations the flutter speed decreases with increasing crack ratio, especially for that predicted by the quasi-steady aerodynamic model. The rate of change is higher with smaller fiber angles. As to a crack of fixed magnitude, the lowest flutter speed is observed when the crack approaches the root of the composite wing with smaller fiber angles.
3) Although both the flutter and divergence speeds experience variation with different crack locations, the magnitude of variation with respect to the crack location is relatively small, compared to the variation with the crack ratio.

Moreover, model-based crack detection (size and location) by changes in natural frequencies is addressed. The cracked beam model developed in Chapter 3 is used as the reference, and the size and location of the crack are determined by the Cawley-Adams criterion. With measurement errors considered, it is demonstrated that increasing the number of frequencies in the algorithm does not necessarily improve the accuracy in crack detection. In other words, all frequencies are not equally significant in the sensitivity based approach. A new strategy in grouping frequencies is then proposed such that the frequency with a larger percentage reduction has the higher selection priority. Numerical testing is conducted and the results indicate that the proposed strategy is less sensitive to measurement errors than the conventional approach of consecutively increasing the number of frequencies from the

lowest to the highest order. It is also demonstrated that both the size and location of the crack can be determined by the Cawley-Adams criterion in the presence of measurement errors. It is relatively more accurate to locate the crack than to determine the size. The numerical testing also indicates that the measurement error threshold – the maximum percentage error allowed for accurate crack detection – is affected by the crack location and its size, as well as the fiber orientation.

Finally, sensitivity of natural frequencies to model parameter uncertainties is investigated. Uncertainties are modeled by info-gap theory. In particular the info-gap models are represented with a collection of nested sets. With reference frequencies obtained from the cracked beam model, the frequency sensitivities to uncertainties in five model parameters are compared in terms of two immunity functions – opportunity and robustness functions. At a certain range of fiber orientation resulting in a “strong” bending-torsion coupling, the first, second and fourth natural frequencies are more sensitive to uncertainties in the coupling term, while the third natural frequency is more sensitive to uncertainty in the torsional stiffness parameter. On the other hand, when the bending-torsion coupling is “weak” due to a change of fiber orientation, the same group of frequencies is more sensitive to uncertainties in the bending stiffness parameter, while the third frequency is more sensitive to uncertainties in the torsional stiffness parameter. At a specific uncertainty level, the parameter that is more robust in model performance is likely the one that has less chance to bring the best possible performance, and vice versa.

Contributions to the literature

The following lists contributions of this research to the literature on vibration analysis of cracked composite beams, aeroelastic analysis of composite wings with an open crack, crack detection on composite beams by changes in natural frequencies, and analysis of model parameter uncertainties:

- An analytical model of cracked composite beams vibrating in coupled bending and torsion is developed. The model developed here is new, and no analytical model of cracked composite beams vibrating in coupled bending-torsion exists in the

literature prior to this research. The effects of the crack in conjunction of the material anisotropy to the modal parameters are investigated. Modal characteristics of a cracked composite cantilever beam are illustrated.

- The local flexibility concept is extended in the cracked composite beam model. One new coefficient (tearing mode by torsional moment) in the local flexibility matrix is calculated from linear fracture mechanics and classical theory of elasticity. The final 3×3 flexibility matrix is obtained including the bending-torsion coupling term in the off-diagonal position. The local flexibility matrix given in this dissertation can be easily applied to a composite bending-torsion beam with multiple cracks.
- An analytical model of cracked composite wings including both elastic and inertia couplings between bending and torsion is developed. It is again the first time in the literature that an analytical model is introduced for the important topic on composite wing structures modeled by beam theory. Free vibration of a cracked composite wing is analyzed with the model.
- Aeroelastic characteristics of an unswept composite wing with an edge crack are investigated. Changes in flutter and divergence speeds due to the presence of the crack and under the condition of varying stiffness orientation are studied. The primary study of the crack induced changes in aeroelastic stabilities may also be used to develop a damage prognosis tool for future composite wing structures.
- It is demonstrated that the model-based approach by using the Cawley-Adams criterion can be used to detect both the size and location of the crack on a composite beam. A new strategy is proposed in selecting natural frequencies for crack detection, which is much less sensitive to measurement errors than the conventional idea that frequencies are selected consecutively from the lowest order to the highest. Results from numerical testing indicate that the measurement error threshold is affected not only by the crack size and location, but also by how strong the bending-torsion coupling is due to the fiber orientation.
- Info-gap decision theory is implemented to investigate parameter uncertainties of the cracked composite beam model. Model performance in terms of natural frequency sensitivities is evaluated as well as compared for several uncertain

parameters, considering the situation that the bending-torsion coupling is strong or weak. The analysis provides guidance to crack detection by changes in natural frequencies.

7.2 Publication Resulting from the Dissertation

The following manuscripts are resulted from the research presented in this dissertation:

- Wang, K., Inman, D. J. and Farrar, C. R., "Crack induced changes in divergence and flutter of cantilevered composite panels," accepted to *Structural Health Monitoring: An International Journal*.

- Wang, K., Inman, D. J. and Farrar, C. R., "Modeling and analysis of a cracked composite cantilever beam vibrating in coupled bending and torsion," *Journal of Sound and Vibration*, in press.

- Wang, K. and Inman, D. J., "Modal models of cracked composite beams," *Proceedings of the 2004 International Conference on Noise and Vibration Engineering* (*ISMA 2004*), Leuven, Belgium, September 20-22, 2004, 1171-1183.

- Wang, K. and Inman, D. J., "Crack induced changes in flutter speed as a damage prognosis tool," *Proceedings of the second European Workshop on Structural Health Monitoring, Munich, Germany*, July 7-9, 2004, 1027-1034.

- Wang, K. and Inman, D. J., "Coupling of bending and torsion of a cracked composite beam," *Proceedings of the 22nd SEM International Modal Analysis Conference*, Dearborn, Michigan, January 26-29, 2004, #283

7.3 Proposed Future Work

The following lists some topics for further research:

- Conduct an experiment to validate as well as calibrate the cracked composite beam model developed in this research.
- Develop a finite element or spectrum element of the cracked composite beam vibrating in coupled bending-torsion in an effort to add a new element to the element library, based on the analytical model presented here.
- Conduct an experiment to validate the aeroelastic characteristics of a cracked composite wing predicted by the analytical model developed in Chapter 4.
- Compare other model-based approaches for crack detection with the one by sensitivity of natural frequencies, such as wave propagation.
- Investigate a damaged composite beam with delamination, closing cracks, or a mixture of matrix and fiber cracking.
- Extend the current cracked composite beam model for a cracked composite beam with asymmetric layouts of plies.

Appendix A

Material Properties of a Single Ply

The complex constants μ_1, μ_2 in equation (3.4) are roots of the characteristic equation (Sih and Chen, 1981):

$$\overline{A}_{11}\mu^4 - 2\overline{A}_{16}\mu^3 + (2\overline{A}_{12} + \overline{A}_{66})\mu^2 - 2\overline{A}_{26}\mu + \overline{A}_{22} = 0 \qquad \text{(A.1)}$$

where the compliances $\overline{A}_{11}$, $\overline{A}_{22}$, $\overline{A}_{12}$, $\overline{A}_{16}$, $\overline{A}_{26}$, $\overline{A}_{66}$ are defined by

$$\overline{A}_{11} = A_{11}m^4 + (2A_{12} + A_{66})m^2n^2 + A_{22}n^4$$

$$\overline{A}_{22} = A_{11}n^4 + (2A_{12} + A_{66})m^2n^2 + A_{22}m^4$$

$$\overline{A}_{12} = (A_{11} + A_{22} - A_{66})m^2n^2 + A_{12}(m^4 + n^4)$$

$$\overline{A}_{16} = (2A_{11} - 2A_{12} - A_{66})m^3n - (2A_{22} - 2A_{12} - A_{66})mn^3$$

$$\overline{A}_{26} = (2A_{11} - 2A_{12} - A_{66})mn^3 - (2A_{22} - 2A_{12} - A_{66})m^3n$$

$$\overline{A}_{66} = 2(2A_{11} + 2A_{22} - 4A_{12} - A_{66})m^2n^2 + A_{66}(m^4 + n^4)$$

with $m = \cos\theta$, $n = \sin\theta$, and θ being the angle between the geometric axes of the beam (*x*-*y*) and the material principle axes (*1*-*2*) as shown in Figure 3.2. The roots are either complex or purely imaginary, and can not be real. The constants μ_1 and μ_2 correspond to those with positive imaginary parts.

Constants $A_{11}, A_{22}, A_{12}, A_{66}$ are compliance elements of the composite along the principle axes and directly relate to the mechanical constants of the material (Vinson and Sierakowski, 1991). Under the plane strain condition,

$$A_{11} = \frac{1}{E_{11}}\left(1 - \frac{E_{22}}{E_{11}}\nu_{12}^2\right)$$

$$A_{22} = \frac{1}{E_{22}}(1 - \nu_{23}^2) \tag{A.2}$$

$$A_{12} = -\frac{\nu_{12}}{E_{11}}(1 + \nu_{23})$$

Under the plane stress condition,

$$A_{11} = \frac{1}{E_{11}},\ A_{22} = \frac{1}{E_{22}},\ A_{12} = -\frac{\nu_{12}}{E_{11}} = -\frac{\nu_{21}}{E_{22}} \tag{A.3}$$

To study the third crack mode, other compliances for both the plane strain and plane stress can be found to be

$$A_{44} = \frac{1}{G_{23}},\ A_{55} = A_{66} = \frac{1}{G_{12}} \tag{A.4}$$

The mechanical properties of the composite, $E_{11}, E_{22}, \nu_{12}, \nu_{23}, G_{12}, G_{23}, \rho$, can be found (Vinson and Sierakowski, 1991) to be

$$E_{11} = E_f V + E_m(1 - V)$$

$$E_{22} = E_{33} = E_m \frac{E_f + E_m + (E_f - E_m)V}{E_f + E_m - (E_f - E_m)V}$$

$$\nu_{12} = \nu_{13} = \nu_f V + \nu_m(1 - V)$$

$$\nu_{23} = \nu_{32} = \nu_f V + \nu_m(1 - V)\frac{1 + \nu_m - \nu_{12}E_m / E_{11}}{1 - \nu_m^2 + \nu_m \nu_{12} E_m / E_{11}} \tag{A.5}$$

$$G_{12} = G_{13} = G_m \frac{G_f + G_m + (G_f - G_m)V}{G_f + G_m - (G_f - G_m)V}$$

$$G_{23} = \frac{E_{22}}{2(1 + \nu_{23})}$$

$$\rho = \rho_f V + \rho_m(1 - V)$$

where subscript *m* stands for matrix and *f* for fiber; *V* is the fiber volume fraction.

Also based on the mechanical properties determined above as well as the ply orientation, the transformed reduced stiffnesses $\bar{Q}_{ij}$ relate to the reduced stiffnesses Q_{ij} by

$$\begin{aligned}
\bar{Q}_{11} &= Q_{11}m^4 + Q_{22}n^4 + 2(Q_{12} + 2Q_{66})m^2n^2 \\
\bar{Q}_{22} &= Q_{11}n^4 + Q_{22}m^4 + 2(Q_{12} + 2Q_{66})m^2n^2 \\
\bar{Q}_{12} &= (Q_{11} + Q_{22} - 4Q_{66})m^2n^2 + Q_{12}(m^4 + n^4) \\
\bar{Q}_{16} &= mn[Q_{11}m^2 - Q_{22}n^2 - (Q_{12} + 2Q_{66})(m^2 - n^2)] \\
\bar{Q}_{26} &= mn[Q_{11}n^2 - Q_{22}m^2 + (Q_{12} + 2Q_{66})(m^2 - n^2)] \\
\bar{Q}_{66} &= (Q_{11} + Q_{22} - 2Q_{12})m^2n^2 + Q_{66}(m^2 - n^2)^2
\end{aligned} \tag{A.6}$$

where

$$Q_{11} = \frac{E_{11}}{1 - \nu_{12}\nu_{21}},\ Q_{22} = \frac{E_{22}}{1 - \nu_{12}\nu_{21}},\ Q_{12} = Q_{11}\nu_{21} = Q_{22}\nu_{12},\ Q_{66} = G_{12}\ .$$

The bending stiffnesses D_{ij} of the beam laminated with *N* plies can then be determined by

$$D_{ij} = \frac{1}{3}\sum_{k=1}^{N}(\bar{Q}_{ij})_k(z_k^3 - z_{k-1}^3) \tag{A.7}$$

where (z_k, z_{k-1}) defines the thickness of the k^{th} ply in the *z*-direction.

Appendix B

Closed Form Solution of the Auxiliary Equation

The governing equation of motion of the composite beam, equation (3.20) or (4.2), can be written in the non-dimensional form:

$$(D^6 + aD^4 - bD^2 - abc)W = 0 \tag{B.1}$$

where $D = d(\cdot)/d\xi$, and a, b, c are positive constants. Substituting the trial solution $W = e^{p\xi}$ to equation (B.1) yields

$$p^6 + ap^4 - bp^2 - abc = 0 \tag{B.2}$$

Let $\lambda = p^2$. Equation (B.2) can be rewritten in the form

$$x^3 - qx - r = 0 \tag{B.3}$$

where

$$x = \lambda + a/3$$

$$q = b + a^2/3$$

$$r = a(bc - b/3 - 2a^2/27)$$

Let $\delta = 27r^2 - 4q^3$. If $\delta < 0$, all three roots of equation (B.3) are real, with one root positive and the other two negative, as given by Pipes and Harvill (1971):

$$x_1 = 2\sqrt{q/3}\cos(\phi/3)$$

$$x_2 = -2\sqrt{q/3}\cos[(\pi - \phi)/3] \tag{B.4}$$

$$x_3 = -2\sqrt{q/3}\cos[(\pi+\phi)/3]$$

with $$\cos\phi = 3r\sqrt{3/q}/(2q).$$

Substitution of r and q in equation (B.3) for δ yields the following expression (Banerjee, 2001):

$$\delta = 27r^2 - 4q^3 = -4b(a^2c^2 - b)^2 - 4a^4bc(1-c^3) - a^2b^2(1-c^2) - 18a^2b^2c(1-c) \quad \text{(B.5)}$$

Since c is always less than 1, it is obvious that $\delta < 0$ and the solution given by (B.4) is justified. Then six roots in equation (B.2), corresponding to three roots given by (B.4), consist of one pair of real roots (α, -α) and two pair of pure imaginary roots ($i\beta$, - $i\beta$; $i\gamma$, - $i\gamma$):

$$\begin{aligned} \alpha^2 &= 2\sqrt{q/3}\cos(\phi/3) - a/3 \\ \beta^2 &= 2\sqrt{q/3}\cos[(\pi-\phi)/3] + a/3 \\ \gamma^2 &= 2\sqrt{q/3}\cos[(\pi+\phi)/3] + a/3 \end{aligned} \quad \text{(B.6)}$$

where α, β and γ are all real and positive, and q and ϕ are given in equations (B.3) and (B.4).

Finally, the solution of the differential equation can be written as

$$W(\xi) = C_1\cosh\alpha\xi + C_2\sinh\alpha\xi + C_3\cos\beta\xi + C_4\sin\beta\xi + C_5\cos\gamma\xi + C_6\sin\gamma\xi \quad \text{(B.7)}$$

where C_1 to C_6 are constants to be determined by boundary conditions.

Bibliography

[1] Abdel Wahab, M. M., Mottershead, J. E., 2001, "Beat-frequencies for damage detection," *Mechanical and Corrosion Properties*, A – Key Engineering Materials, **204**/**205**, 211-220.

[2] Abdo, M. A.-B., Hori, M., 2002, "A numerical study of structural damage detection using changes in the rotation of mode shapes," *Journal of Sound and Vibration*, **251**(2), 227-239.

[3] Adams, R. D., Cawley, P., Pye, C. J. and Stone, B. J., 1978, "A vibration technique for non-destructively assessing the integrity of structures," *Journal of Mechanical Engineering Science*, **20**(2), 93-100.

[4] Agbabian, M. S., Masri, S. F., Miller, R. K. and Caughey, T. K, 1991, "System identification approach to detection of structure changes," *Journal of Engineering Mechanics – ASCE*, **117**(2), 370-390.

[5] Allemang, R. J., 2002, "The modal assurance criterion (MAC): twenty years of use and abuse," *Proceedings of SPIE*, v. 4753, pp. 397-405.

[6] Amaravadi, V., Rao, V., Koval, L. R. and Derriso, M. M., 2001, "Structural health monitoring using wavelet transforms," *Proceeding of SPIE*, v. 4327, pp. 258-269.

[7] Anifantis, N. and Dimarogonas, A., 1983, "Stability of columns with a single crack subjected to follower and vertical loads," *International Journal of Solids and Structures*. **19**(4), 281-291.

[8] Armon, D., Ben-Haim, Y., and Braun, S., 1994, "Crack detection in beams by ranki-ordering of eigenfrequency shifts," *Mechanical Systems and Signal Processing*, **8**(1), 81-91.

[9] Banerjee, J. R., 2001, "Explicit analytical expressions for frequency equation and mode shapes of composite beam," *International Journal of Solids and Structures*, **38**(14), 2415-2426.

[10] Banks, H. T., Inman, D. J., Leo, D. J. and Wang, Y., 1996, "An experimentally validated damage detection theory in smart structures," *Journal of Sound and Vibration*, **191**(5), 859-880.

[11] Bao, G., Ho, S., Sou, Z. and Fan, B., 1992, "The role of material orthotropy in fracture specimens for composites," *International Journal of Solids and Structures*, **29**(9), 1105-1116.

[12] Barbero, E. J. and Reddy, J. N., 1991, "Modeling of delamination in composite laminates using a layer-wise plate theory," *International Journal of Solids and Structures*, **28**(3), 373-388.

[13] Barr, A. D. S., 1966, "An extension of the Hu-Washzu variational principle in linear elasticity for dynamic problems," *Journal of Applied Mechanics*, Transactions of ASME, **33**(2), 465.

[14] Baruch, M and Bar Itzhack, I. Y., 1978, "Optimum weighted orthogonalization of measured modes," *AIAA Journal*, **16**(4), 346-351.

[15] Bauchau, O. A., Zhang, H. C., Loewy, R. G. and Atluri, S. N., 1997, "Nonlinear aeroelastic effects in damaged composite aerospace structures," AIAA-97-0577, January 1997.

[16] Ben-Haim, Y. and Hemez, F. M., 2004, "Robustness-to-uncertainty, fidelity-to-data, and prediction-looseness of models," *Proceedings of the 22nd IMAC*, Dearborn, MI.

[17] Ben-Haim, Y., 2001, "Info-gap value of information in model updating," *Mechanical Systems and Signal Processing*, **15**(3), 457-474.

[18] Ben-Haim, Y., 2001, Information-gap decision theory: decisions under sever uncertainty, Academic Press.

[19] Betz, D. C., Thursby, G., Culshaw, B. and Staszewski, W. J., 2004, "Damage identification using Lamb waves and fibre Bragg grating sensors," *Proceedings of the 2nd European Workshop on Structural Health Monitoring*, Munich, Germany, July 7-9, pp. 1151-1158.

[20] Bisplinghoff, R. L., Ashley, H. and Halfman, R. L., 1996, Aeroelasticity, Dover Publications, Inc., New York.

[21] Brandinelli, L. and Massabo, R., 2003, "Free vibrations of delaminated beam-type structures with crack bridging," *Composite Structures*, **61**(1), 129-142.

[22] Cacciola, P., Impollonia, N. and Muscolino, G., 2003, "Crack detection and location in a damaged beam vibrating under while noise," *Computers and Structures*, **81**(18-19), 1773-1782.

[23] Calabro, A. M., Cusano, A., Giordano, M. and Persiano, G. V., 2002, "Fast and compact-size reader for optical fibres Bragg grating based sensor systems," *Proceedings of the 1st European Workshop on Structural Health Monitoring*, Cachan, France, July 10-12, pp. 524-529.

[24] Carneiro, S. H. S. and Inman, D. J., 2000, "Continuous mathematical model of cracked Timoshenko beams for damage detection," *Proceeding of the 18th International Modal Analysis Conference*, San Antonio, TX, pp. 194-200.

[25] Carneiro, S. H. S., 2000, "Model-based vibration diagnostic of cracked beams in the time domain," Ph.D. dissertation, Virginia Polytechnic Institute and State University, Blacksburg, VA.

[26] Carrasco, C., Osegueda, R., Ferregut, C. and Grygier, M., 1997, "Localization and quantification of damage in a space truss model using modal strain energy," *Proceeding of SPIE*, v. 3043, pp. 181-192.

[27] Cattarius, J. and Inman, D. J., 1997, "Time domain analysis for damage detection in smart structures," *Mechanical Systems and Signal Processing*, **11**(3), 409-423.

[28] Cawley, P. and Adams, R. D., 1979, "The location of defects in structures from measurements of natural frequencies," *Journal of Strain Analysis*, **14**(2), 49-57.

[29] Cesnik, C. E. S., Hodges, D. H. and Patil, M. J., 1996, "Aeroelastic analysis of composite wings," *Proceedings of the AIAA/ASME/ASCE/AHS/ASC Structures, Structural Dynamics, and Materials Conference*, pp. 1113-1123.

[30] Chandra, R., Stemple, A. D. and Chopra, I., 1990, "Thin-walled composite beams under bending, torsional, and extensional loads," *Journal of Aircraft*, **27**(7), 619-626.

[31] Chang, S.-P., Lee, J. and Kim, S., 2002, "Damage detection in a steel bridge using artificial neural network and signal anomaly index," *Proceedings of the 1st European Workshop on Structural Health Monitoring*, Cachan, France, July 10-12, pp. 718-725.

[32] Chang, T. P. and Liang, J. Y., 1998, "Vibration of postbuckled delaminated beam-plates," *International Journal of Solids and Structures*, **35**(12), 1199-1217.

[33] Chaudhari, T. D. and Maiti, S. K., 2000, "A study of vibration of geometrically segmented beams with and without crack," *International Journal of Solids and Structures*, **37**(5), 761-779.

[34] Chaudhry, Z. and Ganino, A. J., 1994, "Damage detection using neural networks: an intial experimental study on debonded beams," *Journal of Intelligent Materials and Structures*, **5**(4), 585-589.

[35] Chaudhry, Z., Lalande, F., Ganino, F., Rogers, C. A. and Chung, J., 1995, "Monitoring the integrity of composite patch structural repair via piezoelectric actuator/sensor," *Proceedings of AIAA/ASME/ASCE/AHS/ASC 36th Structures,*

Structural Dynamics, and Materials Conference, Adaptive Structures Forum, pp. 2243-2248.

[36] Chen, H.-P., 1994, "Free vibration of prebuckled and postbuckled plate with delamination," *Composite Science and Technology*, **51**, 451-462.

[37] Chen, S. Y., Ju, M. S. and Tsuei, Y. G., 1996, "Estimation of mass, stiffness and damping matrices from frequency response functions," *Journal of vibration and Acoustics*, Transactions of the ASME, **118**, 78-82.

[38] Chen, W.-H. and Lin, H.-C., 1985, "Flutter analysis of thin cracked panels using the finite element method," *AIAA Journal*, **23**(5), 795-801.

[39] Cheng, L. K., Groote Schaarserg, J. J. M. and Oostdijk, B. W., 2002, "Multi-channel FBG sensor system for static and dynamic measurement up to 10kHz," *Proceedings of the 1st European Workshop on Structural Health Monitoring*, Cachan, France, July 10-12, pp. 560-567.

[40] Chimenti, D. E. and Martin, R. W., 1991, "Nondestructive evaluation of composite laminates by leaky Lamb waves," *Ultrasonics*, **29**(1), 13-21.

[41] Chinchalkar, S., 2001, "Determination of crack location in beams using natural frequencies," *Journal of Sound and vibration*, **247**(3), 417-429.

[42] Cho, H-N., Choi, Y-M., Lee, S-C. and Hur, C-K, 2004, "Damage assessment of cable stayed bridge using probabilistic neural network," *Structural Engineering and Mechanics*, **17**(3-4), 483-492.

[43] Christides, S. and Barr, A. D. S., 1986, "Torsional vibration of cracked beams of non-circular cross-section," *International Journal of Mechanical Science*, **28**(7), 473-490.

[44] Crane, R. M. and Gagorik, J., 1984, "Fiber optics for a damage assessment system for fiber reinforced plastic composite structures," *Quantitative NDE*, **28**, 1419-1430.

[45] Cusano, A., Capoluongo, P., campopiano, S., Cutolo, A., Giordano, M., Felli, F., Paolozzi, A. and Caponero, M., 2004, "Measuring modal parameter variations on composite structures by fiber Bragg grating sensors," *Proceedings of the 2nd European Workshop on Structural Health Monitoring*, Munich, Germany, July 7-9, pp. 855-861.

[46] Dancila, D. S. and Armanios, E. A., 1998, "The influence of coupling on the free vibration of anisotropic thin-walled closed-section beams," *International Journal of Solids and Structures*, **35**(23), 3108-3119.

[47] Derriso, M. M., Pratt, D. M., Homan, D. B., Schroeder, J. B. and Bortner, R. A., 2003, "Integrated vehicle health management: the key to future aerospace systems," *Proceedings of the 4th International Workshop on Structural Health Monitoring*, Stanford, CA, September 15-17, pp. 3-11.

[48] Diamanti, K., Hodgkinson, J. M. and Soutis, C., 2002, "Damage detection of composite laminates using PZT generated Lamb waves," *Proceedings of the 1st European Workshop on Structural Health Monitoring*, Cachan, France, July 10-12, pp. 398-405.

[49] Dimarogonas, A. and Massouros, G., 1981, "Torsional vibration of a shaft with a circumferential crack," *Engineering Fracture Mechanics*, **15**(3-4), 439-444.

[50] Doebling, S. W., Farrar, C. R. and Prime, M. B., 1998, "A summary review of vibration-based damage identification methods," *The Shock and Vibration Digest*, **30**(2), 91-105.

[51] Doebling, S. W., Peterson, L. D. and Alvin, K. F., 1996, "Estimation of reciprocal residual flexibility from experimental modal data," *AIAA Journal*, **34**(8), 1678-1685.

[52] Dow, M. B. and Dexter, H. B., 1997, "Development of stitched, braided and woven composite structures in the ACT program and at Langley Research Center (1985 to 1997) – summary and bibliography," NASA/TP-97-206234.

[53] Dowell, E. H., Curtiss, H. C., Scanlan, R. H. and Sisto, F., 1978, A modern course in aeroelasticity, Sijthoff & Noordhoff International Publishers B. V., The Netherlands.

[54] Elvin, N., Leung, C. K. Y., Sudarshanam, V. S. and Ezekiel, S., 1999, "A novel fiber optic delamination detectionscheme: theoretical and experimental feasibility studies," *Journal of Intelligent Material Systems and Structures*, **10**(4), 314-321.

[55] Farrar *et al*., 1994, "Dynamic characterization and damage detection in the I-40 bridge over the Rio Grande," *Los Alamos National Laboratory Report*, LA-12767-MS.

[56] Farrar, C. R., Doebling, S. W., James, G. H. and Simmermacher, T., 1997, "Structural health monitoring activities at national laboratories," *Proceedings of the 1st International Workshop on Structural Health Monitoring*, Stanford, CA, September 18-20, pp. 385-395.

[57] Friswell, M. I. and Penny, J. E. T., 2002, "Crack modeling for structural health monitoring," *Structural Health Monitoring: An International Journal*, **1**(2), 139-148.

[58] Friswell, M. I. and Penny, J. E., 1997, "The practical limits of damage detection and location using vibration data," *Proceedings of the 11th VPI & SU Symposium on Structural Dynamics and Control*, Blacksburg, VA, pp. 1-10.

[59] Friswell, M. I., Penny, J. E. T. and Garvey, S. D. A., 1998, "A combined genetic and eigensensitivity algorithms for the location of damage in structures," *Computers and Structures*, **69**, 547-556.

[60] Friswell, M. I., Penny, J. E. T., and Wilson, D. A. L., 1994, "Using Vibration data and statistical measures to locate damage in structures," *Modal Analysis: the International Journal of Analytical and Experimental Modal Analysis*, **9**(4), 239-254.

[61] Fritzen, C-P., 1986, "Identification of mass, damping, and stiffness matrices of mechanical systems," *Journal of Vibration, Acoustics, Stress, and Reliability in Design*, Transactions of the ASME, **108**, 9-16.

[62] Fung, Y. C., 1969, An introduction to the theory of aeroelasticity, Dover Publications, Inc., New York.

[63] Garcia, G. V. and Osegueda, R., "Damage detection using ARMA model coefficients," *Proceedings of SPIE*, v. 3671, pp. 289-296.

[64] Ghoneam, S. M., 1995, "Dynamic analysis of open cracked laminated composite beams," *Composite Structures*, **32**(1-4), 3-11.

[65] Glossop, N. D. W., Dubois, S., Tsaw, W., Leblanc, M., Lymer, J., Measures, R. M. and Tennyson, R. C., 1990, "Optical fibre damage detection for an aircraft composite leading edge," *Composites*, **21**(1), 71-80.

[66] Gounaris, G. and Dimarogonas, A. D., 1988, "A finite element of a cracked prismatic beam for structural analysis," *Computers and Structures*, **28**(3), 309-313.

[67] Guo, S. J., Bannerjee, J. R. and Cheung, C. W., 2003, "The effect of laminate lay-up on the flutter speed of composite wings," *Proceedings of the Institute of Mechanical Engineers, Part B, Journal of Aerospace Engineering*, **217**(3), 115-122.

[68] Hearn, G. and Testa, R. B., 1991, "Modal analysis for damage deletion in structures," *Journal of Structural Engineering – ASCE*, **117**(10), 3042-3063.

[69] Hemez, F. M. and Ben-Haim, Y., 2004, "Info-gap robustness for the correlation of tests and simulations of a non-linear transient," *Mechanical Systems and Signal Processing*, **18**(6), 1443-1467.

[70] Hofer, B., 1987, "Fiber optic damage detection in composite structures," *Composites*, **18**(4), 309-316.

[71] Huston, D., Fuhr, P., Adam, C., Weedon, W. and Maser, K., 1997, "Bridge deck evaluation with ground penetrating radar," *Proceedings of the 1st International Workshop on Structural Health Monitoring*, Stanford, CA, September 18-20, pp. 91-102.

[72] Hwang, H. Y and Kim, C., 2004, "Damage detection in structures using frequency response measurements," *Journal of Sound and Vibration*, **270**(1-2), 1-14.

[73] James, S. W., Tatam, R. P., Twin, A., Morgan, M. and Noonan, P., 2002, "Strain response of fibre Bragg grating sensors at cryogenic temperature," *Proceedings of the 1st European Workshop on Structural Health Monitoring*, Cachan, France, July 10-12, pp. 545-551.

[74] Johnson, G. A., Pran, K., Wang, G., Harsgard, G. B. and Vohra, S. T., 1999, "Structural monitoring of a composite hull air cushion catamaran with a multi-channel fiber Bragg grating sensor system," *Proceedings of the 2nd International Workshop on Structural Health Monitoring*, Stanford, CA, September 8-10, 1999, pp. 190-198.

[75] Jones, K. W. and Turcotte, J. S., 2001, "Finite element model updating using antiresonant frequencies," *Proceeding of the 19th International Modal Analysis Conference*, Kissimmee, FL, pp. 341-347.

[76] Ju, F., Lee, H. P. and Lee, K. H., 1995, "Finite element analysis of free vibration of delaminated composite plates," *Composites Engineering*, **5**(2), 195-209.

[77] Kammer, D. C., 1988, "Optimal approximation for residual stiffness in linear system identification," *AIAA Journal*, **26**(4), 104-112.

[78] Kang, H.-K., Kang, D.-H., Park, J.-S., Hong, C.-S. and Kim, C.-G., 2002, "Strain monitoring of filament wound composite tank using fiber Bragg grating sensors," *Proceedings of the 1st European Workshop on Structural Health Monitoring*, Cachan, France, July 10-12, pp. 568-574.

[79] Kaouk, M. and Zimmerman, D. C., 1994, "Structural damage assessment using a generalized minimum rank perturbation theory," *AIAA Journal*, **32**(4), 836-842.

[80] Kaouk, M. and Zimmerman, D. C., 1995, "Reducing the required number of modes for structural damage assessment," *Proceedings of the 36th AIAA/ASME/ASCE/AHS/ASC Structures, Structural Dynamics and Materials Conference*, AIAA-95-1094-CP, pp. 2802-2812.

[81] Kessler, S. S., Spearing, S. M. and Atalla, M. J., 2002, "In-situ damage detection of composites structures using Lamb wave methods," *Proceedings of the 1st European Workshop on Structural Health Monitoring*, Cachan, France, July 10-12, pp. 347-380.

[82] Khan, A. Z., Stanbridge, A. B. and Ewins, D. J., 1999, "Detecting damage in vibrating structures with a scanning LDV," *Optics and Lasers in Engineering*, **32**(6), 583-592.

[83] Kim, B. S. and Kwak, H. K., 2001, "A study of crack detection in plates using strain mode shapes," *Proceeding of the 19th International Modal Analysis Conference*, Kissimmee, FL, pp. 1212-1218.

[84] Kim, S.-S. and Kim, J.-H., 2003, "Rotating composite beam with a breathing crack," *Composite Structures*, **60**(1), 83-90.

[85] Kim, T., Atluri, S. N. and Loewy, R. G., 1998, "Modeling of microcrack damaged composite plates under bimodular flutter oscillations," *AIAA Journal*, **36**(4), 598-606.

[86] Kisa, M., 2004, "Free vibration analysis of a cantilever composite beam with multiple cracks," *Composite Science and Technology*, **64**(9), 1391-1402.

[87] Krawczuk, M. and Ostachowicz, W. M, 1993, "Hexahedral finite element with an open crack," *Finite Elements in Analysis and Design*, **13**(4), 225-235.

[88] Krawczuk, M. and Ostachowicz, W. M, 1995, "Modelling and vibration analysis of a cantilever composite beam with a transverse open crack," *Journal of Sound and Vibration*, **183**(1), 69-89.

[89] Krawczuk, M., 2002, "Application of spectral beam finite element with a crack and iterative search technique for damage detection," *Finite Elements in Analysis and Design*, **38**(6), 537-548.

[90] Krawczuk, M., Ostachowicz, W. and Zak, A., 1997a, "Dynamics of cracked composite material structures," *Computational Mechanics*, **20**, 79-83.

[91] Krawczuk, M., Ostachowicz, W. and Zak, A., 1997b, "Modal analysis of cracked, unidirectional composite beam," *Composites Part B: Engineering*, **28**(5-6), 641-650.

[92] Kyriazoglou, C., Le Page, B. H., and Guild, F. J., 2004, "Vibration damping for crack detection in composite laminates," *Composites Part A: Applied Science and Manufacturing*, **35**, 945-953.

[93] Lamb, H., 1917, "On waves in an elastic plate," *Proceedings of the Royal Society of London Containing Papers of a Mathematical and Physical Character*, **93**(651), 293-312.

[94] Leissa, A. W., McGee, O. G. and Huang, C. S., 1993, "vibrations of circular plates having V-notches or sharp radial cracks," *Journal of Sound and Vibration*, **161**(2), 227-239.

[95] Lew, J.-S., Sathananthan, S. and Gu, Y., 1997, "Comparison of damage detection algorithms using time domain data," *Proceeding of the 15th International Modal Analysis Conference*, Orlando, FL, pp. 645-651.

[96] Li, C.-S., Ko, W.-J., Lin, H.-T. and Shyu, R.-T., 1993, "Vector autoregressive modal analysis with application to ship structures," *Journal of Sound and Vibration*, **167**(1), 1-15.

[97] Liang, C., Sun, F. P. and Rogers, C. A., 1994, "Coupled electromechanical analysis of adaptive material system – determination of actuator power consumption and system energy transfer," *Journal of Intelligent Material Systems and Structures*, **5**, 21-20.

[98] Librescu, L. and Song, O., 1992, "On the static aeroelastic tailoring of composite aircraft swept wings modeled as thin-walled beam structures," *Composites Engineering*, **2**(5-7), 497-512.

[99] Lieven, N. A. J. and Ewins, D. J., 1988, "Spatial correlation of mode shapes, the coordinate modal assurance criterion (COMAC)," *Proceeding of the 6th International Modal Analysis Conference*, Kissimmee, FL, pp. 690-695.

[100] Lim, T. W., 1990, "A submatrix approach to stiffness using modal test data," *AIAA Journal*, **28**(6), 1123-1130.

[101] Lim, T. W., 1995, "Structural damage detection using constrained eigenstructure assignment," *Journal of Guidance, Control, and Dynamics*, **18**(3), 411-418.

[102] Lin, C. S., 1994, "Unity check method for structural damage detection," *Proceedings of the 35th AIAA/ASME/ASCE/AHS/ASC Structures, Structural Dynamics and Materials Conference*, Hilton Head, SC, pp. 347-354.

[103] Lin, C., 1998, "Unity check method of structural damage detection," *Journal of spacecraft and Rocket*, **34**(4), 577-579.

[104] Lin, K-J., Lu P-J. and Tarn, J-Q, 1989, "Flutter analysis of cantilever composite plates in subsonic flow," *AIAA Journal*, **27**(8), 1102-1109.

[105] Lin, K-J., Lu, P-J. and Tarn, J-Q., 1991, "Flutter analysis of anisotropic panels with patched cracks," Journal of Aircraft, 28(12), 899-907.

[106] Liu, N., Zhu, Q. M., Wei, C. Y., Dykes, N. D. and Irving, P. E., 1999, "Impact damage detection in carbon fibre composite using neural networks and acoustic emission," *Proceedings of the 3rd International Conference on Damage Assessment of Structures* (*DAMAS 99*), Dublin, Ireland, June 28-30, pp. 43-54.

[107] Liu, P.-L. and Sun, S.-C., 1997, "The application of artificial neural networks on the health monitoring of bridges," *Proceedings of the 1st International Workshop on Structural Health Monitoring*, Stanford, CA, September 18-20, 1997, pp. 103-110.

[108] Liu, P.-L., 1995, "Identification and damage detection of trusses using modal data," *Journal of Structural Engineering*, **121**(4), 599-608.

[109] Lloyd, G. M. and Wang, M. L., 1999, "Asymptotic bias correction for a probabilistic neural network for structural health monitoring," *Proceedings of the 2nd International Workshop on Structural Health Monitoring*, Stanford, CA, September 8-10, 1999, pp. 713-722.

[110] Lopes, V. Jr., Pereira, J. A. and Inman, D. J., 2000, "Structural FRF acquisition via electric impedance measurement applied to damage location," *Proceedings of SPIE*, v. 4062, pp. 1549-1555.

[111] Lopes, V., Jr., Park, G., Cudney, H. H. and Inman, D. J., 1999, "Smart structures health monitoring using artificial neural network," *Proceedings of the 2nd International Workshop on Structural Health Monitoring*, Stanford, CA, September 8-10, 1999, pp. 976-985.

[112] Lottati, I., 1985, "Flutter and divergence aeroelastic characteristics for composite forward swept cantilevered wing," *Journal of Aircraft*, **22**(11), 1001-1007.

[113] Luo, H. and Hanagud, S., 2000, "Dynamics of delaminated beams," *International Journal of Solids and Structures*, **37**(10), 1501-1519.

[114] Luo, H., and Hanagud, S., 1997, "Dynamic learning rate neural network training and composite structural damage detection," *AIAA Journal*, **35**(9), 1552-1527.

[115] Luo, S.-N, Fu, Y.-M. and Cao, Z.-Y., 2004, "Non-linear vibration of composite beams with an arbitrary delamination," *Journal of Sound and Vibration*, **271**(3-5), 535-545.

[116] Ma, J. and Pines, D. J., 2003, "Damage detection in a building structure model under seismic excitation using dereverberated wave mechanics," *Engineering Structures*, **25**(3), 385-396.

[117] Majumdar, L and Manohar, C. S., 2004, "Nonlinear reduced models for beam damage detection using data on moving oscillator-beam interactions," *Computers and Structures*, **82**(2-3), 301-314.

[118] Markstrom, K., Storakers, B., 1980, "Buckling of cracked members under tension," *International Journal of Solids and Structures*, **16**(3), 217-229.

[119] Marwala, T. and Hunt, H. E. M., 2000, "Is damage identification using vibration data in a population of cylinders feasible?" *Journal of Sound and Vibration*, **237**(4), 727-732.

[120] Melvin et al., 1997, "Integrated vehicle health monitoring (IVHM) of aerospace vehicles," *Proceedings of the 1st International Workshop on Structural Health Monitoring*, Stanford, CA, September 18-20, pp. 705-714.

[121] Messina, A., Contursi, T. and Williams, E. J. and, 1997, "Multiple damage evaluation using natural frequency changes," *Proceeding of the 15th International Modal Analysis Conference*, Orlando, FL, pp. 658-664.

[122] Messina, A., Jones, A. and Williams, E. J., 1996, "Damage detection and localization using natural frequency changes," *Proceeding of the 14th International Modal Analysis Conference*, Orlando, FL, pp. 67-76.

[123] Modena, C., Sonda, D. and Zonta, D., 1999, "Damage localization in reinforced concrete structures by using damping measurements," *Mechanical and Corrosion Properties*, A – Key Engineering Materials, **167**, 132-141.

[124] Moerman, W., Taerwe, L, De Waele, W., Degrieck, J. and Beats, R., 1999, "Remote monitoring of concrete elements by means of Bragg gratings," *Proceedings of the 2nd International Workshop on Structural Health Monitoring*, Stanford, CA, September 8-10, 1999, pp. 369-378.

[125] Morgan, B. J. and Osterle, R. G., 1985, "On-site modal analysis – a new powerful inspection technique," *Proceedings of the 2nd International Bridge Conference*, Pittsburg, PA, pp. 108-114.

[126] Mottershead, J. E. and Friswell, M. I., 1993, "Model updating in structural dynamics: a survey," *Journal of Sound and Vibration*, **162**(2), 347-375.

[127] Mottershead, J. E., Kyprianou, A. and Ouyang, H, 2003, "Estimation of rotational frequency responses," *Mechanical and Corrosion Properties*, A – Key Engineering Materials, **245**/**246**, 157-116.

[128] Mouritz, A. P., Townsend C. and Shah Khan, M. Z., "Non-destructive detection of fatigue damage in thick composites by pulse-echo ultrasonics," *Composite Science and Technology*, **60**(1), 23-32.

[129] Mujumdar, P. M. and Suryanarayan, S., 1988, "Flexural vibrations of beams with delaminations," *Journal of Sound and Vibration*, **125**(3), 441-461.

[130] Napolitano, K. L. and Kosmatka, J. B., 1996, "Damage detection of highly damped structures using direct frequency response measurements and residual force vectors," *Proceedings of SPIE*, v. 2720, pp. 110-121.

[131] Natke, H. G. and Cempel, C., 1997, "Model-aided diagnosis based on symptoms," *Proceeding of DAMAS '97, Structural Damage Assessment Using Advanced Signal Processing Procedures*, University of Sheffield, UK, pp. 363-375.

[132] Nicholson, D. W. and Alnefaie, K. A., 2000, "Modal moment index for damage detection in beam structures," *Acta Mechanica*, **144**(3-4), 155-167.

[133] Nikpour, K. and Dimarogonas, A., 1988, "Local compliance of composite cracked bodies," *Composite Science and Technology*, **32**(3), 209-223.

[134] Nikpour, K., 1990a, "Diagnosis of axisymmetric cracks in orthotropic cylindrical shells by vibration measurement," *Composites Science and Technology*, **39**(1), 45-61.

[135] Nikpour, K., 1990b, "Buckling of cracked composite columns," *International Journal of Solids and Structures*, **26**(12), 1371-1386.

[136] Norris, M. A. and Meirovitch, L., 1989, "On the problem of modeling for parameter identification in distributed structures," *International Journal for Numerical Methods in Engineering*, **28**, 2451-2463.

[137] Okabe, Y., Mizutani, T., Tsuji, R. and Takeda, N., 2002, "Identification of crack locations in composites using fiber Bragg grating sensors," *Proceedings of the 1st European Workshop on Structural Health Monitoring*, Cachan, France, July 10-12, pp. 517-523.

[138] Ostachowicz, W. and Krawczuk, M., 2001, "On modeling of structural stiffness loss due to damage," *Proceedings of the 4th International Conference on Damage Assessment of Structures* (*DAMAS 2001*), Wales, UK, June 25-28, pp. 185-200.

[139] Ostachowicz, W., Krawczuk, M., Cartmell, M. and Gilchrist, M., 2004, "Wave propagation in delaminated beam," *Computers and Structures*, **82**(6), 475-483.

[140] Paget, C. A., Grondel, S., Levin, K. and Delebarre, C., 2002, "Damage detection in composites by a wavelet-coefficient technique," *Proceedings of the 1st European Workshop on Structural Health Monitoring*, Cachan, France, July 10-12, pp. 313-320.

[141] Palacz, M. and Krawczuk, M., 2002, "Analysis of longitudinal wave propagation in a cracked rod by the spectral element method," *Computers and Structures*, **80**(24), 1809-1816.

[142] Palacz, M. and Krawczuk, M., 2002, "Vibration parameters for damage detection in structures," *Journal of Sound and Vibration*, **249**(5), 999-1010.

[143] Pandey, A. K and Biswas, M., 1994, "Damage detection in structures using changes in flexibility," *Journal of Sound and Vibration*, **169**(1), 3-17.

[144] Pandey, A. K., Biswas, M. and Samman, M. M., 1991, "Damage detection from changes in curvature mode shapes," *Journal of Sound and Vibration*, **145**(2), 321-332.

[145] Parhi, P. K., Sinha, P. K. and Bhattacharyya, S. K., 2001, "Dynamic behavior and impact induced first ply failure of multiple delaminated composite shells," *Journal of Reinforced Plastics and composites*, **20**(15), 1276-1300.

[146] Park, G., Cudney, H. H. and Inman, D. J., 2000, "An integrated health monitoring technique using structural inmedance sensors," *Journal of Intelligent Material Systems and Structures*, **11**(6), 448-455.

[147] Park, G., Sohn, H., Farrar, C. R. and Inman, D. J., 2003, "Overview of piezoelectric impedance-based health monitoring and path forward," *The Shock and Vibration Digest*, **35**(6), 451-463.

[148] Pawar, P. M. and Ganguli, R., 2003, "Genetic fuzzy system for damage detection in beams and helicopter rotor blades," *Computer Methods in Applied Mechanics and Engineering*, **192**(16-18), 2031-2057.

[149] Pines, D. J., 1997, "The use of wave propagation models for structural damage identification," *Proceedings of the 1st International Workshop on Structural Health Monitoring*, Stanford, CA, September 18-20, 1997, pp. 665-677.

[150] Pipes, L. A. and Harvill, L. R., 1971, Applied mathematics for engineers and physicists, McGraw-Hill, NY.

[151] Poe, C. C. Jr., Reeder, J. R. and Yuan, F. G., 2001, "Fracture behavior of a stitched warp-knit fabric composite," *NASA technical report*, NASA/TM-2001-210868.

[152] Qian, G.-L., Gu, S.-N. and Jiang, J.-S., 1990, "The dynamic behavior and crack detection of a beam with a crack," *Journal of Sound and Vibration*, **138**(2), 233-243.

[153] Qin, Z., Librescu, L. and Marzocca, P., 2003, "Aeroelasticity of composite aerovehicle wings in supersonic flows," *Journal of Spacecraft and Rockets*, **40**(2), 162-173.

[154] Raju, V., Park, G. and Cudney, H. H., 1998, "Impedance-based health monitoring technique of composite reinforced structure," *Proceedings of the 9th International Conference on Adaptive Structures and Technologies*, pp. 448-457.

[155] Ramkumar, R. L., Kulkarni, S. V. and Pipes, R. B., 1979, "Free vibration frequencies of a delaminated beam," Reinforced Plastics/Composites Institute, 34th Annual Technical Conference, The Society of the Plastics Industry Inc. 22-E, 1-5.

[156] Ratcliffe, C. P., 1997, "Damage detection using a modified Laplacian operator on mode shape data," *Journal of Sound and Vibration*, **204**(3), 505-517.

[157] Rehfield, L. W., Atilgan, A. R. and Hodges, D. H., 1990, "Nonclassical behavior of thin-walled composite beam with closed cross sections," *Journal of the American Helicopter Society*, pp. 42-50.

[158] Rizos, P. F., Aspragathos, N. and Dimarogonas, A. D., 1990, "Identification of crack location and magnitude in a cantilever from the vibration modes," *Journal of Sound and Vibration*, **138**(3), 381-388.

[159] Russell-Floyd, R. and Phillips, M. G., 1988, "A critical assessment of acousto-ultrasonics as a method of nondestructive examination for carbon-fibre-reinforced thermoplastic laminates," *NDT International*, **21**(4), 247-257.

[160] Rytter, A., 1993, "Vibration based inspection of civil engineering structures," Ph.D. dissertation, Aalborg University, Denmark.

[161] Saitoh, M and Takei, B. T., 1996, "Damage estimation and identification of structural faults using modal parameters," *Proceeding of the 14th International Modal Analysis Conference*, Dearborn, MI, pp. 1159-1164.

[162] Salane, H. J. and Baldwin, J. W., 1990, "Identification of modal properties of bridges," *Journal of Structural Engineering – ASCE*, **116**(6), 2008-2021.

[163] Salawu, O. S., 1997, "Detection of structural damage through changes in frequencies: a review," *Engineering Structures*, **19**(9), 718-723.

[164] Sanayei, M. and Onipede, O., 1991, "Damage assessment of structures using static test data," *AIAA Journal*, **29**(7), 1174-1179.

[165] Sankar, B. V., 1991, "A finite element for modeling delaminations in composite beams," *Computers and Structures*, **38**(2), 239-246.

[166] Shen, M. H. H. and Grady, J. E., 1992, "Free vibrations of delaminated beams," *AIAA Journal*, **30**(5), 1361-1370.

[167] Shen, M. H. H. and Pierre, C., 1990, "Natural modes of Bernoulli-Euler beams with symmetric cracks," *Journal of Sound and Vibration*, **138**(1), 115-134.

[168] Shen, M. H. H. and Pierre, C., 1994, "Free vibrations of beams with a single edge crack," *Journal of Sound and Vibration*, **170**(2), 237-258.

[169] Shi, Z. Y., Law, S. S. and Zhang, L. M., 2000, "Damage localization by directly using incomplete mode shapes," *Journal of Engineering Mechanics – ASCE*, **126**(6), 656-660.

[170] Sih, G. C. and Chen, E. P., 1981, Cracks in composite materials, Mechanics of Fracture, vol. 6, Martinus Nijhoff Publishers.

[171] Sirkis, J., Childers, B., Melvin, L., Peng, T., Tang, Y., Moore, J., Enright, E. and Bovier, C., 1999, "Integrated vehicle health management (IVHM) on space vehicles: a space shuttle fight experiment," *Proceedings of the International Conference on Damage Assessment of Structures* (*DAMAS 99*), Dublin, Ireland, June 28-30, pp. 273-280.

[172] Smith, E. C. and Chopra, I., 1991, "Formulation and evaluation of an analytical model for composite box-beam," *Journal of the American Helicopter Society*, pp. 23-35.

[173] Smith, S. W. and Beattie, C. A., 1991, "Model correlation and damage location for large space truss structures: secant method development and evaluation," *NASA Report*, NASA-CR-188102.

[174] Sohn, H. and Farrar, C. R., 2000, "Statistical process control and projection techniques for damage detection," *European COST F3 Conference on System Identification and Structural Health Monitoring*, Madrid, Spain, pp. 105-114.

[175] Sohn, H., Farrar, C. R., Hemez, F. M., Shunk, D. D., Stinemates, D. W., Nadler, B. R. and Czarnecki, J. J., 2004, "A review of structural health monitoring literature: 1996-2001," *Los Alamos National Laboratory Report*, LA-13976-MS.

[176] Sokolnikoff, I. S., 1983, Mathematical theory of elasticity, Robert T. Krieger Publishing Co.

[177] Song, O., Ha, T.-W., Librescu, L., 2003, "Dynamics of anisotropic composite cantilevers weakened by multiple transverse open cracks," *Engineering Fracture Mechanics*, **70**(1), 105-123.

[178] Stein, M and Housner, J. G., 1974, "Flutter analysis of swept-wing subsonic aircraft with parameter studies of composite wings," *NASA TN D-7539*, NASA Technical Report.

[179] Strganac, T. W. and Kim, Y. I., 1996, "Aeroelastic behavior of composite plates subject to damage growth," *Journal of Aircraft*, **33**(1), 68-73.

[180] Stubbs, N. and Osegueda, R., 1990a, "Global non-destructive damage evaluation in solids," *Modal Analysis: the International Journal of Analytical and Experimental Modal Analysis*, **5**(2), 67-79.

[181] Stubbs, N. and Osegueda, R., 1990b, "Global damage detection in solids – experimental verification," *Modal Analysis: the International Journal of Analytical and Experimental Modal Analysis*, **5**(2), 81-97.

[182] Stubbs, N., Kim, J. T. and Farrar, C. R., 1995, "Field verification of a nondestructive damage localization and sensitivity estimator algorithm," *Proceeding of the 13th International Modal Analysis Conference*, Nashville, TN, pp. 210-218.

[183] Sun, F., Roger, C. A. and Liang, C., 1995, "Structural frequency response function acquisition via electric impedance measurement of surface-bonded piezoelectric sensor/actuator," *Proceedings of the AIAA/ASME/ASCE/AHS/ASC Structures, Structural Dynamics, and Materials Conference*, pp. 3450-3461.

[184] Swamidas, A. S. J. and Sheng, S., 1997, "Detection of fatigue crack initiation and crack growth in tubular T-joints using modal analysis," *Proceeding of the 15th International Modal Analysis Conference*, Orlando, FL, pp. 1801-1807.

[185] Tada, H., Paris, P. C. and Irwin, G. R., 2000, The stress analysis of cracks handbook, 3rd edition, ASME Press.

[186] Tan, K. S., Guo, N., Wong, B. S. and Tui, C. G., 1995, "Comparison of Lamb waves and pulse echo in detection of near-surface defects in laminate plates," *NDT & E International*, **28**(4), 215-223.

[187] Thyagarajan, S. K., Schulz, M. J., Pai, P. F., and Chung, J., 1998, "Detecting structural damage using frequency response functions," *Journal of Sound and Vibration*, **210**(1), 162-170.

[188] Trifunac, M. D., Ivanovic, S. S. and Todorovska, M. I., 2003, "Wave propagation in a seven-story reinforced concrete building: III. Damage detection via changes in wavenumbers," *Soil Dynamics and Earthquake Engineering*, **23**(1), 65-75.

[189] Van Den Abeele, K. E-A., Sutin, A. Carmeliet, J. and Johnson, P. A., 2001, "Micro-damage diagnostics using nonlinear elastic wave spectroscopy (NEWS)," *NDT &E International*, **34**(4), 239-248.

[190] Van der Auweraer, H. and Peeters, B., 2003, "International research projects on structural health monitoring: an review," *Structural Health Monitoring: An International Journal*, **2**(4), 341-358.

[191] Vanhoenaker, K., Schoukens, J., Guillaume, P. and Vanlanduit, S., 2004, "The use of multisine excitations to characterize damage in structures," *Mechanical Systems and Signal Processing*, **18**(1), 43-57.

[192] Viktrov, I. A., 1967, Rayleigh and Lamb Waves, Physical Theory and Applications, Plenum Press, New York.

[193] Voyiadjis, G. Z., 1993, Damage in Composite Materials, Elsevier, Amsterdam, NY.

[194] Wang, J. T. S. , Liu, Y. Y. and Gibby, J. A., 1982, "Vibration of split beams," *Journal of Sound and Vibration*, **84**(4), 491-502.

[195] Wang, W.-C. and Hwang, C.-H., 1998, "Experimental analysis of vibration characteristics of an edge-cracked composite plate by ESPI method," *International Journal of Fracture*, **91**(4), 311-321.

[196] Wang, Z., Lin, R. M. and Lim, M. K., 1997, "Structural damage detection using measured FRF data," *Computer Methods in Applied Mechanics and Engineering*, **147**(1-2), 187-197.

[197] Weisshaar, T. A. and Foist, B. L., 1985, "Vibration tailoring of advanced composite lifting surfaces," *Journal of Aircraft*, **22**(2), 141-147.

[198] Weisshaar, T. A., 1978, "Aeroelastic stability and performance characteristics of aircraft with advanced composite sweptforward wing structures," AFFDL-TR-78-116.

[199] Weisshaar, T. A., 1981, "Aeroelastic tailoring of forward swept composite wings," *Journal of Aircraft*, **18**(8), 669-676.

[200] Weisshaar, T. A., 1985, "Vibration tailoring of advanced composite lifting surfaces," *Journal of Aircraft*, **22**(2), 141-147.

[201] West, W. M., 1984, "Illustration of the use of modal assurance criterion to detect structural changes in an orbiter test specimen," *Proceedings of the Air Force Conference on Aircraft Structural Integrity*, pp. 1-6.

[202] Williams, C. and Salawu, O. S., 1997, "Damping as a damage indication parameter," *Proceeding of the 15th International Modal Analysis Conference*, Orlando, FL, pp. 1531-1536.

[203] Xu, Y., Leung, C. K. Y, Yang, Z., Tong, P. and Lee, S. K. L., 2003, "A new fiber optic based method for delamination detection in composites," *Structural Health Monitoring: An International Journal*, **2**(3), 205-224.

[204] Yin, W. L., and Jane, K. C., 1992, "vibration of delaminated beam-plate relative to buckled states," *Journal of Sound and Vibration*, **156**(1), 125-140.

[205] Yuan, F. G., 2001, "Crack turning mechanics of composite wing skin panels," *NASA technical report*.

[206] Yuen, M. M. F., 1985, "A numerical study of the eigenparameters of a damaged cantilever," *Journal of Sound and Vibration*, **103**(3), 301-310.

[207] Yuen, M. M. F., 1985, "A numerical study of the eigenparameters of damaged cantilever beam," *Journal of Sound and Vibration*, **103**(3), 301-310.

[208] Yun, C.-B. and Bahng, E. Y., 2000, "Substructural identification using neural networks," *Computers and Structures*, **77**(1), 41-52.

[209] Zak, A., Kawczuk, M. and Ostachowicz, W., 2001, "Vibration of a laminated composite plate with closing delamination," *Journal of Intelligent Material Systems and Structures*, **12**(8), 545-551.

[210] Zapico, J. L., Gonzalez, M. P. and Worden, K., 2003, "Damage assessment using neural networks," *Mechanical Systems and Signal Processing*, **17**(1), 119-125.

[211] Zhang, C. and Gross, D., 1993, "Wave attenuation and dispersion in randomly cracked solids – I. Slit cracks," *International Journal of Engineering Science*, **31**(6), 841-858.

[212] Zhang, Z. and Atkan, A. E., 1995, "The damage indices for constructed facilities," *Proceeding of the 13th International Modal Analysis Conference*, Nashville, TN, pp. 1520-1529.

[213] Zhao, J., Ivan, J. N., DeWolf, J. T., 1998, "Structural damage detection using artificial neural networks," *Journal of Infrastructure Systems*, **4**(3), 93-101.

[214] Zimmerman, D. C. and Kaouk, M., 1992, "Eigenstructure assignment approach for structural damage detection," *AIAA Journal*, **30**(7), 1848-1855.

[215] Zimmerman, D. C. and Kaouk, M., 1994, "Structural damage detection using minimum rank update theory," *Journal of Vibration and Acoustics*, **116**, 222-230.

[216] Zonta, D., Bursi, O. S. and Pozzi, M., 2004, "Development of an FBG-based dynamic measurement system for real-time monitoring of RC elements," *Proceedings of the 2nd European Workshop on Structural Health Monitoring*, Munich, Germany, July 7-9, pp. 862-869.

[217] Zou, Y., Tong, L and Steven, G. P., 2000, "Vibration-based model-dependent damage (delamination) identification and health monitoring for composite structures – a review," *Journal of Sound and Vibration*, **230**(2), 357-378.

[218] Jones, R. M., 1975, Mechanics of composite materials, Scripta Book Company.

[219] Vinson, J. R. and Sierakowski, R. L., 1991, Behavior of structures of composed of composite materials, Martinus Nijhoff Publishers.

Vita

Kaihong Wang was born in Anhui, China. After receiving a B.E. in Manufacturing in 1990 from Changsha Institute of Technology, Hunan, China, he worked as a mechanical engineer for Capital Steel & Iron, Inc., in Beijing, China for eight years. In 1998, he entered the graduate school at Southern Illinois University at Carbondale, and received a M.S. in Mechanical Engineering in 2000. In August of 2000 he enrolled at Virginia Polytechnic Institute and State University, Blacksburg, Virginia, as a doctoral student under the supervision of Professor Daniel J. Inman at the Center of Intelligent Material Systems and Structures in the Department of Mechanical Engineering.